DISSERTATION

THERMOPLASTIC ELECTRODE SURFACE MODIFICATIONS FOR USE AS LABEL-FREE ELECTROCHEMICAL IMMUNOSENSORS

Submitted by

Brandaise Martinez

Department of Chemistry

In partial fulfillment of the requirements

For the Degree of Doctor of Philosophy

Colorado State University

Fort Collins, Colorado

Spring 2024

Doctoral Committee:

Advisor: Charles S. Henry

Melissa Reynolds
Christopher Snow
Stuart Tobet

ABSTRACT

THERMOPLASTIC ELECTRODE SURFACE MODIFICATIONS FOR USE AS LABEL-FREE ELECTROCHEMICAL IMMUNOSENSORS

Point-of-care (POC) testing has grown in popularity in recent years, though most common lateral flow assay (LFA) techniques lack sensitivity and are not quantitative. Electrochemical sensors are a promising alternative, specifically thermoplastic electrodes (TPEs) due to their electrochemical performance and durability while remaining inexpensive. TPEs have been used for a wide variety of applications, but their use as immunosensors has been limited due to difficulty with antibody immobilization. This work seeks to explore techniques for modifying TPE surfaces for use as label-free immunosensors.

Chapter 2 examines common antibody immobilization techniques applied to TPEs and determines that the standard existing protocols are lacking. Passive adsorption, EDC/NHS coupling, and chitosan films are used to attach antibodies to the surface. It was found that while each are commonly used in immunosensor fabrication, they have drawbacks that make them unsuitable for TPE immunosensors. Passive adsorption results in unstable antibody attachments leading to inconsistent sensing. EDC/NHS crosslinking is prone to side reactions and again led to inconsistencies in detection of the antigen. Chitosan films were perhaps the most promising, but they passivated the electrode to the extent that detecting the antigen was limited.

Chapter 3 moves towards the development and characterization of a new TPE surface modification using aryl diazonium grafting followed by click chemistry to biotinylate electrodes for easy antibody immobilization. A variety of electrochemical techniques and surface characterizations were used to examine the stepwise modification of the TPE surface. It was shown that click chemistry can be successfully used on TPEs to attach various moieties following aryl diazonium grafting. Ethynyl ferrocene was clicked to the surface resulting in a surface coverage (Γ_{Fc}) of $(1.0 \pm 0.2) \times 10^{-10}$ mol·cm^{-2}, which is comparable to literature values for similar approaches on commercial carbon electrodes. Streptavidinated antibody was successfully attached as well with a clear change in electrochemical signal upon binding.

The method is expanded in Chapter 4 with the use of heterogeneous modifications with multiple functions. The monolayer contains surface bound ferrocene to aid in electron transport, long polyethylene glycol (PEG) spacers to block nonspecific adsorption, in addition to the antibody immobilization point. The modified TPEs were used to successfully detect the nucleocapsid protein of inactivated SARS-CoV-2 virus in buffer solution as a proof-of-concept without the need for a label. The LOD was approximately 6 PFU/mL which exceeds many existing POC tests for COVID-19. The work here expands on the potential applications of TPEs with increased performance and durability over other carbon electrode immunosensors. Potential future directions to expand the sensing capabilities include multiplexed sensors, alternative electrode materials, and expanding to non-antibody based systems.

ACKNOWLEDGEMENTS

I am deeply grateful for the invaluable support and guidance that made this work possible. My heartfelt appreciation goes to Dr. Chuck Henry, my advisor, for his unwavering mentorship and patience. Special thanks to Dr. Yann Leroux and Dr. Philippe Hapiot for their valuable insights during our collaboration and my visit to Rennes. I am indebted to my committee, Dr. Melissa Reynolds, Dr. Chris Snow, and Dr. Stu Tobet, for their counsel throughout my time at CSU.

The friendships cultivated within the Henry Group have been instrumental, especially Emie Marin and my emotional support researcher, Dr. Kate McMahon. My cohort, known as the "Analytical Six," played a crucial role during my initial years in the program. Roxanna Martinez and Heidi Kreckel, bingo Mondays were always a highlight of the week.

I would not be this far in my academic career if not for my parents' support and encouragement. Thank you to my sister for always keeping me humble. My cat, Curie; the best office buddy for working from home. And to Justin, thank you for always being there for me, for cooking me dinner, for listening to my "made-up words", for reminding me to take a break now and then, and for believing in me even when I did not. I could not ask for a better partner.

TABLE OF CONTENTS

CHAPTER 1 - Introduction

1.1 Electrochemical Biosensors

Electrochemical biosensors are a class of biosensors where the interaction between the analyte and the biorecognition element results in a measurable electrochemical change at the electrode.[1] Biosensors target a wide range of biologically relevant analytes, from ions and small molecules to bacteria and viruses. A classic example of an electrochemical biosensor is the handheld glucometer, which measures blood glucose levels at the point-of-care (POC) or point-of-need.[2] The global pandemic brought a more conscious push towards expanding POC electrochemical biosensors to detect infectious diseases.[3]

One of the most common approaches is the affinity-based method which exploits the binding between the analyte and a biorecognition element such as an antibody, aptamer, or a variety of other receptors.[4] **Figure 1.1** illustrates the basic components of an affinity-based electrochemical biosensor, specifically an immunosensor. The biorecognition element, or antibody in this case, is immobilized on the electrode and coated with a blocker to prevent nonspecific adsorption of sample matrix components.[5, 6] The binding event between the analyte antigen and the antibody causes a change measurable via voltammetry, potentiometry, electrochemical impedance spectroscopy or other techniques.[7] Considering the wide availability of options for electrochemical biosensor components, researchers must weigh the options to develop sensitive, selective, robust, and cost-effective sensors.

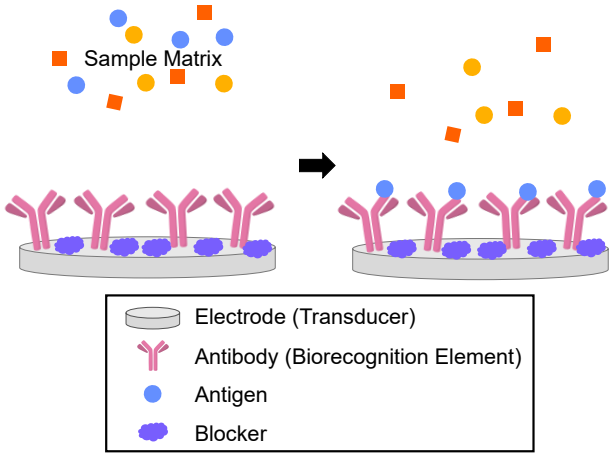

Figure 1.1. Illustration of an affinity based electrochemical biosensor.

Electrochemical immunosensors can be used in labeled or label-free formats. Labeled systems mirror the popular sandwich enzyme-linked immunosorbent assay (ELISA), where a secondary binding event occurs in which an antibody with a tag is bound to the antigen that is caught by the primary antibody.[8] A popular choice of enzymatic tag is horseradish peroxidase (HRP) because it can be used to oxidize a variety of different substrates including 3,3',5,5'-tetramethylbenzidine (TMB) which is turned over into a colored, electrochemically active compound.[9] **Figure 1.2** illustrates the concept of sandwich ELISA using HRP and TMB as the enzyme-substrate pair. The goal of using a label is to provide an indirect measure of the analyte concentration, which often includes increasing the number of detectable molecules to achieve lower limits of detection. For example, in the event of a single antigen binding to an antibody, there is a very small electrochemical change and no colorimetric change. The enzyme-substrate reaction implemented with the HRP-conjugated secondary antibody and addition of TMB can be used to generate thousands of oxidized-TMB molecules to be detected either

electrochemically or colorimetrically. However, label-free electrochemical sensors are desirable because they rely on fewer steps and are more cost-effective.[10]

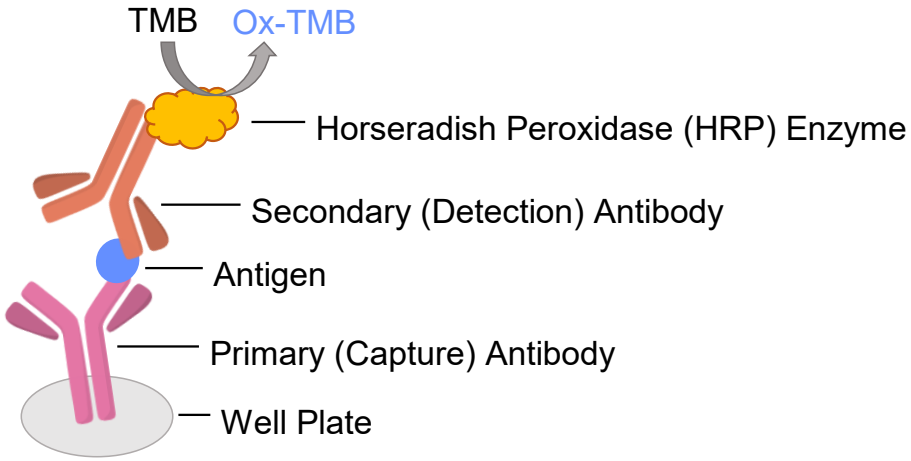

Figure 1.2. Illustration of a sandwich enzyme-linked immunosorbent assay (ELISA) using horseradish peroxidase (HRP) and 3,3',5,5'-tetramethylbenzidine (TMB).

An important choice in electrochemical sensor design is the type of electrode to use as the biosensor transducer. Gold, platinum, and carbon are the most commonly used electrode materials due to their inertness and conductivity.[7, 11] Carbon electrodes are often less expensive than precious metal electrodes, making them an excellent choice. There are many types of carbon electrodes but popular choices for macroelectrodes are commercial glassy carbon (GC) electrodes or screen-printed carbon electrodes (SPCEs).[12] SPCEs (either screen- or stencil-printed) are easily mass produced and are considered inexpensive and disposable electrodes. On the other hand, GC electrodes are often expensive but are reusable with polishing and cleaning steps between uses.

In 2017, Klunder et al. introduced thermoplastic electrodes (TPEs) as a new class of carbon composite electrodes.[13] TPEs take advantage of the low melting points of thermoplastics such as polycaprolactone (PCL) or polystyrene (PS) mixed with graphite powder to result in highly customizable electrodes with electrochemical performance

rivaling commercially available carbon electrodes.[13] The fabrication is briefly illustrated by **Figure 1.3** for TPEs made with PS. First, powdered graphite is added to thermoplastic dissolved in an organic solvent such as dichloromethane. The resulting mixture is then stirred and thoroughly combined on a silicon wafer before allowing the organic solvent to evaporate off. The graphite-thermoplastic material is then formed into an electrode configuration using a hydraulic heat press. The photo in **Figure 1.3** shows a 3-electrode system (working electrode, reference electrode, and counter electrode) cut into a polymethylmethacrylate (PMMA) template. The excess electrode material is sanded away, and connections are added via silver conductive paint. Steps may vary slightly based on the specific types of graphite, thermoplastic, and template used. High performance and customizability combined with the inexpensive materials makes TPEs an excellent choice of carbon electrode over more expensive options (i.e., commercial glassy carbon electrodes) and less durable options (i.e., stencil-printed electrodes).

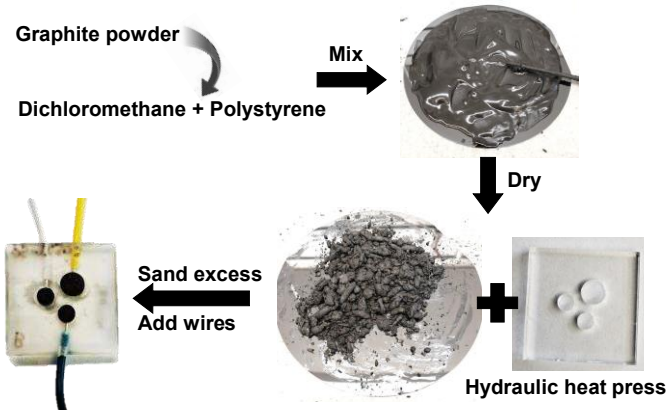

Figure 1.3. Typical thermoplastic electrode fabrication process.

Since their initial development, TPEs have been employed in a wide range of applications.[14-18] Early efforts achieved success in integrating TPEs with microfluidic platforms to detect tryptamine.[17, 19] Recently, TPEs were characterized for their utility for

detecting heavy metals, such as lead, in water.[20] This work thoroughly examined surface chemistry of TPEs based on thermoplastic and graphite type. It was determined that these materials have a significant impact on the performance of the TPE and the function of the TPE could be tuned based on the material used for fabrication. Characterization of a variety of TPE compositions using scanning electrochemical microscopy (SECM) in a variety of redox probes also demonstrated the dependence on graphite or polymer type for performance.[21] For example, it was established in another work that PS TPEs perform best for the simultaneous detection of ascorbic acid, uric acid, and dopamine at bare electrodes.[18] The TPE electrode material can be modified by mixing in other materials, such as enzymes, as demonstrated by Clark et al. with glucose oxidase mixed in to TPE formulations to detect glucose.[14]

Surface modifications, the addition of extra reagents to manipulate the surface chemistry, of TPEs has also been explored previously to expand the potential applications. This approach involved adding an ion-selective membrane for the successful detection of potassium and sodium.[15, 22] TPEs with surface modifications are also good choices for immunosensor applications due to their durability and biocompatibility. Immunosensors are a class of biosensors that rely on the interaction between the analyte (an antigen) and a corresponding antibody to produce a signal.[23] The antigen targeted is often part of a complex sample matrix and the affinity of the antibody is relied upon for sensor selectivity.

One case of TPEs being used as an immunosensor currently exists where TPEs modified with antibodies were able to successfully detect *Escherichia coli* with a limit of detection of 27 CFU/mL in buffer solution.[16] This method relied on first modifying the TPE surfaces with an amine group before antibody immobilization by 1-ethyl-3-(3-

dimethylaminopropyl)-carbodiimide (EDC) and N-hydroxysuccinimide (NHS) crosslinking.[16] The EDC/NHS crosslinking method is commonly used in immunoassays and immunosensors, however, it is prone to side reactions which may limit the number of active antibodies immobilized on the electrode surface.[24] There is more work to be done to develop facile protocols for immunosensor fabrication using TPEs to be applied to a wide range of bacterial and viral targets.

1.2 Diazonium Grafting and Click Chemistry for Electrode Modification

The aforementioned *E. coli* sensor on TPEs used a diazonium produced from 4-nitroaniline with sodium nitrite in p-toluenesulfonic acid followed by electrochemical reduction to yield an amine modified surface.[16] A similar approach was also demonstrated on stencil-printed electrodes to detect C-reactive protein with dynamic range of 0.01 – 10 ng/mL.[25] These approaches are promising however, they have two potential drawbacks. The first is that the diazonium grafting in this manner produces a disordered, multilayered film on the electrode surface due to the highly reactive radical intermediates.[25, 26] The second is that they rely on EDC/NHS as a secondary reaction for the immobilization of antibodies. EDC is readily hydrolyzed in aqueous solution and is prone to side reactions.[24] Thus, the need exists for more easily controlled TPE surface functionalization and subsequent antibody immobilization.

One approach for simple modification of carbon electrodes is via reduction of diazonium salts.[27] **Figure 1.4** shows the general reaction mechanism for diazonium reduction onto carbon electrodes. A reducing potential is applied to the electrode, which initiates the formation of a radical with the loss of the diazonium as N_2 gas. The reaction can be easily controlled to generate patterned surfaces.[28] However, the production of

highly reactive radical intermediates can lead to disorganized multilayers forming. A solution to this was presented by Leroux et al., with the determination that modifications by diazonium electrografting can be limited to monolayers by using a silyl protecting group.[29] Further, binary layers can be produced, and the density of the modification monolayer can be controlled by changing the size of the protecting group.[26, 30]

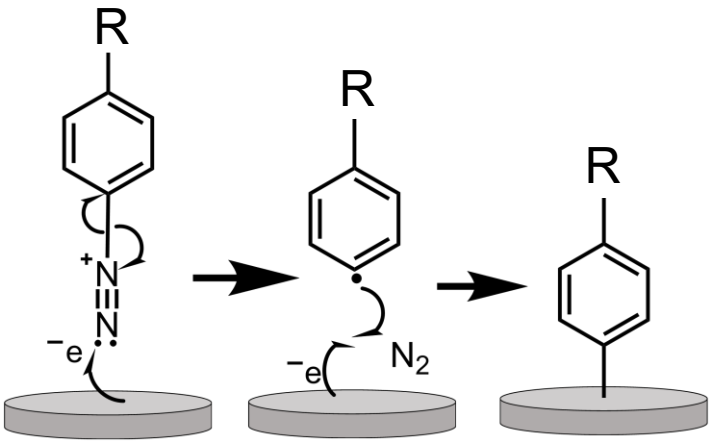

Figure 1.4. General mechanism for aryl diazonium grafting.

Berg et al. first demonstrated the successful diazonium electrografting on TPEs in 2019. Solvent-resistant TPEs were made with cyclic olefin copolymer (COC) as the thermoplastic in a glass template and modified with a variety of para substituted diazonium compounds in acetonitrile.[31] A benefit of aryldiazonium grafting is the variety of substituted compounds available providing many options for functionalization of TPEs. One approach is to functionalize the TPE surface with a terminal alkyne via diazonium grafting, which can then be exploited for subsequent reactions using click chemistry.[29, 31]

Click chemistry, first described in 2001, is a class of convenient and robust reactions in which the two reactants "click" together in facile manner regardless of the rest of the molecular structure.[32, 33] Copper-catalyzed azide-alkyne cycloaddition (CuAAC) is one type of click chemistry where azido- compounds are reacted with terminal

alkynes to form [1,2,3]-triazoles.[34, 35] **Figure 1.5** shows the simplified, generic CuAAC mechanism. The convenient regioselective reaction is successful under mild conditions with such broad applications that the founders were awarded the Nobel Prize in Chemistry 2022.[36] Numerous works have been published utilizing the convenience of click chemistry to develop electrochemical sensors.[37, 38]

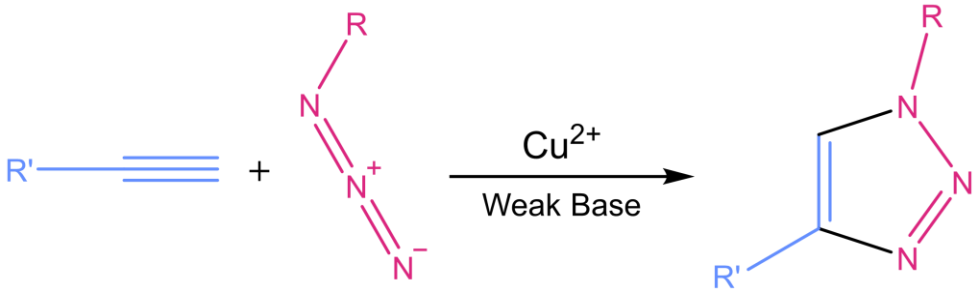

Figure 1.5. Generic copper-catalyzed azide-alkyne cycloaddition (CuAAC) reaction between a terminal alkyne and an azide to form a substituted triazole.

The aryl diazonium grafting on TPEs used subsequent click chemistry to immobilize azidomethylferrocene on the surface with surface concentrations within the same magnitude of the maximum possible ferrocene surface concentration.[12, 31] The 2-step approach of diazonium grafting followed by click chemistry has also been applied to electrochemical biosensors. Of course, the versatility of the method has led to a wide variety of approaches for biorecognition elements. Aptamers,[39] enzymes,[40] and antibodies[41, 42] have each been successfully implemented using CuAAC reactions with alkyne- or azido- decorated carbon electrodes. Sequential reactions with alkyne- and azide-modified DNA probes were used to easily modify gold electrodes that were electrografted with a diazonium salt to develop a multiplexed sensor.[43] One work also examined the use of CuAAC to covalently bind biotin to the surface to take advantage of streptavidin-biotin conjugation more efficiently.[44] This approach allows for even more

choice in biosensor target, because it can be used with any streptavidin or avidin conjugated constituent.

Several works have used diazonium grafting followed by click chemistry to fabricate label-free sensors. Meini et al. modified gold electrodes with terminal alkynes prior to clicking azido-PEG3-biotin and streptavidin to the surface for the label-free detection of biotinylated human serum albumin.[42] The dynamic range of the sensor was determined to be 10 pg/mL to 100 ng/mL using impedimetric detection.[42] Another approach to label-free sensors used aptamers clicked onto gold nanoparticles that were deposited onto SPCEs also achieved pg/mL levels of detection for their target analyte.[43] Hepatitis C electrochemical sensors were also developed using DNA probes clicked onto modified gold electrodes in the nanomolar range.[44] A common theme with these label-free systems is the limited working range, spanning only one or two orders of magnitude. While the very low limits of detection (LODs) are exciting, some analytes require maintaining a wide working range to encompass the variety of patient samples that may be encountered.

1.3 Signal Amplification and Multifunctional Monolayers

Signal amplification techniques are a common approach to not only further reducing the LOD but also increasing the sensitivity and the dynamic range of label-free electrochemical sensors. A key point is introducing components into the system that maintain the ease of the label-free system instead of simply adding a label. For example, the electron transfer of carbon electrodes can be enhanced to increase the measured current. The most common approach is to introduce gold nanoparticles (AuNPs) to the

electrode surface prior to modifications.[45] AuNPs may be susceptible to desorption from the carbon surface, can be expensive, and can complicate the sensor fabrication process depending on the nanoparticle synthesis.

Nanostructuring the carbon electrode surface is a quickly rising alternative to boost electron transfer.[46] TPEs have already seem to reap benefits of their rough and complex surface morphology compared to other carbon electrode types, making them an excellent electrode candidate for label-free sensing.[8, 11] An additional mechanism of improving performance of label-free sensing is through electrocatalysis in which groups bound to the electrode surface then enhance the measured current.[47]

Signal enhancing components can also be introduced to the sensor by designing heterogeneous monolayers on the electrode. Liu and Gooding developed a sensor to characterize protein electrochemistry by interspacing molecular wires between polyethylene glycol (PEG) spacers.[45] The molecular wires enhance electron transfer while the PEG spacers acted as a blocker to prevent nonspecific adsorption.[45] PEG has been shown to be an excellent blocker for immunosensors immunosensor.[46] In another work, sequential reactions were used to coimmobilize enzymes and electrocatalysts, demonstrating successful heterogeneous modifications using click chemistry following diazonium grafting.[47] Thus, integrating varying PEG spacer lengths for click chemistry in sequential reactions or mixed reagents is an attractive approach to yield multifunctional modifications.

1.4 My Contributions

The work presented in this dissertation achieves three main objectives towards the overall goal of developing TPE-based immunosensors. Chapter 2 discusses the first

objective of exploring existing antibody immobilization techniques applied on TPEs. This chapter presents the initial dive into electrochemical immunosensors based on trends in literature and establishes the need for a novel approach to antibody immobilization on TPEs. The data in Chapter 2 was presented, in part, at ACS Fall 2022.[48]

Chapter 3 highlights the second objective which is the development of a standardized protocol for the stable and consistent modification of the TPE surface with antibodies. This is achieved using diazonium chemistry followed by click chemistry. Each step of the protocol was examined by surface characterization techniques (such as X-ray photoelectron spectroscopy and scanning electrochemical microscopy) in addition to traditional electrochemical techniques like cyclic voltammetry and electrochemical impedance spectroscopy. The data in Chapter 3 was recently published in *ACS Applied Materials and Interfaces*.[49]

The third objective is to further investigate the utility of click chemistry to modify TPEs for use as biosensors. In Chapter 4, signal enhancing behavior is implemented into TPEs by mixing PEG lengths and functionalization clicked to the surface. The result is a system where the electrodes are decorated with N_3-PEG3-Fc mixed with N_3-PEG11-biotin or N_3-PEG24-biotin. It was determined that N_3-PEG11-biotin mixed layers are more resistant to nonspecific adsorption, but N_3-PEG24-biotin mixed layers are successfully able to be used for detection of SARS-CoV-2 N protein. Chapter 4 is in progress to be submitted for publication.

Appendix C shares the data collected for a collaborative project with the Tobet Lab. The work, published in *Analytical Chemistry*, explores the use of 1H-NMR to characterize the short-chain fatty acids (SCFAs) produced by the gut microbiome present in mouse gut

tissue explants maintained in microfluidic devices.[50] The goal was to determine the impact of including a physiologically relevant oxygen gradient across the tissue on microbiome metabolism and thus, SCFA production. SCFAs were semi-quantitatively monitored across time points for different oxygen environments showing the prominent impacts of the oxygen gradient on lactate, butyrate, acetate, and propionate production. The ^{1}H-NMR experiments and data analysis were completed during the first two years of my PhD and provided a strong base for my development as a researcher.

Overall, this dissertation seeks to demonstrate the development of a TPE immunosensor platform from fundamental surface chemistry towards immunosensing applications. A proof-of-concept demonstration of detecting SARS-CoV-2 nucleocapsid protein is given with many areas for improvement and expansion of applications. The work here has wide implications with the potential to be applied to a variety of electrode types, biorecognition elements, and analytes.

References

1. Bhalla, N.; Jolly, P.; Formisano, N.; Estrela, P., Introduction to biosensors. *Essays Biochem* **2016,** *60* (1), 1-8.

2. Yoo, E. H.; Lee, S. Y., Glucose biosensors: an overview of use in clinical practice. *Sensors (Basel)* **2010,** *10* (5), 4558-76.

3. Madhurantakam, S.; Muthukumar, S.; Prasad, S., Emerging Electrochemical Biosensing Trends for Rapid Diagnosis of COVID-19 Biomarkers as Point-of-Care Platforms: A Critical Review. *ACS Omega* **2022,** *7* (15), 12467-12473.

4. Campuzano, S.; Pingarrón, J. M., Electrochemical Affinity Biosensors: Pervasive Devices with Exciting Alliances and Horizons Ahead. *ACS Sensors* **2023,** *8* (9), 3276-3293.

5. Contreras-Naranjo, J. E.; Aguilar, O. Suppressing Non-Specific Binding of Proteins onto Electrode Surfaces in the Development of Electrochemical Immunosensors *Biosensors* [Online], 2019.

6. Lichtenberg, J. Y.; Ling, Y.; Kim, S. Non-Specific Adsorption Reduction Methods in Biosensing *Sensors* [Online], 2019.

7. Grieshaber, D.; MacKenzie, R.; Vörös, J.; Reimhult, E., Electrochemical Biosensors - Sensor Principles and Architectures. *Sensors (Basel)* **2008,** *8* (3), 1400-1458.

8. Clark, M. F.; Lister, R. M.; Bar-Joseph, M., ELISA techniques. In *Methods in Enzymology*, Academic Press: 1986; Vol. 118, pp 742-766.

9. Fanjul-Bolado, P.; González-García, M. B.; Costa-García, A., Amperometric detection in TMB/HRP-based assays. *Anal Bioanal Chem* **2005,** *382* (2), 297-302.

10. Samuel, V. R.; Rao, K. J., A review on label free biosensors. *Biosensors and Bioelectronics: X* **2022,** *11*, 100216.

11. Mehrvar, M.; Abdi, M., Recent Developments, Characteristics, and Potential Applications of Electrochemical Biosensors. *Analytical Sciences* **2004,** *20* (8), 1113-1126.

12. McCreery, R. L., Advanced Carbon Electrode Materials for Molecular Electrochemistry. *Chemical Reviews* **2008,** *108* (7), 2646-2687.

13. Klunder, K. J.; Nilsson, Z.; Sambur, J. B.; Henry, C. S., Patternable Solvent-Processed Thermoplastic Graphite Electrodes. *Journal of the American Chemical Society* **2017,** *139* (36), 12623-12631.

14. Clark, K. M.; Henry, C. S., Thermoplastic Electrode (TPE)-based Enzymatic Glucose Sensor Using Polycaprolactone-graphite Composites. *Electroanalysis* **2021,** *n/a* (n/a).

15. Ozer, T.; Henry, C. S., Microfluidic-based ion-selective thermoplastic electrode array for point-of-care detection of potassium and sodium ions. *Microchimica Acta* **2022,** *189* (4), 152.

16. Ozer, T.; McCord, C.; Geiss, B. J.; Dandy, D.; Henry, C. S., Thermoplastic Electrodes for Detection of Escherichia coli. *Journal of The Electrochemical Society* **2021,** *168* (4), 047509.

17. Pradela-Filho, L. A.; Araújo, D. A. G.; Takeuchi, R. M.; Santos, A. L.; Henry, C. S., Thermoplastic electrodes as a new electrochemical platform coupled to microfluidic devices for tryptamine determination. *Analytica Chimica Acta* **2021,** *1147*, 116-123.

18. McCord, C. P.; Summers, B.; Henry, C. S., Simultaneous Analysis of Ascorbic Acid, Uric Acid, and Dopamine at Bare Polystyrene Thermoplastic Electrodes. *ChemElectroChem* **2022,** *9* (11), e202101600.

19. Noviana, E.; Klunder, K. J.; Channon, R. B.; Henry, C. S., Thermoplastic Electrode Arrays in Electrochemical Paper-Based Analytical Devices. *Analytical Chemistry* **2019,** *91* (3), 2431-2438.

20. McMahon, C. J.; Martinez, B.; Henry, C. S., Characterization of Factors Affecting Stripping Voltammetry on Thermoplastic Electrodes. *Journal of The Electrochemical Society* **2023**.

21. Berg, K. E.; Leroux, Y. R.; Hapiot, P.; Henry, C. S., SECM Investigation of Carbon Composite Thermoplastic Electrodes. *Analytical Chemistry* **2021,** *93* (3), 1304-1309.

22. Ozer, T.; Henry, C. S., All-solid-state potassium-selective sensor based on carbon black modified thermoplastic electrode. *Electrochimica Acta* **2022,** *404*, 139762.

23. Mollarasouli, F.; Kurbanoglu, S.; Ozkan, S. A., The Role of Electrochemical Immunosensors in Clinical Analysis. *Biosensors (Basel)* **2019,** *9* (3).

24. Vashist, S. K., Comparison of 1-Ethyl-3-(3-Dimethylaminopropyl) Carbodiimide Based Strategies to Crosslink Antibodies on Amine-Functionalized Platforms for Immunodiagnostic Applications. *Diagnostics (Basel)* **2012,** *2* (3), 23-33.

25. Gillan, L.; Teerinen, T.; Johansson, L.-S.; Smolander, M., Controlled diazonium electrodeposition towards a biosensor for C-reactive protein. *Sensors International* **2021,** *2*, 100060.

26. Leroux, Y. R.; Hapiot, P., Nanostructured Monolayers on Carbon Substrates Prepared by Electrografting of Protected Aryldiazonium Salts. *Chemistry of Materials* **2013,** *25* (3), 489-495.

27. Pinson, J.; Podvorica, F., Attachment of organic layers to conductive or semiconductive surfaces by reduction of diazonium salts. *Chemical Society Reviews* **2005,** *34* (5), 429-439.

28. Flavel, B. S.; Gross, A. J.; Garrett, D. J.; Nock, V.; Downard, A. J., A Simple Approach to Patterned Protein Immobilization on Silicon via Electrografting from Diazonium Salt Solutions. *ACS Applied Materials & Interfaces* **2010,** *2* (4), 1184-1190.

29. Leroux, Y. R.; Fei, H.; Noël, J.-M.; Roux, C.; Hapiot, P., Efficient Covalent Modification of a Carbon Surface: Use of a Silyl Protecting Group To Form an Active Monolayer. *Journal of the American Chemical Society* **2010,** *132* (40), 14039-14041.

30. Leroux, Y. R.; Hui, F.; Noël, J.-M.; Roux, C.; Downard, A. J.; Hapiot, P., Design of Robust Binary Film onto Carbon Surface Using Diazonium Electrochemistry. *Langmuir* **2011,** *27* (17), 11222-11228.

31. Berg, K. E.; Leroux, Y. R.; Hapiot, P.; Henry, C. S., Increasing Applications of Graphite Thermoplastic Electrodes with Aryl Diazonium Grafting. *ChemElectroChem* **2019,** *6* (18), 4811-4816.

32. Kolb, H. C.; Finn, M. G.; Sharpless, K. B., Click Chemistry: Diverse Chemical Function from a Few Good Reactions. *Angewandte Chemie International Edition* **2001,** *40* (11), 2004-2021.

33. Devaraj, N. K.; Finn, M. G., Introduction: Click Chemistry. *Chemical Reviews* **2021,** *121* (12), 6697-6698.

34. Rostovtsev, V. V.; Green, L. G.; Fokin, V. V.; Sharpless, K. B., A Stepwise Huisgen Cycloaddition Process: Copper(I)-Catalyzed Regioselective "Ligation" of Azides and Terminal Alkynes. *Angewandte Chemie International Edition* **2002,** *41* (14), 2596-2599.

35. Tornøe, C. W.; Christensen, C.; Meldal, M., Peptidotriazoles on Solid Phase: [1,2,3]-Triazoles by Regiospecific Copper(I)-Catalyzed 1,3-Dipolar Cycloadditions of Terminal Alkynes to Azides. *The Journal of Organic Chemistry* **2002,** *67* (9), 3057-3064.

36. The Nobel Prize in Chemistry 2022. https://www.nobelprize.org/prizes/chemistry/2022/summary/ (accessed Oct 16).

37. Cernat, A.; Tertiş, M.; Cristea, C.; Săndulescu, R., Applications of Click Chemistry in the Development of Electrochemical Sensors. *International Journal of Electrochemical Science* **2015,** *10* (8), 6324-6337.

38. Yáñez-Sedeño, P.; González-Cortés, A.; Campuzano, S.; Pingarrón, J. M., Copper(I)-Catalyzed Click Chemistry as a Tool for the Functionalization of Nanomaterials and the Preparation of Electrochemical (Bio)Sensors. *Sensors (Basel)* **2019,** *19* (10).

39. Hayat, A.; Sassolas, A.; Marty, J.-L.; Radi, A.-E., Highly sensitive ochratoxin A impedimetric aptasensor based on the immobilization of azido-aptamer onto electrografted binary film via click chemistry. *Talanta* **2013,** *103*, 14-19.

40. Hayat, A.; Sassolas, A.; Rhouati, A.; Marty, J.-L., Immobilization of Enzymes on Ethynyl-Modified Electrodes via Click Chemistry. In *Immobilization of Enzymes and Cells: Third Edition*, Guisan, J. M., Ed. Humana Press: Totowa, NJ, 2013; pp 209-216.

41. Qi, H.; Li, M.; Zhang, R.; Dong, M.; Ling, C., Double electrochemical covalent coupling method based on click chemistry and diazonium chemistry for the fabrication of sensitive amperometric immunosensor. *Analytica Chimica Acta* **2013,** *792*, 28-34.

42. Guerrero, S.; Cadano, D.; Agüí, L.; Barderas, R.; Campuzano, S.; Yáñez-Sedeño, P.; Pingarrón, J. M., Click chemistry-assisted antibodies immobilization for immunosensing of CXCL7 chemokine in serum. *Journal of Electroanalytical Chemistry* **2019,** *837*, 246-253.

43. Levrie, K.; Jans, K.; Vos, R.; Ardakanian, N.; Verellen, N.; Van Hoof, C.; Lagae, L.; Stakenborg, T., Multiplexed site-specific electrode functionalization for multitarget biosensors. *Bioelectrochemistry* **2016,** *112*, 61-66.

44. Evrard, D.; Lambert, F.; Policar, C.; Balland, V.; Limoges, B., Electrochemical Functionalization of Carbon Surfaces by Aromatic Azide or Alkyne Molecules: A Versatile Platform for Click Chemistry. *Chemistry – A European Journal* **2008,** *14* (30), 9286-9291.

45. Liu; Gooding, J. J., An Interface Comprising Molecular Wires and Poly(ethylene glycol) Spacer Units Self-Assembled on Carbon Electrodes for Studies of Protein Electrochemistry. *Langmuir* **2006,** *22* (17), 7421-7430.

46. Kingshott, P.; Thissen, H.; Griesser, H. J., Effects of cloud-point grafting, chain length, and density of PEG layers on competitive adsorption of ocular proteins. *Biomaterials* **2002,** *23* (9), 2043-2056.

47. Zhang, L.; Vilà, N.; Walcarius, A.; Etienne, M., Molecular and Biological Catalysts Coimmobilization on Electrode by Combining Diazonium Electrografting and Sequential Click Chemistry. *ChemElectroChem* **2018,** *5* (16), 2208-2217.

48. McMahon, C.; Martinez, B.; Henry, C. S., Surface modification of thermoplastic electrodes for electrochemical immunosensors. In *American Chemical Society Fall Meeting*, Chicago, Illinois, 2022.

49. Martinez, B.; Leroux, Y. R.; Hapiot, P.; Henry, C. S., Surface Modification of Thermoplastic Electrodes for Biosensing Applications via Copper-Catalyzed Click Chemistry. *ACS Applied Materials & Interfaces* **2023**.

50. Martinez, B.; Schwerdtfeger, L. A.; Richardson, A.; Tobet, S. A.; Henry, C. S., 1H-NMR Profiling of Short-Chain Fatty Acid Content from a Physiologically Accurate Gut-on-a-Chip Device. *Analytical Chemistry* **2022,** *94* (28), 9987-9992.

CHAPTER 2 – Survey of Antibody Immobilization Approaches on Thermoplastic Electrodes

2.1 Overview

The goal of this chapter is to present the preliminary antibody immobilization attempts on thermoplastic electrodes (TPEs) which is motivation for the remainder of the dissertation. The data has not been published and was collected with the collaboration of Cynthia McCord, Kate McMahon, and external collaborators at Oakridge National Laboratory. K. McMahon and I conducted the experiments included here which was presented, in part, as an oral presentation and a poster at ACS Fall 2022.[1] The chapter is not given in chronological order for clarity and some studies may be incomplete due to funding at the time of the work.

Various common antibody immobilization techniques were attempted on TPEs with the goal of developing a label free sensor for a model bacterial target *(Escherichia coli)* including EDC/NHS coupling, passive adsorption, and chitosan films. Difficulties such as side reactions and highly variable TPE surfaces caused each immobilization technique to have limited reproducibility and electrochemical performance. The findings were that TPEs in their basic form can be widely variable and are generally unsuccessful sensors when using common antibody immobilization techniques.

2.2 Introduction

Thermoplastic electrodes (TPEs) have been shown to be highly advantageous for a variety of applications, however, there is yet to have broad implementation of TPEs as immunosensors.[2-5] One limiting factor is the lack of a defined protocol for successfully

immobilizing antibodies to the surface of TPEs. Antibodies are widely used biorecognition elements in electrochemical sensors. The antibody must have the appropriate density while maintaining a good proportion of the active paratopes available for binding antigen epitopes. There are a broad variety of approaches that have been successfully applied to immunoassays, including electrochemical sensors.

One approach is to rely on electrostatic forces and passively adsorb antibodies to the electrode surface (**Figure 2.1A**). Sharafeldin et al. demonstrated that while having somewhat lower antibody coverage compared to other immobilization methods, sensors made with antibodies passively adsorbed had a comparable number of active antibodies per electrode (correctly orientated) compared to other techniques.[6] Passive adsorption is easy to do, however, the attractions between the antibodies and the electrode surface are weak and may cause antibody denaturing.[7-9]

An alternative is to use a covalent crosslinking approach to ensure stability of the antibody attachment to the electrode surface. Commonly used is N-(3-dimethylaminopropyl)-N′-ethylcarbodiimide hydrochloride (EDC) with N-hydroxysulfosuccinimide (NHS) crosslinking (**Figure 2.1B**) which yields a zero-length connection between a carboxylic group and an amine.[10] EDC/NHS crosslinking has been used in a wide variety of electrochemical sensors, including carbon-based electrodes, to immobilize antibodies.[11-14] Cross reactions including hydrolysis in aqueous solutions are a problem also commonly associated with EDC/NHS crosslinking, meaning it may not always be the ideal choice for antibody immobilization.[10]

Another crosslinking method uses chitosan activated with glutaraldehyde (**Figure 2.1C**) to form bonds between the amines of chitosan (and itself) and antibodies via reactions with the carbonyls of glutaraldehyde.[15] Chitosan films have been evaluated as

platforms for antibody immobilization and have been successfully used to immobilize enzymes such as horseradish peroxidase on the surface of a carbon electrode for biosensing applications.[16, 17] One work used chitosan film to immobilize antibodies and found that it aided in stability of the sensor with less than 10% of signal loss after storage for five days.[6] One drawback of chitosan is that it can strongly passivate the electrode, resulting in very low electrochemical performance, as is shown herein.

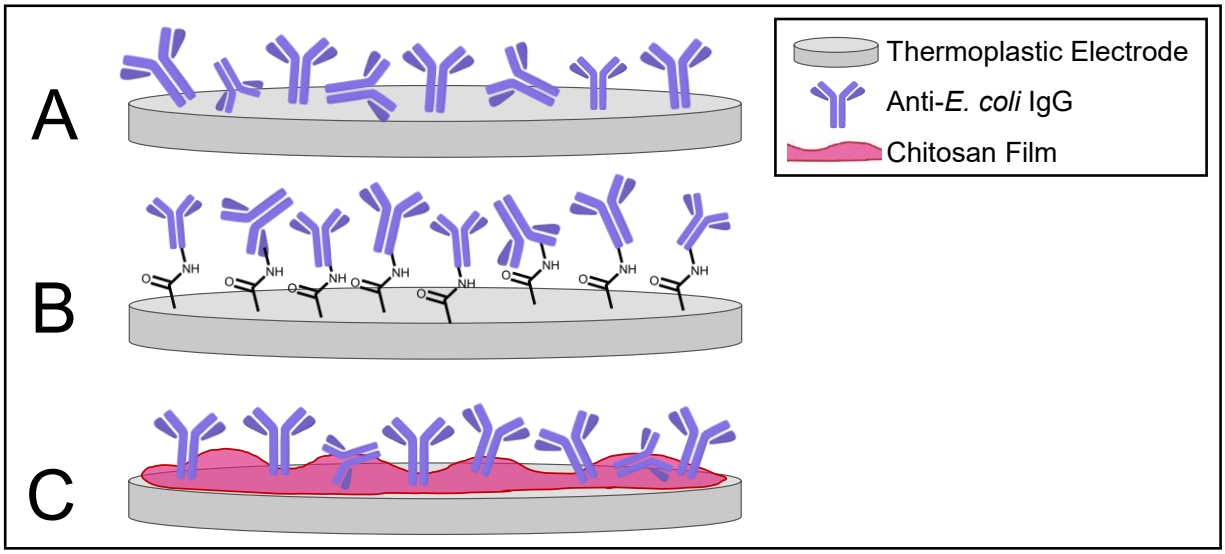

Figure 2.1. Antibody immobilization techniques: A) passive adsorption, B) EDC/NHS coupling, and C) chitosan film crosslinking.

Surface chemistry and structure is of considerable importance when determining the best approach for antibody immobilization. Recently, TPE surface chemistry was characterized using scanning electrochemical microscopy (SEM), cyclic voltammetry (CV), and X-ray photoelectron spectroscopy (XPS) for environmental sensing applications. It was determined that the binder and graphite type play a significant role in the function of the TPE with regards to anodic stripping voltametric determination of lead.[18] It is expected that the surface roughness (R_q) and composition similarly impact antibody immobilization. For example, one binder used for TPE fabrication,

polycaprolactone (PCL), contains carbonyl groups which are required for EDC/NHS coupling and can enhance intermolecular interactions for adsorption based techniques. On the other hand, polystyrene (PS) electrodes have better electrochemical performance which is believed to be a result of π-π stacking.[18] Here, three approaches to antibody immobilization are explored for establishing TPE immunosensors using PCL-based TPEs.

2.3 Materials and Methods

Electrode Fabrication

TPEs were fabricated according to previous methods.[2, 19] TC303 graphite from Asbury Graphite Mills, Inc. (Asbury, NJ) was mixed with either polystyrene (PS, average MW 45,000 from Sigma Aldrich, St. Louis, MO) or polycaprolactone (PCL, ThermoMorph®, Toledo, OH) dissolved in dichloromethane (DCM, Avantor performance Materials, Radnor, PA). Mass ratio of 2:1 graphite to thermoplastic were used. The resulting mixtures were dried completely before being pressed into a polymethylmethacrylate (PMMA, Fort Collins Plastics, Fort Collins, CO) template using a hydraulic heat press. Excess electrode material was sanded away before attaching wires with conductive silver paint (SPI Supplies, West Chester, PA) and topped with 2-part epoxy (Loctite®, Henkel Corp., Rocky Hill, CT) to seal and protect the connections. Each electrode was polished before use with wet 150 then 600 grit silicon carbide sandpaper (60 seconds each) and sonicated in MilliQ water for 5 minutes. A Palmsens4 (Palmsens BV, Houten, Netherlands) potentiostat was used for all measurements with a TPE pseudo-reference and TPE counter electrode. TPEs used were similar in design to **Figure 2.2** where one array contains four sets of 3-electrode systems (1 mm WE, 1 mm RE, and

1.5 mm CE). Chitosan and gold nanoparticle experiments used TPE arrays with larger electrode diameters (3 mm WE, 3 mm RE, and 4.5 mm CE).

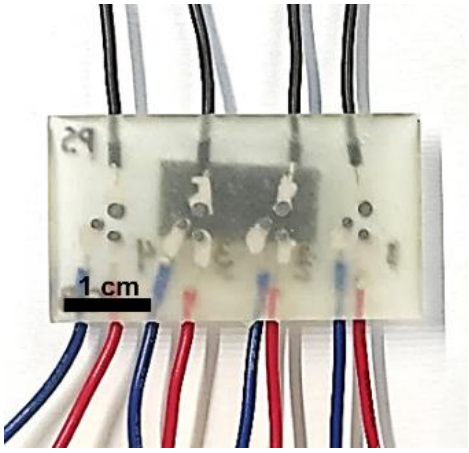

Figure 2.2. Photo of a PS TPE array of four 3-electrode systems in a PMMA template.

Stencil printed carbon electrodes (SPCEs) were used for higher throughput experiments due to their similar composition to TPEs. SPCEs were made as previously reported using commercial carbon ink (E3178, Ercon, Inc., Wareham, MA) and TC303 graphite.[20, 21] Silver/silver chloride paste (Sigma Aldrich, St. Louis, MO) was added to the reference electrode.

Passive Adsorption

A 10 µL aliquot of 20 µg/mL anti-*E. coli* IgG antibody (Abcam, Inc., Cambridge, UK) solution in 10 mM phosphate buffered saline (PBS, pH = 7.4, ThermoFisher Scientific, Waltham, MA) was added to the working electrode only of the TPE and left at room temperature for 2 hours. After incubation, the electrodes were rinsed with approximately 15 mL of 10 mM PBS via transfer pipette. Square wave voltammetry (SWV) was used with a potential sweep from -0.3 to 0.3 V with 2 sec equilibration time, 0.002 V

step, 0.05 V amplitude, and 10.0 Hz frequency. For the *E. coli* experiment, only PCL TPEs were used, and they were plasma treated for 2 min at 125 W prior to use for activation. DH5α *E. coli* samples were prepared by isolating bacteria from growth media by centrifuging and resuspending in 10 mM PBS at a 1:2 dilution yielding approximately 1x10^4 CFU/mL. The antibody modified electrodes were exposed to 10 µL of 10 mM PBS or *E. coli* solution for 40 minutes before rinsing with 10 mM PBS prior to measurement using SWV with 5 mM $Fe(CN)_6^{3-/4}$ in 10 mM PBS.

EDC/NHS Coupling

A reaction solution of 2.5 mM each of N-(3-dimethylaminopropyl)-N′-ethylcarbodiimide hydrochloride (EDC, Sigma Aldrich, St. Louis, MO) and N-hydroxysulfosuccinimide (NHS, Sigma Aldrich, St. Louis, MO) was made in MilliQ H_2O. Each working electrode received 20 µL of EDC/NHS for 45 min at room temperature. The reaction mixture was pipetted off and then 20 µL of 10 µg/mL anti-*E. coli* IgG antibody was added for 1 hr at room temperature. Antibody concentration was optimized by varying the concentration from 1 µg/mL to 50 µg/mL. The electrodes were washed with PBS followed by PBS with 0.1% TWEEN® 20 (Sigma Aldrich, St. Louis, MO) applied via spray bottle. For blocker optimization, 50 µL of blocker was added to the working electrode for 1 hr. Blockers were 0.3% aged casein (Sigma Aldrich, St. Louis, MO) in 50 mM borate buffer, pH 8.5 (Sigma Aldrich, St. Louis, MO),[11, 22] 0.5% bovine serum albumin (BSA, Equitech-Bio, Inc., Kerrville, TX) in PBS, and SuperBlock™ PBS Blocking Buffer (ThermoFisher Scientific, Waltham, MA). The blocker was pipetted off and electrodes were gently washed with PBS via transfer pipette prior to incubation in 1x10^4 CFU/mL DH5α *E. coli* prepared as before. SWV was performed in 5 mM $Fe(CN)_6^{3-/4}$ in 10 mM PBS.

Square wave voltammetry (SWV) was used with a potential sweep from -0.2 to 0.5 V with 2 sec equilibration time, 0.002 V step, 0.05 V amplitude, and 10.0 Hz frequency.

Chitosan Films

Stock solutions of 1% w/v chitosan (low molecular weight, Sigma Aldrich, St. Louis, MO) in 2% by volume of acetic acid (ThermoFisher Scientific, Waltham, MA) were mixed overnight at room temperature prior to use. A 15 µL aliquot of chitosan solution was added to the working electrode only and allowed to dry overnight at room temperature. Chitosan-coated TPEs were activated by adding 15 µL of glutaraldehyde (ThermoFisher Scientific, Waltham, MA) for 30 min. Concentrations of both chitosan and glutaraldehyde were varied to determine the optimal conditions. The WE was rinsed with approximately 5 mL of DI water via transfer pipette prior to addition of 15 µL of antibody solution (anti-*E. coli* IgG, Abcam, Inc., Cambridge, UK).

Cyclic voltammetry (CV) was done in 10 mM $Fe(CN)_6^{3-/4}$ in 0.1 M KCl (Sigma Aldrich, St. Louis, MO) with sweeps in the positive direction from -0.4 V to 0.4 V with 2 sec equilibration time, 0.01 V step, and 0.05 V/s scan rate. Chronoamperometry was performed in TMB solution at 0.0 V for 120.0 sec with 0.01 sec intervals. Scanning electron microscopy (SEM) was performed using a JEOL JSM-6500F Field Emission Scanning Electron Microscopy in secondary electron imaging mode with 15 kV accelerating voltage. Samples were prepared by gold coating with a 10 nm layer using a Denton Vacuum Desk II gold sputter coater.

2.4 Results and Discussion

Passively Adsorbed Antibodies

The simplest approach to adding antibodies to carbon electrodes is to passively adsorb the antibodies, relying on intermolecular forces and hydrodynamic forces to keep the antibodies on the electrodes. Two different TPE types were tested PS-TC303 and PCL-TC303 knowing that they have different surface chemistries.[18] Shown in **Figure 2.3** are the bare versus antibody adsorbed electrodes for both PS and PCL type polymers. The change in signal was calculated by **Equation 2.1**. The signal significantly decreases with the adsorption of antibodies blocking the electron transfer from $Fe(CN)_6^{3-/4-}$ as expected.

$$\left(\frac{i_{Ab\ modified} - i_{Bare}}{i_{Bare}}\right) * 100 = \%\ \text{Change in Peak Current} \qquad \textbf{(Equation 2.1)}$$

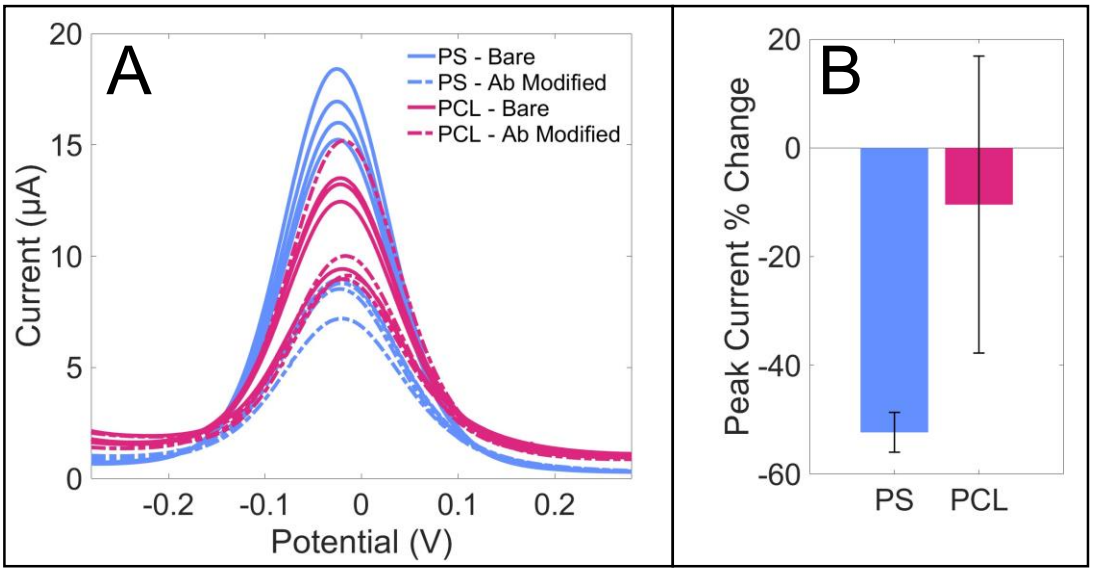

Figure 2.3. (A) Square wave voltammograms in 1 mM $Fe(CN)_6^{3-/4-}$ (in 10 mM PBS) of bare and antibody adsorbed TPEs made from polystyrene (PS) or polycaprolactone (PCL), n=3. Potential is versus a TPE pseudo-reference. The percent change in peak current (B) shows that antibodies are much more consistently adsorbed to PS based TPEs than PCL.

PS electrodes had a much larger difference between the bare and antibody modified electrode. This is potentially due to the higher electrochemical signal with PS initially (when comparing bare signals). The antibody modified signal between both electrode types was nearly identical with the exception of one PCL electrode that may be an outlier, but more replicates would be needed for confirmation. Since PCL electrodes are easier to fabricate with the lower melting point and the antibody modified signals were comparable, we decided to move forward with PCL TPEs. Further, the PCL electrodes were plasma treated to increase electrochemical performance to be comparable to that of PS prior to antibody adsorption. Previous work demonstrated the utility of plasma treating stencil-printed carbon electrodes, in which plasma treatment etched away binder to reveal more carbon active sites.[20] A similar phenomenon is hypothesized to occur in TPEs.

Initial tests using TPEs modified with passively adsorbed antibodies were conducted using 1 x 10^4 CFU/mL *E. coli* in 10 mM PBS (pH = 7.4) on plasma-treated PCL electrodes. **Figure 2.4** shows the average peak currents from square wave voltammograms taken in 5 mM $Fe(CN)_6^{3-/4-}$ (in 10 mM PBS) for modified TPEs exposed to blank (PBS buffer only, n=3) and 1 x 10^4 CFU/mL *E. coli* in 10 mM PBS (n=4). Notably, the average peak current for the *E. coli* exposed group is higher than the PBS blank which is the opposite of the typical trend for label free immunosensors where binding of the target antigen should block the redox probe from undergoing oxidation/reduction at the electrode surface. There are two possible reasons for this phenomenon. The first is that the redox probe can be accumulated beneath the *E. coli* layer on the electrode surface and be prevented from diffusing away from the surface quickly resulting in a higher concentration of $Fe(CN)_6^{3-/4-}$ at the surface. Accumulation and rejection mode hypotheses

are illustrated in **Figure 2.5.** Rejection mode is the expected and most common form of label free immunosensor mechanisms where the binding of the relatively large target analyte prevents electron transfer of $Fe(CN)_6^{3-/4-}$ at the electrode surface.

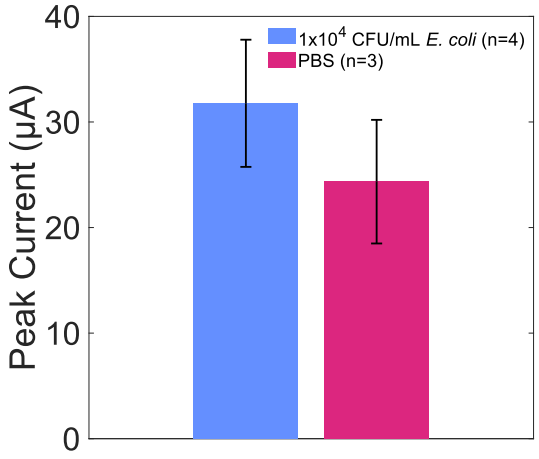

Figure 2.4. Peak currents from SWV (using 5 mM $Fe(CN)_6^{3-/4}$ in 10 mM PBS) of plasma treated PCL TPEs that were modified with passively adsorbed antibodies before being incubated with either PBS blank (pink, n=3) or 1x10⁴ CFU/mL *E. coli* (blue, n=4).

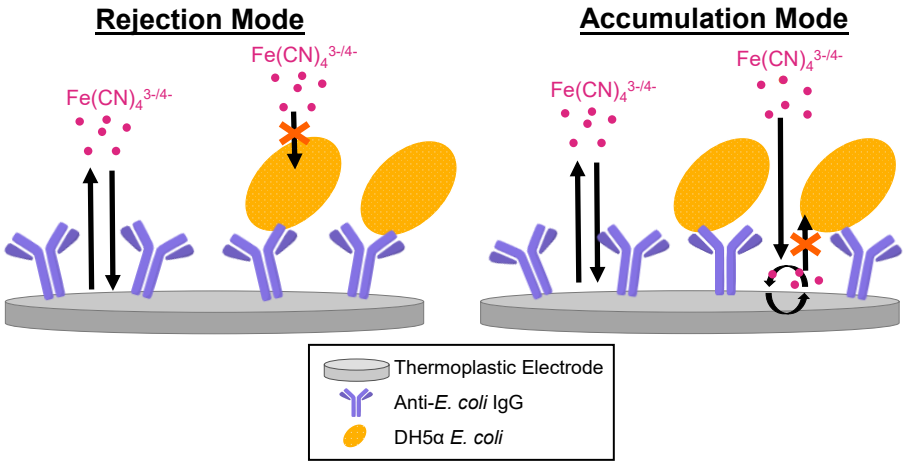

Figure 2.5. Illustration of the hypothesized mechanisms for label-free sensing using an electrochemical immunosensor.

The second hypothesis is that the binding of the relatively large *E. coli* causes the antibodies to desorb from the surface and then be washed away during a rinse step prior to measurement. However, the results shown in **Figure 2.4** are not statistically significant and were not effectively reproducible so we concluded that a more robust method of antibody immobilization should be tested.

EDC/NHS Coupling

Crosslinking using N-(3-dimethylaminopropyl)-N′-ethylcarbodiimide hydrochloride (EDC) with N-hydroxysulfosuccinimide (NHS) is a commonly used technique is attractive due to the zero-length covalent bonds formed between the antibodies and the electrode surface.[23] Initial testing with this approach was done on stencil-printed carbon electrodes (SPCEs) due to their ease of assembly so that we can test many variables in optimizing the reactions while spending less time fabricating new electrode batches. It is hypothesized that using the same graphite type limits differences between SPCEs and TPEs and the crosslinking reaction could be translated easily.

We saw a consistent decrease in signal when performing SWV before and after antibody immobilization with EDC/NHS on SPCEs and TPEs. **Figure 2.6** shows the average peak currents from SWV taken in 10 mM $Fe(CN)_6^{3-/4}$ in 10 mM PBS on SPCEs. Notably, the reaction of EDC/NHS on the electrode surface (with no antibodies present) caused an increase in the peak current. It is hypothesized there is formation of N-acylisourea derivative at the surface which may enhance the electrochemical behavior.[23] Upon immobilizing antibody via EDC/NHS, the signal is returned to be comparable to the bare electrode. Further testing would be needed, potentially via XPS, to confirm that antibodies are present.

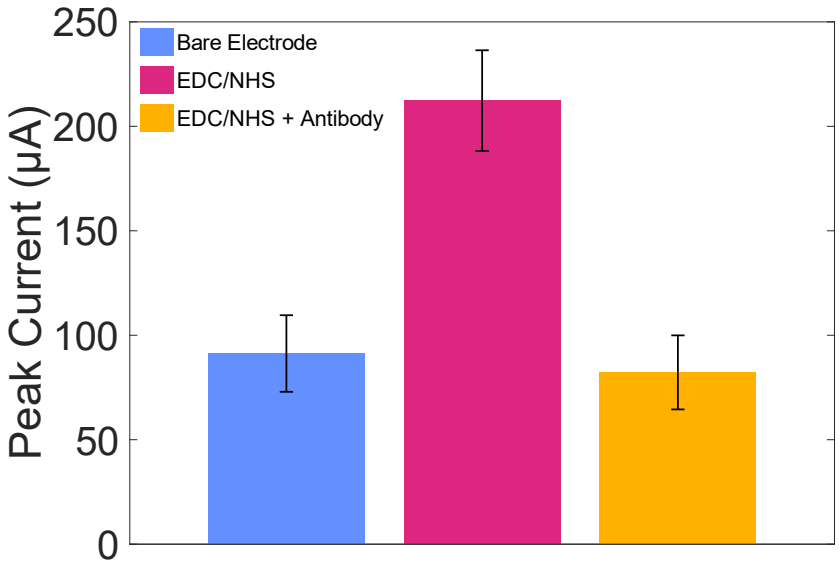

Figure 2.6. Average peak current for bare SPCEs (blue, n=6), EDC/NHS modified SPCEs (pink, n=6), and antibody immobilize SPCEs (yellow, n=3). SWV was done using 10 mM $Fe(CN)_6^{3-/4}$ in 10 mM PBS.

Subsequently, antibody concentration optimization was attempted. Anti-E. coli IgG antibody concentration was varied from 1 μg/mL to 50 μg/mL. After incubation and a wash step, 0.5% BSA was used as a blocker and the SPCEs were incubated in approximately 1 x 10^6 CFU/mL *E. coli*. The final electrodes were tested via SWV in 5 mM $Fe(CN)_6^{3-/4}$ and average change in peak currents are shown in **Figure 2.7**. The changes in peak currents were calculated using **Equation 2.1** from measurements made before and after incubation in either PBS (blank) or *E. coli*. It was expected for the blank to have a peak current change near zero as nothing should be changing the surface of the electrode. At concentrations less than 50 μg/mL, this was supported with relatively small changes in the peak current for the blanks. However, it was expected that the incubation of *E. coli* on the antibody modified electrodes would result in relatively large changes in peak current in the negative direction. This was only observed at 1 μg/mL and 20 μg/mL. Regardless, the variation in this experiment (represented as standard deviation by the

error bars) made the results inconclusive. We moved forward with 10 µg/mL of antibody due to success seen in other carbon-electrode based immunsensors.[11, 24, 25]

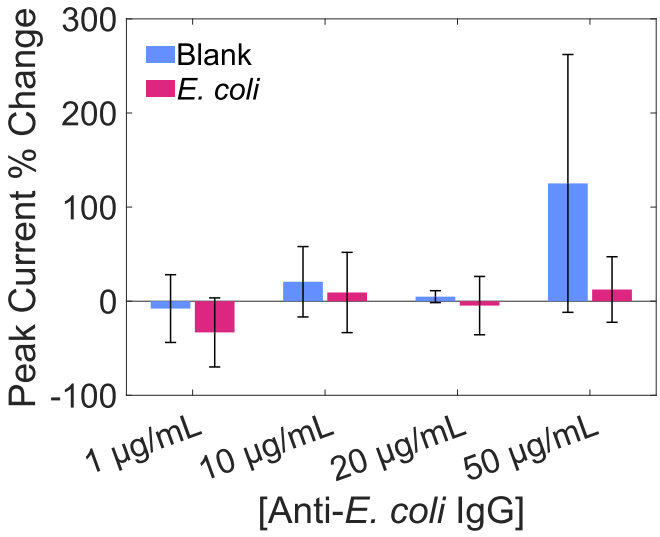

Figure 2.7. Peak current percent change from before and after incubation with PBS (blank, blue) or 1 x 10^6 CFU/mL *E. coli* (pink). Concentration of antibody immobilized varied from 1 µg/mL to 50 µg/mL. n = 3 for each concentration and test group.

One hypothesis for the cause of the wide variations in **Figure 2.7** is ineffective blocking of nonspecific adsorption. It is possible that the blocker used was preventing the target, *E. coli*, from binding and was not consistently coating the electrodes. First, three blocker types were investigated (**Figure 2.8a**) including 0.3% aged casein (AC), SuperBlock™, and 0.5% bovine serum albumin (BSA). Again, peak current percent changes were calculated as in Equation 1 for the signals before and after modifications and incubation in either PBS (blank) or 1 x 10^6 CFU/mL *E. coli* were taken from SWV using 10 mM $Fe(CN)_6^{3-/4-}$. Both SuperBlock™ and the negative control (no blocker) appeared to have an accumulation mode response (**Figure 2.5**) where the *E. coli* incubated electrodes had a peak current percent change resulting in a higher signal than

the blank. AC and BSA demonstrated slight, but not statistically significant, rejection mode (**Figure 2.5**) where the signal for the *E. coli* incubated electrodes was lower than that of the blanks. Passivation of the electrode with the binding of the target is more widely understood and accepted hypothesized sensing mechanism, so we more closely studied AC and BSA blocking conditions (**Figure 2.8B**). Time and concentration were varied and the resulting peak currents for SPCEs following incubation in PBS or E. coli in 10 mM $Fe(CN)_6^{3-/4-}$ are shown. The 1 hour with 1% BSA condition performed the best with relatively low variation and the expected signal decrease from the blank to the target.

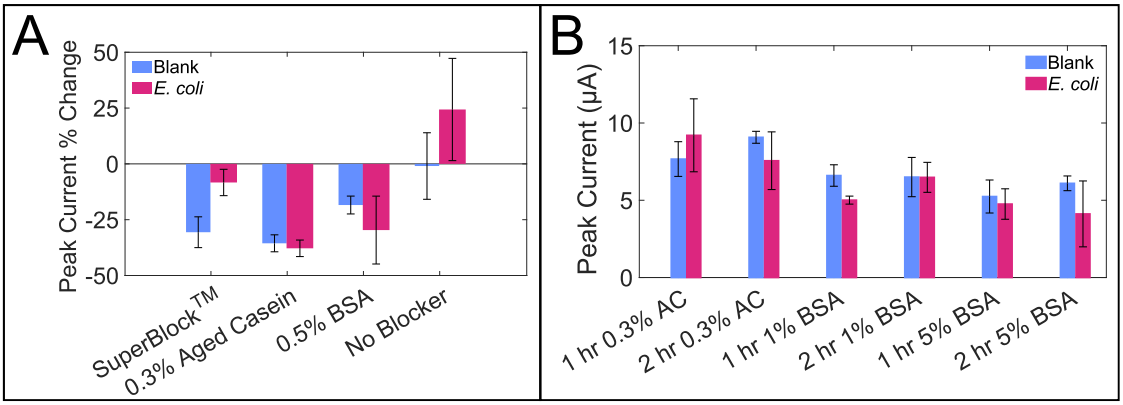

Figure 2.8. (A) Comparison of blocker types on SPCEs with antibodies immobilized via EDC/NHS for detection of *E. coli* using peak current percent change from before and after incubation with PBS or E. coli using SWV in 10 mM $Fe(CN)_6^{3-/4-}$. **(B)** Comparison of aged casein (AC) and bovine serum albumin (BSA) at 1 and 2 hours. Peak currents were measured using SWV in 10 mM $Fe(CN)_6^{3-/4-}$.

However, we did not achieve reproducible statistical significance when working to detect *E. coli* using EDC/NHS as the antibody immobilization technique. The EDC/NHS reaction in aqueous conditions is prone to hydrolysis and may facilitate many side reactions due to the nonspecific linkages between carboxylates and amines.[23] It is possible that these side reactions were outcompeting the antibody linkage reaction and preventing

enough antibodies from binding to create a consistent electrochemical immunosensor. Alternative immobilization techniques were investigated to avoid the problems of the facile hydrolysis of EDC.

Chitosan Films

The chitosan film approach can be considered a hybrid between passive adsorption and EDC/NHS crosslinking. First, a chitosan solution is dropcast onto the TPE and allowed to dry in a simple, 1-step process. The chitosan is attached to the carbon TPE surface by intermolecular forces similar to passively adsorbed antibodies. The dried chitosan film is then activated by the addition of glutaraldehyde which induces the formation of aldehydes which react with amines on neighboring chitosan molecules or antibodies to form imines as illustrated in **Figure 2.9**.[26, 27] It has been suggested that antibody immobilization by this approach may help with antibody stability with less than 10% signal loss in one groups sensors after storage for five days.[6]

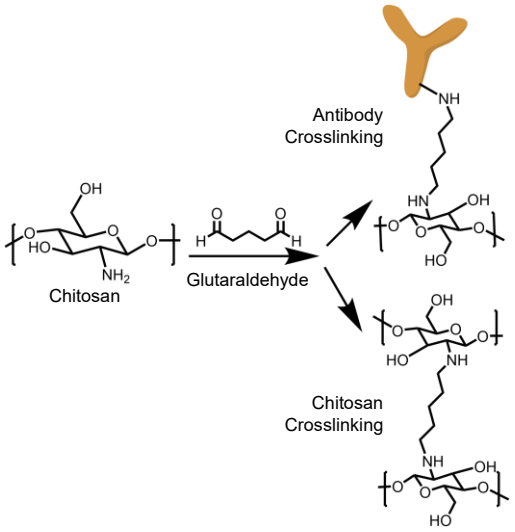

Figure 2.9. Chitosan crosslinking mechanism for immobilizing antibodies via activation with glutaraldehyde.

First, the chitosan coating required optimization to determine the best coverage while limiting passivation of the electrode. The concentration of chitosan (w/v) was varied from 0% to 0.1% and the resulting dried films were examined via scanning electron microscopy (SEM) as shown in **Figure 2.10**. At 200x magnification there is not an appreciable difference between amounts of chitosan. However, at 2000x magnification, it is seen that the 0.1% chitosan modified TPE has a smoother appearance with filled gaps and softened edges compared to the bare electrode with 0% chitosan. The 0.01% and 0.05% are not greatly different than that of the bare electrode.

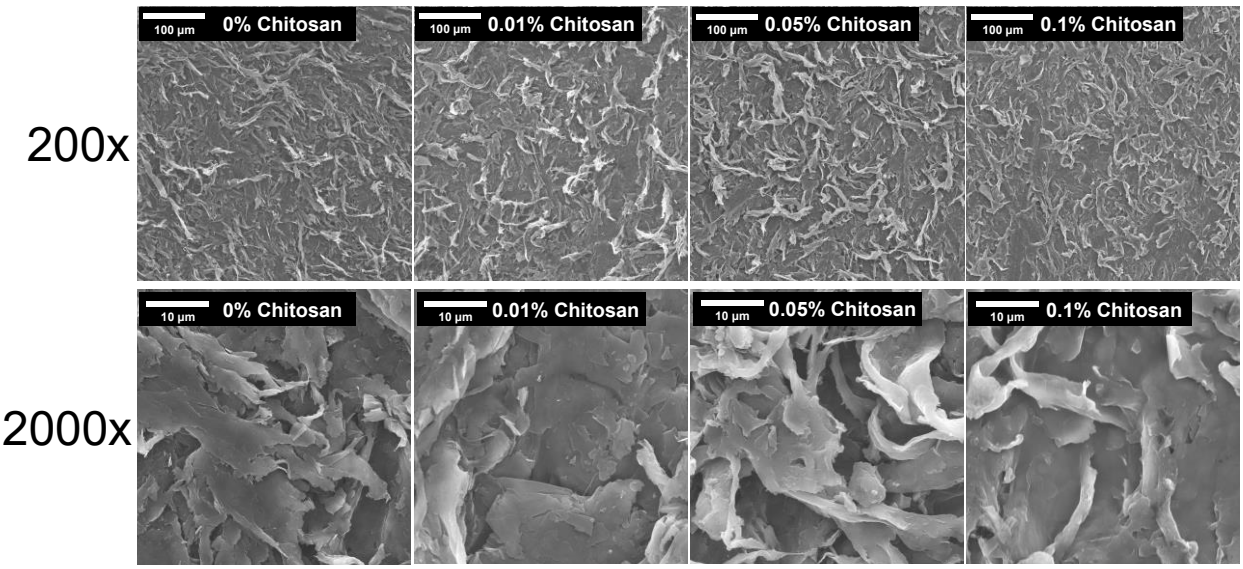

Figure 2.10. Scanning electron micrographs, 5 kV accelerating voltage, at 200x and 2000x magnification demonstrating 0%, 0.01%, 0.05%, and 0.1% chitosan solutions dried onto TPEs.

The electrochemical signal was severely impacted with 0.1% chitosan (not shown); thus, it was immediately ruled out as a being too high of a chitosan concentration. Electrodes coated with 0%, 0.01%, and 0.05% chitosan were activated with 2.5% glutaraldehyde, and antibodies were immobilized before cyclic voltammetry was done to

observe the resulting impacts on electrochemical performance (**Figure 2.11**). As expected, there is a decrease in signal as the concentration, and coating density, on the electrode is higher. The 0.05% chitosan condition was chosen as it showed some evidence of a film in SEM while maintaining an electrochemical signal on the electrode.

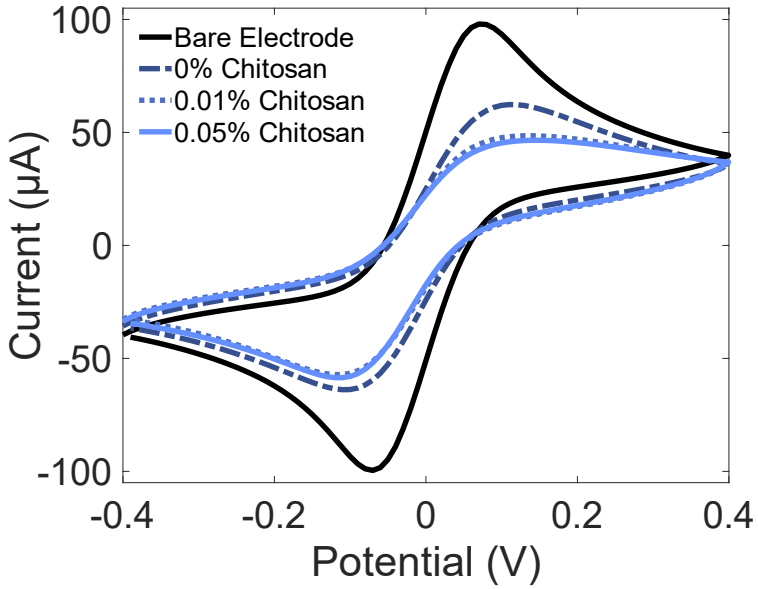

Figure 2.11. Representative CVs of modified electrodes with varied concentration of chitosan taken in 10 mM $Fe(CN)_6^{3-/4-}$ in 0.1 M KCl at a scan rate of 0.05 V/s. Potential is versus a TPE pseudo-reference.

Next, glutaraldehyde concentration (v/v%) was optimized. Representative cyclic voltammograms for 1%, 2.5%, and 5% glutaraldehyde activation are shown in **Figure 2.12A**. The 1% and 5% glutaraldehyde conditions follow the expected trend where the signal is lower than the bare electrode. However, the 2.5% glutaraldehyde treated TPE had similar response to the bare electrode. Peak currents of the oxidation reaction are shown in **Figure 2.12B**. It is hypothesized that this is the result of random error in the small sample size (n=3). The 5% condition had the smallest variation and the largest

decrease in signal, indicating that more antibody was immobilized, and more chitosan crosslinked to result in a thicker coating on the TPE surface. Thus, we determined 5% glutaraldehyde to be the ideal condition.

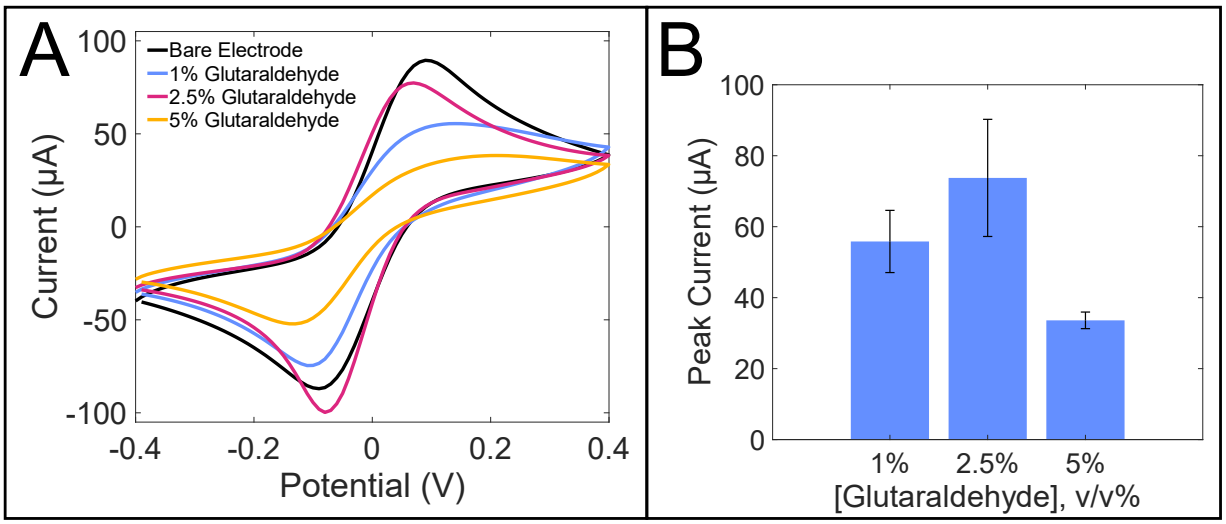

Figure 2.12. (A) Representative cyclic voltammograms in 5 mM $Fe(CN)_6^{3-/4-}$ in 0.1 M KCl at 0.05 mV/s with a TPE pseudo-reference. **(B)** Average peak currents (n=3) for each concentration of glutaraldehyde used for activation of the chitosan film for antibody immobilization.

Overall, the chitosan film modification passivated the electrode too much for it to be a successful label-free sensor. The signal of the modified electrode in redox solution was too low for there to be much room for reduced signal in the presence of target analyte via the typical rejection mode sensing. Dr. Thaisa Baldo (Colorado State University) and Dr. Vanessa Ataide (University of São Paolo) continued the chitosan work to examine the utility of the modification with the addition of a carbon black to function as a conductive media to aid in electrochemical performance.

2.5 Conclusions

Overall, traditional approaches to antibody immobilization such as passive adsorption, EDC/NHS crosslinking, and chitosan films were unsuccessful on TPEs. Passive adsorption was shown to be a simple approach however it is limited in performance due to limited active antibodies and weak attachments to the TPE surface. The EDC/NHS crosslinking offered an attractive solution to weak attachments but was shown to be unreliably prone to side reactions. The chitosan film approach was simple with limited side reactions, but ultimately blocked the electrode surface too much with a layer that was optimal for antibody attachment. The conclusion then is that an alternative method is required for efficient antibody immobilization on TPEs. The ideal method has strong covalent bonding, limited side reactions, and consistent results without extensive passivation of the electrode.

References

1. McMahon, C.; Martinez, B.; Henry, C. S., Surface modification of thermoplastic electrodes for electrochemical immunosensors. In *American Chemical Society Fall Meeting*, Chicago, Illinois, 2022.

2. McCord, C. P.; Summers, B.; Henry, C. S., Simultaneous Analysis of Ascorbic Acid, Uric Acid, and Dopamine at Bare Polystyrene Thermoplastic Electrodes. *ChemElectroChem* **2022,** *9* (11), e202101600.

3. Clark, K. M.; Henry, C. S., Thermoplastic Electrode (TPE)-based Enzymatic Glucose Sensor Using Polycaprolactone-graphite Composites. *Electroanalysis* **2021,** *n/a* (n/a).

4. Ozer, T.; Henry, C. S., All-solid-state potassium-selective sensor based on carbon black modified thermoplastic electrode. *Electrochimica Acta* **2022,** *404*, 139762.

5. Ozer, T.; McCord, C.; Geiss, B. J.; Dandy, D.; Henry, C. S., Thermoplastic Electrodes for Detection of Escherichia coli. *Journal of The Electrochemical Society* **2021,** *168* (4), 047509.

6. Sharafeldin, M.; McCaffrey, K.; Rusling, J. F., Influence of antibody immobilization strategy on carbon electrode immunoarrays. *Analyst* **2019,** *144* (17), 5108-5116.

7. Shen, M.; Rusling, J.; Dixit, C. K., Site-selective orientated immobilization of antibodies and conjugates for immunodiagnostics development. *Methods* **2017,** *116*, 95-111.

8. Patel, M.; Agrawal, M.; Srivastava, A., Signal amplification strategies in electrochemical biosensors via antibody immobilization and nanomaterial-based transducers. *Materials Advances* **2022,** *3* (24), 8864-8885.

9. Butler, J. E.; Ni, L.; Brown, W. R.; Joshi, K. S.; Chang, J.; Rosenberg, B.; Voss, E. W., The immunochemistry of sandwich elisas—VI. Greater than 90% of monoclonal and 75% of polyclonal anti-fluorescyl capture antibodies (CAbs) are denatured by passive adsorption. *Molecular Immunology* **1993,** *30* (13), 1165-1175.

10. Vashist, S. K., Comparison of 1-Ethyl-3-(3-Dimethylaminopropyl) Carbodiimide Based Strategies to Crosslink Antibodies on Amine-Functionalized Platforms for Immunodiagnostic Applications. *Diagnostics (Basel)* **2012,** *2* (3), 23-33.

11. Samper, I. C.; McMahon, C. J.; Schenkel, M. S.; Clark, K. M.; Khamcharoen, W.; Anderson, L. B. R.; Terry, J. S.; Gallichotte, E. N.; Ebel, G. D.; Geiss, B. J.; Dandy, D. S.; Henry, C. S., Electrochemical Immunoassay for the Detection of SARS-CoV-2 Nucleocapsid Protein in Nasopharyngeal Samples. *Analytical Chemistry* **2022,** *94* (11), 4712-4719.

12. Eissa, S.; L'Hocine, L.; Siaj, M.; Zourob, M., A graphene-based label-free voltammetric immunosensor for sensitive detection of the egg allergen ovalbumin. *Analyst* **2013,** *138* (15), 4378-4384.

13. Białobrzeska, W.; Firganek, D.; Czerkies, M.; Lipniacki, T.; Skwarecka, M.; Dziąbowska, K.; Cebula, Z.; Malinowska, N.; Bigus, D.; Bięga, E.; Pyrć, K.; Pala, K.; Żołędowska, S.; Nidzworski, D., Electrochemical Immunosensors Based on Screen-Printed Gold and Glassy Carbon Electrodes: Comparison of Performance for Respiratory Syncytial Virus Detection. *Biosensors* **2020,** *10*.

14. Jarocka, U.; Radecka, H.; Malinowski, T.; Michalczuk, L.; Radecki, J., Detection of Prunus Necrotic Ringspot Virus in Plant Extracts with Impedimetric Immunosensor based on Glassy Carbon Electrode. *Electroanalysis* **2013,** *25* (2), 433-438.

15. Öztop, H. N.; Saraydin, D.; Cetinus, Ş., pH-sensitive chitosan films for baker's yeast immobilization. *Applied Biochemistry and Biotechnology* **2002,** *101* (3), 239-249.

16. Yuan, W.; Dong, H.; Li, C. M.; Cui, X.; Yu, L.; Lu, Z.; Zhou, Q., pH-Controlled Construction of Chitosan/Alginate Multilayer Film: Characterization and Application for Antibody Immobilization. *Langmuir* **2007,** *23* (26), 13046-13052.

17. Miao, Y.; Tan, S. N., Amperometric hydrogen peroxide biosensor based on immobilization of peroxidase in chitosan matrix crosslinked with glutaraldehyde. *Analyst* **2000,** *125* (9), 1591-1594.

18. McMahon, C. J.; Martinez, B.; Henry, C. S., Characterization of Factors Affecting Stripping Voltammetry on Thermoplastic Electrodes. *Journal of The Electrochemical Society* **2023**.

19. Klunder, K. J.; Nilsson, Z.; Sambur, J. B.; Henry, C. S., Patternable Solvent-Processed Thermoplastic Graphite Electrodes. *Journal of the American Chemical Society* **2017,** *139* (36), 12623-12631.

20. Kava, A. A.; Henry, C. S., Exploring carbon particle type and plasma treatment to improve electrochemical properties of stencil-printed carbon electrodes. *Talanta* **2021,** *221*, 121553.

21. Kava, A. A.; Beardsley, C.; Hofstetter, J.; Henry, C. S., Disposable glassy carbon stencil printed electrodes for trace detection of cadmium and lead. *Analytica Chimica Acta* **2020,** *1103*, 58-66.

22. Grant, B. D.; Anderson, C. E.; Williford, J. R.; Alonzo, L. F.; Glukhova, V. A.; Boyle, D. S.; Weigl, B. H.; Nichols, K. P., SARS-CoV-2 Coronavirus Nucleocapsid Antigen-Detecting Half-Strip Lateral Flow Assay Toward the Development of Point of Care Tests

Using Commercially Available Reagents. *Analytical Chemistry* **2020,** *92* (16), 11305-11309.

23. Hermanson, G. T., Chapter 4 - Zero-Length Crosslinkers. In *Bioconjugate Techniques (Third Edition)*, Hermanson, G. T., Ed. Academic Press: Boston, 2013; pp 259-273.

24. Yang, Y.; Liu, Q.; Liu, Y.; Cui, J.; Liu, H.; Wang, P.; Li, Y.; Chen, L.; Zhao, Z.; Dong, Y., A novel label-free electrochemical immunosensor based on functionalized nitrogen-doped graphene quantum dots for carcinoembryonic antigen detection. *Biosensors and Bioelectronics* **2017,** *90*, 31-38.

25. Mao, K.; Wu, D.; Li, Y.; Ma, H.; Ni, Z.; Yu, H.; Luo, C.; Wei, Q.; Du, B., Label-free electrochemical immunosensor based on graphene/methylene blue nanocomposite. *Analytical Biochemistry* **2012,** *422* (1), 22-27.

26. Woźniak, A.; Biernat, M., Methods for crosslinking and stabilization of chitosan structures for potential medical applications. *Journal of Bioactive and Compatible Polymers* **2022,** *37* (3), 151-167.

27. Cotchim, S.; Thavarungkul, P.; Kanatharana, P.; Limbut, W., Multiplexed label-free electrochemical immunosensor for breast cancer precision medicine. *Analytica Chimica Acta* **2020,** *1130*, 60-71.

CHAPTER 3 – Surface Modification of Thermoplastic Electrodes for Biosensing Applications via Copper-Catalyzed Click Chemistry

3.1 Overview

After studies to examine options for antibody immobilization on thermoplastic electrodes proved difficult, as shown in Chapter 2, the focus shifted to using click chemistry for modifying the surface of the thermoplastic electrodes (TPEs). Cu(I)-catalyzed 1,3-dipolar cycloaddition (CuAAC), aka click chemistry, has been demonstrated to be highly robust while providing versatile surface chemistry. One specific application is biosensor fabrication. Recently, we developed TPEs as an alternative to traditional carbon composite electrodes in terms of cost, performance, and robustness. However, their applications in biosensing are currently limited due to lack of facile methods for electrode modification. Here, we demonstrate the feasibility of using CuAAC following diazonium grafting of thermoplastic electrodes (TPEs) to take advantage of two powerful technologies for developing a customizable and versatile biosensing platform. After performing a stepwise characterization of the electrode modification procedures, electrodes were modified with model affinity reagents. Streptavidin and streptavidin-conjugated IgG antibodies were successfully immobilized on the TPE surface as confirmed by electrochemical impedance spectroscopy (EIS) and X-ray photoelectron spectroscopy (XPS).

The work presented in this chapter was completed in collaboration with Dr. Yann R. Leroux and Dr. Philippe Hapiot of the University of Rennes. Acknowledgement is also given to the Analytical Resources Core (RRID: SCR_021758) at Colorado State University for instrument access and training for SEM and XPS. The data shown here has been

published in *ACS Applied Materials and Interfaces*.[1] Supporting information can be found in Appendix A.

3.2 Introduction

Thermoplastic electrodes (TPEs) have been shown to have a wide range of applications including ion-selective electrodes, *Escherichia coli* sensors, and enzymatic glucose sensors.[2-7] The advantage of using these carbon composite electrodes is they are robust and yield better electrochemistry than other carbon electrodes, such as screen-printed carbon electrodes (SPCEs), while being less expensive than traditional precious metal electrodes.[2] However, there is a gap in the ability to modify TPEs consistently and reliably for biosensing applications, particularly for immobilization of biorecognition elements such as antibodies and aptamers. Passive adsorption methods for antibody immobilization tend to be inconsistent due to the relatively weak intermolecular forces between the antibody and the electrode surface.[8] Covalent modification lends stronger binding and can help orientate antibodies to be able to bind the antigen. One commonly used covalent approach is (EDC)/N-hydroxysuccinimide (NHS) crosslinking.[6, 8-10] EDC/NHS has been shown to be successful on TPEs for *E. coli* detection, however, EDC/NHS chemistry can be prone to undesirable side reactions with water, primary amines, and carboxyl groups present in the system.[6, 11, 12] Thus, there is still a need for facile antibody immobilization, applicable to the highly variable surface topography and chemistries of TPEs.

Click chemistry, Cu(I)-catalyzed 1,3-dipolar cycloaddition (CuAAC), is an attractive solution and has been used in a wide variety of applications on precious metal

and carbon electrodes.[13, 14] The key to click chemistry is adding alkyne or azide functional groups on the electrode surface, which can be achieved via electroreduction of aryl diazonium ions.[15-18] Several groups have successfully applied CuAAC combined with diazonium grafting for biosensing applications on carbon electrodes using aptamers or antibodies as the biorecognition elements.[19-24] For instance, Sánchez-Tirado, *et. al.,* used alkyne-terminated IgGs to detect transforming growth factor β1 (TGF-β1) cytokine using multi-walled carbon nanotube modified SPCEs to achieve pg/mL limits of detection.[25] Success using SPCEs bolsters the motivation for exploring the CuAAC modification approach on TPEs.

One of the greatest advantages of the CuAAC approach to electrode surface modification is that it is easily customizable in terms of functional groups, pattern, film thickness, and can be performed under mild conditions.[26-28] The present study seeks to examine the performance of TPEs as an alternative to traditional electrodes with CuAAC modification following diazonium grafting as a platform for biosensing applications. Initial work using aryl diazonium grafting on TPEs was successful using organic solvents.[29] However, better electrochemical performances and easier fabrication are seen using TPE materials (polystyrene binder and polymethylmethacrylate template) that are not compatible with these solvents.[2] Diazonium grafting in water is established to be successful on TPEs here along with subsequent click chemistry-based modification with a biotin moiety for easy linkage to streptavidin conjugated nanoparticles and antibodies as a proof of concept. The multistep process allows for a well-organized monolayer film to form as a result of the aryl diazonium grafting to form a convenient linkage point for the secondary click chemistry reaction.[16]

3.3 Materials and Methods

Electrochemical Characterizations

Thermoplastic electrodes (TPEs) made of TC303 carbon (Asbury Graphite Mills Inc, NJ) and 45,000 MW polystyrene (Sigma-Aldrich, St. Louis, MO) in polymethylmethacrylate (PMMA) templates were fabricated as previously reported.[2, 5] They were prepared for each experiment by wet sanding for 30 s each in a figure-eight pattern on silicon carbide sandpaper at 150 then 600 grit. They were then sonicated in ultrapure water for 5 min and air dried before use. All electrochemical measurements were performed with Palmsens4 potentiostat (Palmsens, Houten, Netherlands). Each electrode in the 3-electrode system (counter, working, and pseudo reference) were made of the same thermoplastic electrode material with 3 mm diameter working and reference electrodes and 4.5 mm counter electrode. All data was processed and plotted using MATLAB, unless otherwise specified.

Cyclic voltammograms (CVs) were collected by adding 300 µL of 1 mM $Fe(CN)_6^{3-/4-}$ (0.5 mM of potassium hexacyanoferrate trihydrate and 0.5 mM of potassium ferricyanide, Sigma Aldrich, St. Louis, MO) in 0.1 M KCl (99.0% Sigma Aldrich, St. Louis, MO) to the electrode system and scanning at 5, 10, 20, 40, 60, 80, 100, 300, and 500 mV/s in random order. Each scan rate was tested in triplicate on separate electrodes and the process was repeated in triplicate for 1 mM ferrocenedimethanol ($Fc(MeOH)_2$, Ambeed, Arlington Heights, IL) in 0.1 M KCl.

Electrochemical impedance spectroscopy (EIS) was performed in 10 mM $Fe(CN)_6^{3-/4-}$ in 0.1 M KCl with a fixed scan type at AC potential of 0.2 V with an equilibration time of 3 s. Frequency was scanned from 0.1 Hz to 10^5 Hz with 10 points taken per frequency decade. Fits were made to the equivalent circuit using PSTrace v.5.

Surface Characterizations

Scanning electron microscopy (SEM) was used to image surfaces. Representative TPE surfaces were sputter-coated to a 10 nm thick gold layer. Secondary electron images (SEI) were collected on a JEOL JSM-6500 Field Emission Scanning Electron Microscope with 10.0 kV accelerating voltage applied. All resulting images were processed in ImageJ software. For optical profilometry measurements, a Zygo ZeScope profilometer was used with 20x magnification and ZeMaps data acquisition software. X-ray photoelectron spectroscopy (XPS) was performed on a Physical Electronics X-Ray Photoelectron Spectrometer equipped with monochromated Al anode producing Al k_α x-rays and 0.8 x 0.8 mm aperture, 20 μA electron neutralizer, and argon ion gun neutralizer. Resulting high resolution spectra were processed and analyzed via CasaXPS software.

Scanning electrochemical microscopy (SECM) was performed using a CH Instruments 920D model and 10 um diameter Pt probe, with Ag/AgCl reference, and platinum-wire counter electrode in a traditional three component system. The TPE surface was unbiased and tilt corrections were done using probe approach curves on the insulating electrode template surrounding the TPEs. Either 1 mM potassium ferrocyanide or 1 mM ferrocene dimethanol in 0.5 M KCl were used as the probe. Maps were processed using CH Instruments software and probe approach curves were fitted using simulations via MIRA software.

Electrode modification

Electrode modification throughout this work follows the general steps shown in **Figure 3.1**. First, the 4-(trimethylsilyl)ethynylbenzene diazonium salt was generated *in situ* from addition of 2 molar equivalents of sodium nitrite (99.99% metals basis, Sigma-

Aldrich, St. Louis, MO) to 10 mM of 4-(trimethylsilyl)ethynylaniline (96%, Sigma-Aldrich, St. Louis, MO) in 0.1 M HCl (ACS certified, Fisher Scientific, Waltham, MA).[30] The diazonium solution was then diluted 20-fold in 0.1 M HCl. A 100 µL aliquot was added to the TPE and electroreduction of aryl diazonium ions was performed by CV by sweeping the potential from 0 to -0.8 V with a scan rate of 50 mV/s for five cycles[16] (**Figure 3.1, Step 1**). Electrodes were rinsed thoroughly with MQ water and air dried before deprotection. Grafted electrodes were used within three days of electrografting (stored on benchtop protected from dust). The trimethylsilyl (TMS) protecting group was removed (**Figure 3.1, Step 2**) via 20 min of sonication in 1 M of NaOH (Fisher Scientific, Waltham, MA). Electrodes were rinsed thoroughly with MQ water and air dried prior to the "click" reaction.

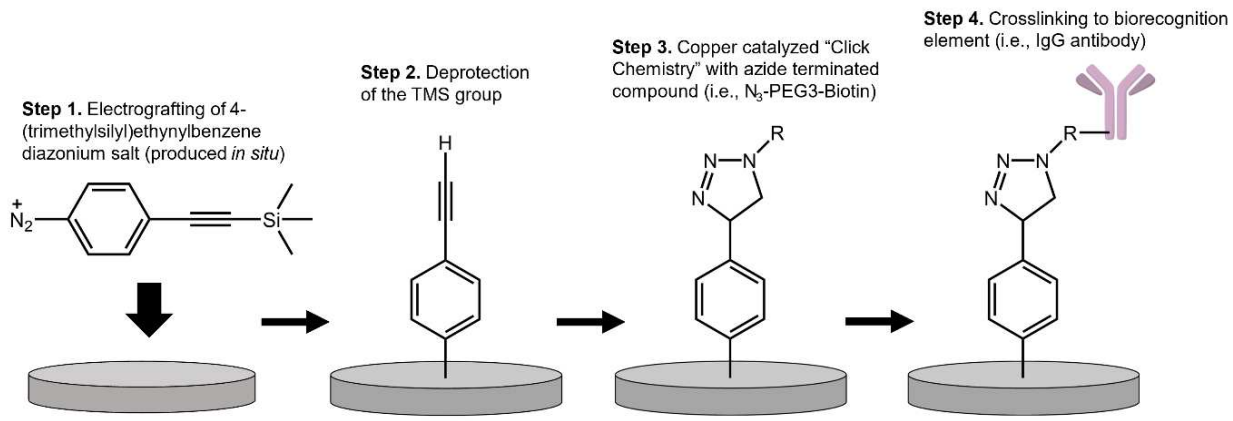

Figure 3.1. Modification workflow for the covalent functionalization of thermoplastic electrodes.

Alkyne-azide cycloaddition click chemistry was performed next (**Figure 3.1, Step 3**) with 20 mM of $CuSO_4$ (pentahydrate, 99%, Sigma-Aldrich, St. Louis, MO), 2.5 µL/mL of N_3-PEG3-N_3 (Toronto Research Chemicals, Toronto, ON) or 20 mM of N_3-PEG3-biotin (98%, BroadPharm, San Diego, CA), and 5 mM of L-ascorbic acid (Biogems International,

Westlake Village, CA). A 25 µL of each reagent was added sequentially to the working electrode only and allowed to sit at room temperature for 1 hour before rinsing with MQ water and air drying. A second click reaction was completed for electrodes modified with N_3-PEG3-N_3 with the same $CuSO_4$ and L-ascorbic acid (AA) with 20 mM of ethynylferrocene (Ambeed, Arlington Heights, IL). Concentrations of $CuSO_4$, AA, and N_3-PEG3-N_3 were optimized by determining peak signal and surface coverage, Γ_{Fc}, after clicking ethynylferrocene to the surface (see Appendix A, **Figure A.1**). Optimizations followed expected trends, where higher concentrations yielded higher surface coverage, except in the case of AA where the low pH of the higher concentration is hypothesized to have impeded the reaction.[31]

After click reactions (**Figure 3.1, Step 4**), electrodes were successively rinsed with saturated EDTA solution (pH = 8) and water (optimization available in Appendix A, **Figure A.2**). Electrodes modified with N_3-PEG3-biotin were incubated with 25 µL of 10 µg/mL of streptavidin (AnaSpec Inc., Fremont, CA, USA) or streptavidin-conjugated anti-*E. coli* IgG (Abcam, Cambridge, UK) for 30 minutes at room temperature. Anti-*E. coli* antibodies were linked to streptavidin prior to use via Lightning Link Kit (Abcam, Cambridge, UK). After incubation, the electrodes were rinsed thoroughly with water. All electrodes were used the same day that they were modified.

3.4 Results and Discussion

The surfaces of unmodified thermoplastic electrodes (TPEs) were first characterized to evaluate the composition and morphology prior to functionalization. **Figure 3.2A** shows SEM micrographs of the TPEs used in this study. The rough surface observed here is due to the polishing process applied to the TPEs before use. Through

Figure 3.2B, the electrodes were determined to have a root-mean-square roughness of the representative surface sample of R_{RMS} = 0.776 µm (average roughness, R_A = 0.575 µm). This is more than previously reported roughness values for commercial screen-printed carbon electrodes (R_A = 0.121 µm).[32] It was hypothesized that these TPEs yield high electrochemical performance due to the abundance of edge planes at the surface,[33] which effectively enhances the surface area available to electrochemical reactions. **Figure 3.2C** shows the C1s high resolution x-ray photoelectron spectrum of the TPE surface. The thermoplastic binder, polystyrene, is the primary contributor to the C1s spectrum.[34] The C1s spectrum can be peak-fitted in 3 main contributions at 284.9 eV, 285.4 eV, and 286.8 eV corresponding to C-C, C=C (50.5%), C-O (26.5%) and C=O (23.0%). The oxygen to carbon ratio (I_O/I_C) based on the XPS survey spectrum (Appendix A, **Figure A.3**) is 0.067 which is expected based on the individual spectra of the electrode components: graphite and polystyrene.[35-37]

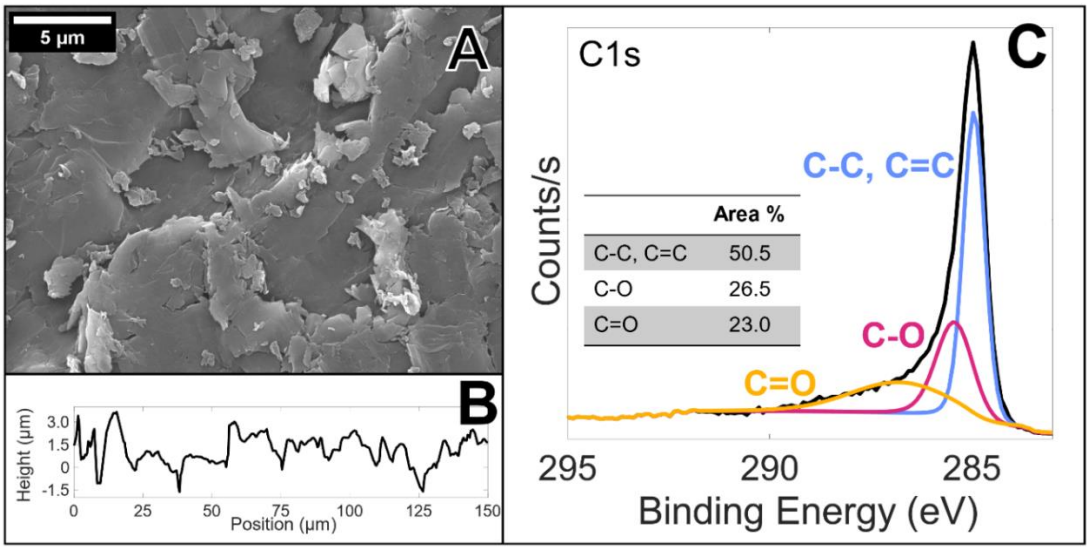

Figure 3.2. **(A)** Scanning electron micrograph at 5,000x magnification of bare TPE surface at 10.0 kV accelerating voltage. **(B)** Representative roughness profile of the TPE surface, R_{RMS} = 0.776 µm and R_A = 0.575 µm. **(C)** XPS high resolution C1s spectrum of TPE surface.

The equation (**Equation 3.1**) describing the value of the peak current for a monoelectronic reversible redox couple was used to determine the electroactive surface area using the peak current as a function of scan rate in cyclic voltammetry, where i_p is the peak current (A), F is Faraday's constant ($C \cdot mol^{-1}$), R is the ideal gas constant ($J \cdot mol^{-1} \cdot K^{-1}$), T is temperature (K), A is the electrode electroactive area (cm^2), D is the diffusion coefficient ($cm \cdot s^{-1}$), C is the concentration (M), and v is the scan rate ($V \cdot s^{-1}$).[38]

$$i_p = 0.4463 \left(\frac{F^3}{RT}\right)^{\frac{1}{2}} A D^{\frac{1}{2}} C v^{\frac{1}{2}} \qquad \textbf{(Equation 3.1)}$$

Ferri/ferrocyanide ($Fe(CN)_6^{3-/4-}$) and ferrocenedimethanol ($Fc(MeOH)_2$) were used as complementary redox probes; $Fe(CN)_6^{3-/4-}$ being an inner-sphere electron transfer probe and $Fc(MeOH)_2$ an outer-sphere electron transfer probe, giving information on both electrode surface state and kinetic of electron transfer.[39] Cyclic voltammograms and the resulting peak current versus the square root of the scan rate plots are shown in Appendix A, **Figure A.4**. The diffusion coefficients for $Fe(CN)_6^{3-/4-}$ in 0.1 M KCl were calculated using Equation 1 and the peak currents from cyclic voltammetry at 1 mV/s and assuming the area to be equivalent to the geometric area (0.0707 cm^2). The values are in agreement with literature at $D_O = 5.66 \times 10^{-6}$ $cm^2 \cdot s^{-1}$ and $D_R = 6.89 \times 10^{-6}$ $cm^2 \cdot s^{-1}$ by running cyclic voltammetry at 5 mV/s.[40] Temperature was assumed to be 298 K to calculate the electroactive area of the working electrode as 0.0957 cm^2 for the oxidized species. The reduced species electroactive area was in agreement at 0.0846 cm^2. This is over 130% of the geometric area for the oxidized species, which is sensible given the rough surface observed in **Figure 3.2**. The electroactive area determined using the oxidized and reduced $Fc(MeOH)_2$ was 0.0776cm^2 (oxidized species) and 0.0685cm^2

(reduced species), which is roughly 110% of the geometric area for the oxidized species. These values were again calculated using the assumption of 298 K and diffusion constants of $D_R = 6.06\times 10^{-6}$ cm^2·s^{-1} and $D_o = 7.00 \times 10^{-6}$ cm^2·s^{-1} calculated in the same manner as for $Fe(CN)_6^{3-/4-}$ in agreement with previous work.[41] Due to the surface sensitive nature of $Fe(CN)_6^{3-/4-}$, it was expected for the geometric area in $Fe(CN)_6^{3-/4-}$ to be lower than that of $Fc(MeOH)_2$.[42] It is hypothesized that the difference in electroactive area between the two probes is the result of random variation in surface area of the TPEs.

After establishing the baselines for TPE behavior and surface characteristics, TPE surface functionalization was carried out by electroreduction of aryl diazonium salt produced in situ by reacting 4-(trimethylsilyl)ethynylaniline with sodium nitrite, forming a protected alkyl monolayer.[16, 27] Representative cyclic voltammograms (Appendix A, **Figure A.5**) demonstrate that the grafting reaction proceeded comparably to previous reports.[17, 18, 29] The resulting surface shows a clear silicon signal compared to a bare electrode (**Figure 3.3**) confirming, in conjunction with electrochemical data, a TMS-protected 4-ethynylbenzene monolayer on the surface. The C1s high resolution XPS spectrum also shows a broadening of the C1s peak including a contribution from C-Si and C-N bonding at 284.9 eV and 285.19 eV respectively, with atomic compositions calculated as follows: C-Si: 10.2%, C-C, C=C: 15.0%, C-N: 20.5%, C-O: 7.9% and C=O: 46.4%. The increase in C=O relative atomic percent is probably due to the aqueous treatment of the electrode surface during electrochemical grafting. The C-N contribution has already been observed during aryl diazonium grafting and is attributed to the reaction of the diazonium cation with surface groups of the carbon electrode or grafting of azophenyl groups, formed from the one-electron reduction of the diazo functional group, directly at the electrode surface.[43-45]

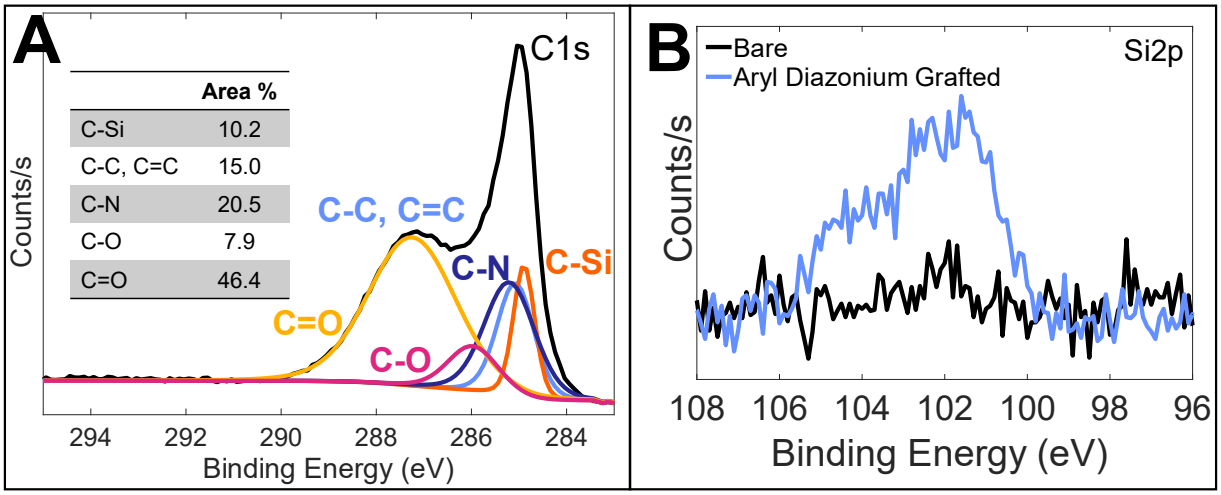

Figure 3.3. (A) C1s and **(B)** Si2p high resolution XPS spectra of functionalized TPE with 4-(trimethylsilyl)ethynylbenzene monolayer.

The diazonium salt solution concentration was varied from 0 mM to 10 mM (Appendix A, **Figure A.6**) and the resulting electrochemical behavior of the functionalized TPE was evaluated via cyclic voltammetry in solution containing $Fc(MeOH)_2$ or $Fe(CN)_6^{3-/4-}$ redox probes. **Figure 3.4** shows the representative CVs for $Fc(MeOH)_2$ and $Fe(CN)_6^{3-/4-}$ redox probes. The CVs obtained in $Fe(CN)_6^{3-/4-}$ confirm a complete coverage of the TPE surface, with no pinholes or defects, for aryl diazonium concentration as low as 0.5 mM, while in $Fc(MeOH)_2$ no significant change can be observed. This is indicative of a very thin layer deposition as observed previously.[16] At 0.05 mM (Appendix A, **Figure A.6**), there is a significant increase in reduction/oxidation of $Fe(CN)_6^{3-/4-}$ indicating a disperse monolayer. The 0.5 mM diazonium solution was used for the remainder of the work, reducing reagent cost (compared to 10 mM), but maintaining a consistent and complete functionalization of the surface.

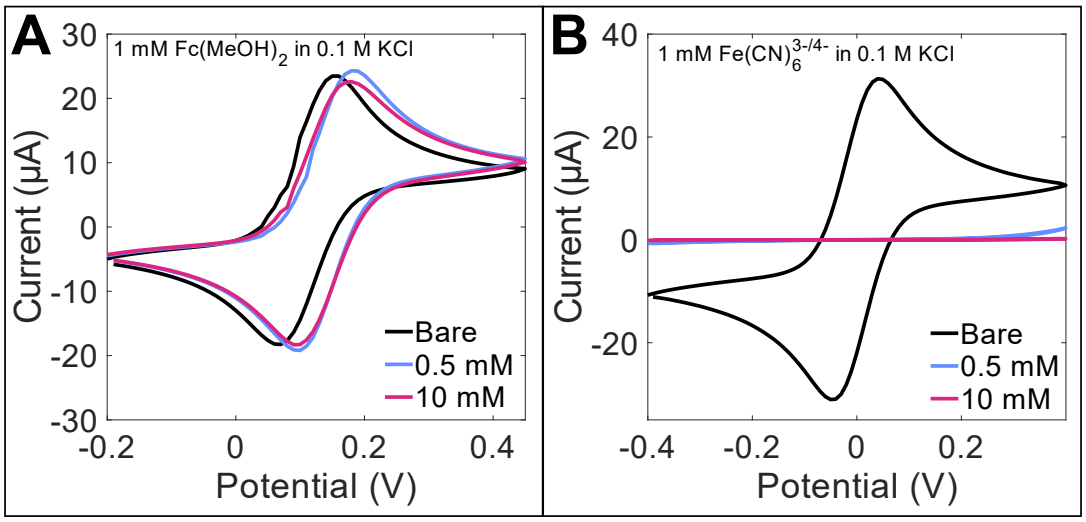

Figure 3.4. Representative cyclic voltammograms (**A)** 1 mM $Fc(MeOH)_2$ in 0.1 M KCl or (**B)** 1 mM $Fe(CN)_6^{3-/4-}$ in 0.1 M KCl on modified electrodes with 0.5 or 10 mM of diazonium salt solution grafted to the surface via electroreduction. Potential are given versus carbon pseudo reference.

From the voltammograms of $Fc(MeOH)_2$ (Appendix A, **Figure A.7A and A.7C**) we could derive an apparent electroactive area of the electrode before and after modification. The oxidized species electroactive area is 0.0708 cm^2 which is an 9% decrease from the bare surface area, which effectively does not impact the proportion of electroactive area percentage of the geometric area. The reduced species electroactive area is 0.0751 cm^2 which is an increase of approximately 10% from the bare surface and also not an appreciable change from the percent of the geometric area. The results indicate that the electrode modifications do not significantly impede the rate of electron transfer with ferrocene dimethanol, which is beneficial when considering biosensing applications.

Removing the TMS protecting group is the next phase and is critical for freeing the ethynyl group for click chemistry. While using TBAF in tetrahydrofuran has been shown to be highly successful, TPEs are not compatible with organic solvents.[17] Thus sodium

hydroxide was used to remove the protecting group.[46] Deprotection conditions were optimized (Appendix A, **Figure A.8**) and sonicating the electrodes in 1M NaOH for 20 min is effective in the removal of the TMS protection group. Cyclic voltammograms in **Figure 3.5** show that some $Fe(CN)_6^{3-/4-}$ signal is recovered after deprotection, while $Fc(MeOH)_2$ signal is largely unaffected. The signal suppression of $Fe(CN)_6^{3-/4-}$ despite deprotection is expected due to the small protecting group lending to a dense packing of the monolayer.[47]

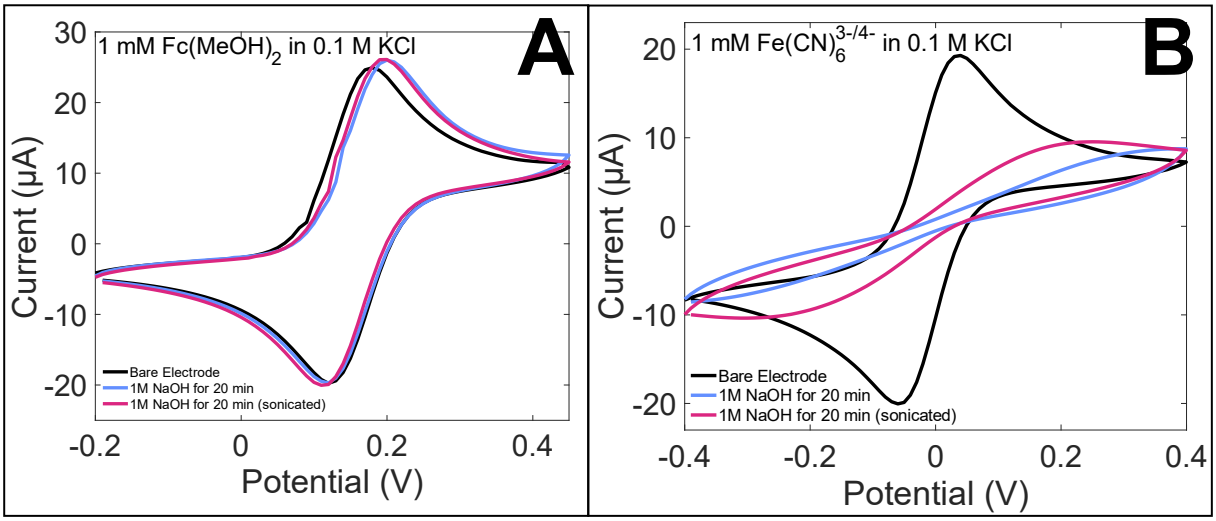

Figure 3.5. Representative cyclic voltammograms in **(A)** 1 mM $Fc(MeOH)_2$ in 0.1 M KCl or **(B)** 1 mM $Fe(CN)_6^{3-/4-}$ in 0.1 M KCl of bare (black curves) and functionalized TPEs deprotected using 1M NaOH solution for 20 min with (magenta curves) and without sonication (blue curves).

Upon freeing the alkyne moiety for the click chemistry reaction, a short diazido-PEG linker (N_3-PEG3-N_3) was introduced by click chemistry reaction, followed by the addition of ferrocenyl moieties through a second click chemistry reaction, resulting in a surface bound redox probe. The successful bonding of ferrocenyl moieties is observed both by electrochemical means (**Figure 3.6A**) and by the appearance of a new signal at 709.5 eV in the XPS survey spectrum attributed to Fe2p (**Figure 3.6B**). From the area

under the oxidation peak, the surface concentration of immobilized ferrocene (Γ_{Fc}) was determined.[48] At a scan rate of 10 mV·s^{-1}, the Γ_{Fc} was determined to be (1.0 ± 0.2) × 10^{-10} mol·cm^{-2}. This value is comparable to those reported for a similar approach on glassy carbon and pyrolytic graphite edge electrodes, (3.3 ± 0.9) × 10^{-10} and (14.3 ± 1.0) × 10^{-10} mol·cm^{-2} respectively.[48] This value is especially reasonable when considering the possible impact of the diazido-PEG linker used to immobilize the ferrocenyl moieties.

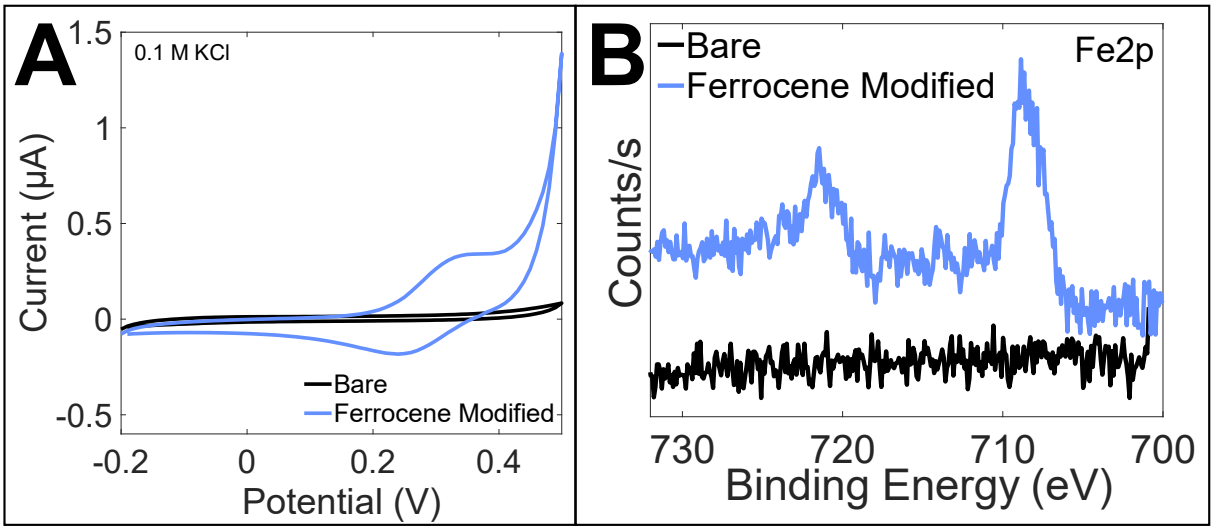

Figure 3.6. (**A**) Representative cyclic voltammograms of bare (black curve) and ferrocenyl functionalized (blue curve) TPE by click chemistry. Potential are given versus carbon pseudo-reference and scan rate = 10 mV·s^{-1}. (**B**) Fe2p high resolution XPS spectra of bare (black curve) and ferrocenyl functionalized (blue curve) TPE by click chemistry.

Upon demonstrating the success of clicking ferrocene to the surface, N_3-PEG3-biotin was clicked to the electrode surface, following diazonium electrografting. Representative CVs following the stepwise TPE modification (Appendix A, **Figure A.9**) show the decrease in electron transfer at the surface with $Fe(CN)_6^{3-/4-}$. The first step is from bare electrode to grafted and the near total suppression of electron transfer is seen. After deprotection, the signal is recovered and the subsequent step to click N_3-PEG3-

biotin to the surface causes the signal to decrease as expected. To evaluate the quantity of biotin that was clicked onto the surface, the apparent electroactive area was determined considering the oxidation of $Fc(MeOH)_2$ at different scan rates (Appendix A, **Figure A.10**) with **Eq 3.1** once again. In this estimation, we consider that the surface covered by PEG3-biotin is blocking for the oxidation of $Fc(MeOH)_2$. The oxidized species electroactive area was 0.0529 cm^2 which is a 27% decrease from that of the grafted electrode and 32% decrease from the bare electrode, thus the binding of the N_3-PEG3-biotin does not significantly impede electron transfer when using $Fc(MeOH)_2$.

Ultimately, the use of TPEs as an immunosensor requires the immobilization of a biorecognition element, such as an antibody to the surface. The confirmed presence of biotin clicked to the surface gave a point for streptavidin conjugation. Preliminary tests with cyclic voltammetry (Appendix A, **Figure A.9**) showed the suppression of oxidation and reduction of $Fe(CN)_6^{3-/4-}$ as expected. It is seen that the signal on a streptavidin modified electrode is significantly lower than the negative control (N_3-PEG3-biotin modified electrode incubated in PBS only). Surprisingly, when streptavidinated-IgG antibody was bound to the biotin clicked surface, the resulting voltammogram shows higher signal than any of the modification steps. This behavior was further investigated by electrochemical impedance spectroscopy (EIS) (**Figure 3.7**). As expected, the data mirrors the CV results. The charge transfer resistance, R_{ct}, was calculated by the equivalent circuit shown in **Figure 3.7B** which is based on modified electrode equivalent circuits for electrodes with surface modification.[49-52] The R_{ct} values represented by the bar chart in **Figure 3.7B** correspond to R3 in the equivalent circuit and the average percent error of the fit was less than 5% across all conditions (Appendix A, **Table A.1**). The R_{ct} increases upon the addition of streptavidin compared to the control of phosphate buffered

saline (PBS) yet decreases substantially when streptavidinated antibody is bound instead. Streptavidin is roughly 5 nm in diameter and is expected to pack much more tightly than the streptavidin-antibody complex in which the antibody portion alone is upwards of 14 nm at the longest side.[53, 54] Further, it is hypothesized that the streptavidin-antibody conjugate disrupts the PEG3-biotin monolayer on the surface creating gaps for the redox probe, $Fe(CN)_6^{3-/4-}$, to perform electron transfer more effectively at the electrode surface.

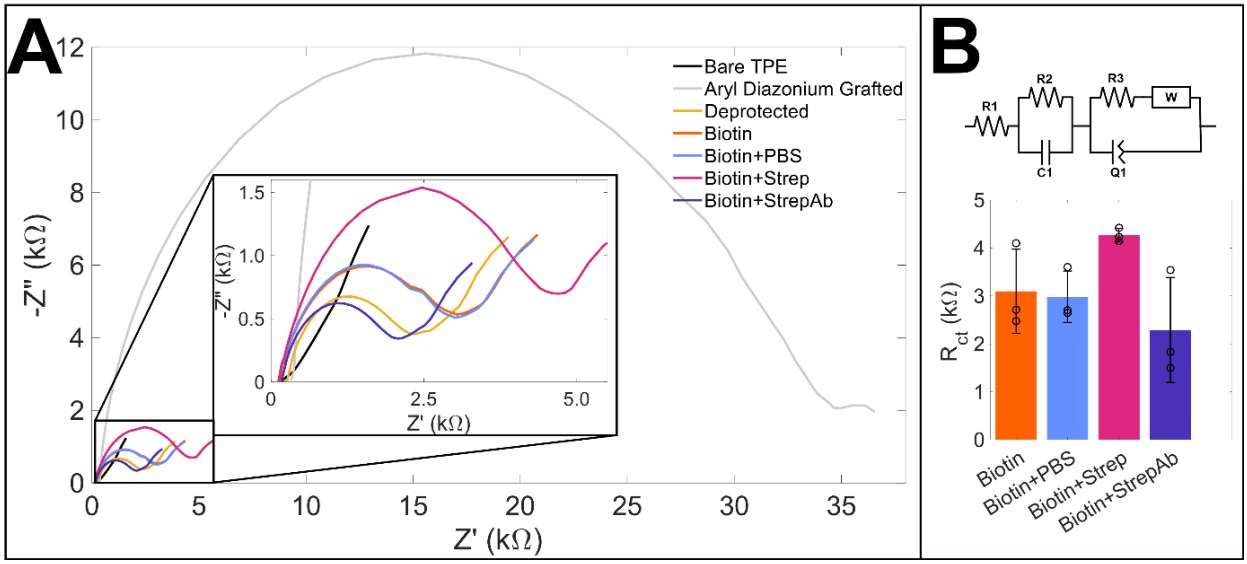

Figure 3.7. (A) Representative Nyquist plots demonstrating the change in R_{ct} as the surface groups change. **(B)** EIS equivalent circuit and resulting calculated R_{ct} values (n=3) where the error bars represent standard deviation.

Further support that demonstrates the successful conjugation of streptavidin to the surface was achieved via scanning electrochemical microscopy (SECM) using $Fe(CN)_6^{4-}$ as the redox probe (**Figure 3.8**). On the bare electrode, approach curves show positive feedback (**Figure 3.8A**) indicating electron transfer between the TPE surface and $Fe(CN)_6^{4-}$ in solution. The increase in current is relatively small, likely due to the rugosity of the surface impeding the approach of the SECM tip. A 200 µm square map of the bare electrode surface shows areas of higher and lower activity due to the surface

roughness, but the whole surface demonstrates positive feedback indicating that there are no insulating zones on the bare TPE surface. After modifying the TPE with N_3-PEG3-biotin, negative feedback is observed across the whole surface shown in **Figure 3.8B**, corresponding with full coverage of the electrode preventing electron transfer. Approach curves for both the bare and N_3-PEG3-biotin modified electrodes are consistent within groups regardless of the approach location. Streptavidin was bound to the N_3-PEG3-biotin modified surface and the resulting surface is shown to be highly heterogenous with some areas giving positive feedback and some giving negative (**Figure 3.8C**). However, when streptavidin-antibody is immobilized onto the TPE instead, the surface regains positive feedback across the surface. The culmination of the data further supports the hypothesis that binding the relatively large streptavidin-antibody complex creates disruptions in the modification layers to facilitate the electron transfer at the TPE surface. **Figure 3.9** illustrates the hypothesis on a molecular level where the bulkier streptavidin-antibody structure may cause greater gaps in the surface modifications allowing more $Fe(CN)_6^{3-/4-}$ to interact with the surface.

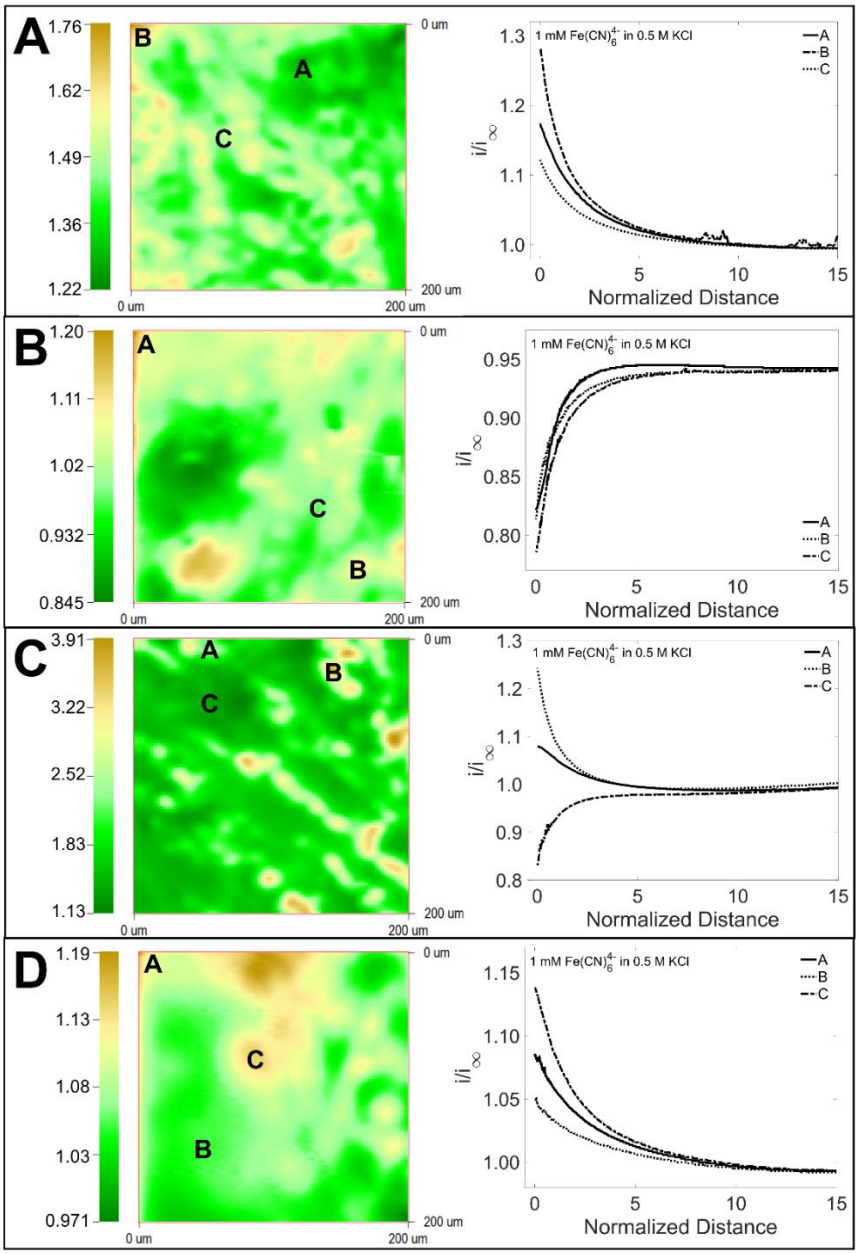

Figure 3.8. SECM maps and representative (n=3) probe approach curves taken in 1 mM ferrocyanide in 0.5 M KCl of 200 µm square sections of **(A)** bare electrodes, **(B)** N_3-PEG3-biotin modified electrodes, **(C)** streptavidin immobilized on electrodes, and **(D)** streptavidinated antibody immobilized on electrodes. Average currents for the maps are 1.18 ± 0.08 µA, 1.20 ± 0.05 µA, 1.46 ± 0.23 µA, and 1.21 ± 0.05 µA respectively, with no statistical difference. All reported currents are normalized against the infinite current.

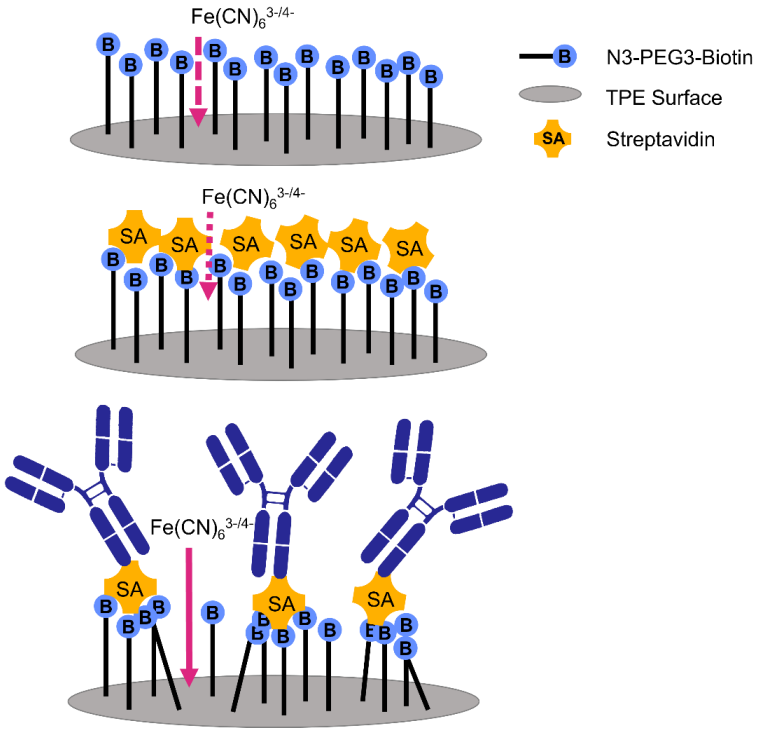

Figure 3.9. Hypothesized molecular-level behavior of modified TPEs with the binding of streptavidin (SA) and streptavidin-antibody to N_3-PEG3-biotin modified TPEs.

Confirmation of streptavidin-antibody bound to the surface was made via XPS (**Figure 3.10**) where the C1s high resolution spectra demonstrate the changes in surface chemistry. Both biotin and streptavidin-antibody modified TPEs show the presence of increased nitrogen and sulfur over the bare electrode as expected due to the formation of the triazole linkage with N_3-PEG3-biotin and protein composition.[55-57] Most XPS analysis penetrates 5-10 nm into the sample surface; hence, the relative reduction in C-S and C-N bonding in the streptavidin-antibody decorated surface over the biotin clicked surface indicates the biotin structure being hidden by the comparatively large protein layer.[57-59] The XPS data supports the electrochemical data demonstrating that streptavidin-antibody is successfully bound to TPEs modified with N_3-PEG3-biotin via click chemistry following diazonium electrografting for immunosensing applications.

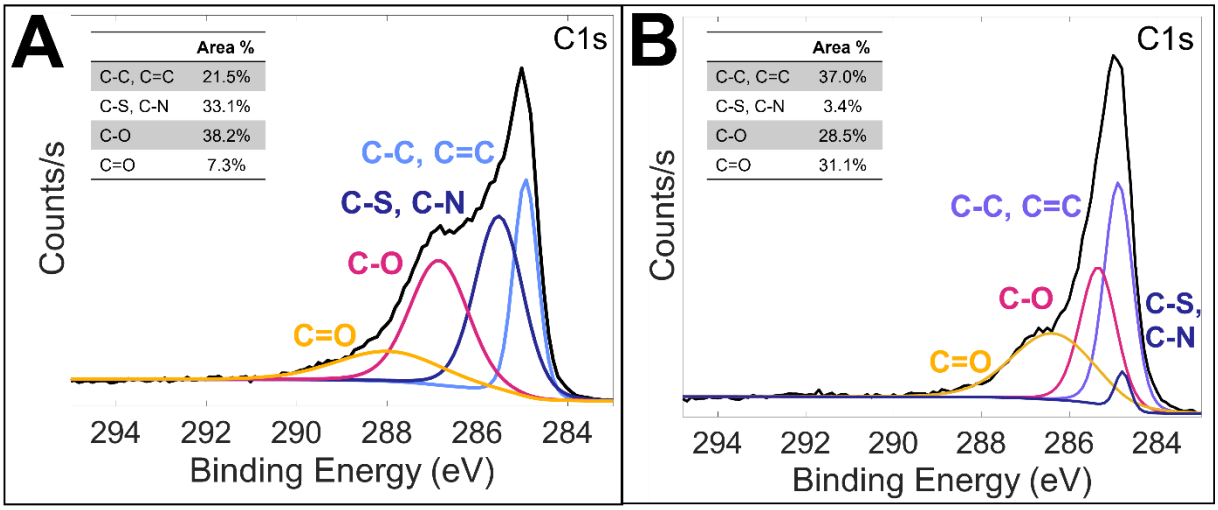

Figure 3.10. Deconvoluted XPS C1s high resolution spectra for **(A)** N_3-PEG3-biotin clicked and **(B)** streptavidin-antibody modified electrodes.

3.5 Conclusion

Here it has been shown that diazonium grafting followed by click chemistry is successful for adding biotin functionalization to TPEs, creating an easily customizable platform for biosensing. Electrochemical techniques and XPS were used to determine surface coverage of the diazonium monolayer, clicked N_3-PEG3-biotin, and to validate each step of the modification procedure. We demonstrated that the modification is successful and binding of large complexes, such as streptavidin-antibody conjugation, is believed to disrupt the modification layer, increasing the observed current in a surface sensitive redox probe. The multi-step approach used herein allows for a uniform monolayer to form in the aryl diazonium grafting step followed by highly customizable functionalization via click chemistry for a stable, biotinylated TPE. This work provides an exciting basis for expanding the applicability of TPEs, which can be a better choice of electrode compared to expensive metal electrodes and more robust than SPCEs.

References

1. Martinez, B.; Leroux, Y. R.; Hapiot, P.; Henry, C. S., Surface Modification of Thermoplastic Electrodes for Biosensing Applications via Copper-Catalyzed Click Chemistry. *ACS Applied Materials & Interfaces* **2023**.

2. Klunder, K. J.; Nilsson, Z.; Sambur, J. B.; Henry, C. S., Patternable Solvent-Processed Thermoplastic Graphite Electrodes. *Journal of the American Chemical Society* **2017,** *139* (36), 12623-12631.

3. Ozer, T.; Henry, C. S., All-solid-state potassium-selective sensor based on carbon black modified thermoplastic electrode. *Electrochimica Acta* **2022,** *404*, 139762.

4. Noviana, E.; Klunder, K. J.; Channon, R. B.; Henry, C. S., Thermoplastic Electrode Arrays in Electrochemical Paper-Based Analytical Devices. *Analytical Chemistry* **2019,** *91* (3), 2431-2438.

5. McCord, C. P.; Summers, B.; Henry, C. S., Simultaneous Analysis of Ascorbic Acid, Uric Acid, and Dopamine at Bare Polystyrene Thermoplastic Electrodes. *ChemElectroChem* **2022,** *9* (11), e202101600.

6. Ozer, T.; McCord, C.; Geiss, B. J.; Dandy, D.; Henry, C. S., Thermoplastic Electrodes for Detection of Escherichia coli. *Journal of The Electrochemical Society* **2021,** *168* (4), 047509.

7. Clark, K. M.; Henry, C. S., Thermoplastic Electrode (TPE)-based Enzymatic Glucose Sensor Using Polycaprolactone-graphite Composites. *Electroanalysis* **2021,** *n/a* (n/a).

8. Danczyk, R.; Krieder, B.; North, A.; Webster, T.; HogenEsch, H.; Rundell, A., Comparison of antibody functionality using different immobilization methods. *Biotechnology and Bioengineering* **2003,** *84* (2), 215-223.

9. Stanković, V.; Đurđić, S.; Ognjanović, M.; Antić, B.; Kalcher, K.; Mutić, J.; Stanković, D. M., Anti-human albumin monoclonal antibody immobilized on EDC-NHS functionalized carboxylic graphene/AuNPs composite as promising electrochemical HSA immunosensor. *Journal of Electroanalytical Chemistry* **2020,** *860*, 113928.

10. Sharafeldin, M.; McCaffrey, K.; Rusling, J. F., Influence of antibody immobilization strategy on carbon electrode immunoarrays. *Analyst* **2019,** *144* (17), 5108-5116.

11. Sehgal, D.; Vijay, I. K., A method for the high efficiency of water-soluble carbodiimide-mediated amidation. *Anal Biochem* **1994,** *218* (1), 87-91.

12. Nakajima, N.; Ikada, Y., Mechanism of Amide Formation by Carbodiimide for Bioconjugation in Aqueous Media. *Bioconjugate Chemistry* **1995,** *6* (1), 123-130.

13. Yáñez-Sedeño, P.; González-Cortés, A.; Campuzano, S.; Pingarrón, J. M., Copper(I)-Catalyzed Click Chemistry as a Tool for the Functionalization of Nanomaterials and the Preparation of Electrochemical (Bio)Sensors. *Sensors (Basel)* **2019,** *19* (10).

14. Guerrero, S.; Cadano, D.; Agüí, L.; Barderas, R.; Campuzano, S.; Yáñez-Sedeño, P.; Pingarrón, J. M., Click chemistry-assisted antibodies immobilization for immunosensing of CXCL7 chemokine in serum. *Journal of Electroanalytical Chemistry* **2019,** *837*, 246-253.

15. Cesbron, M.; Levillain, E.; Breton, T.; Gautier, C., Click Chemistry: A Versatile Method for Tuning the Composition of Mixed Organic Layers Obtained by Reduction of Diazonium Cations. *ACS Applied Materials & Interfaces* **2018,** *10* (44), 37779-37782.

16. Leroux, Y. R.; Fei, H.; Noël, J.-M.; Roux, C.; Hapiot, P., Efficient Covalent Modification of a Carbon Surface: Use of a Silyl Protecting Group To Form an Active Monolayer. *Journal of the American Chemical Society* **2010,** *132* (40), 14039-14041.

17. Leroux, Y. R.; Hui, F.; Noël, J.-M.; Roux, C.; Downard, A. J.; Hapiot, P., Design of Robust Binary Film onto Carbon Surface Using Diazonium Electrochemistry. *Langmuir* **2011,** *27* (17), 11222-11228.

18. Pinson, J.; Podvorica, F., Attachment of organic layers to conductive or semiconductive surfaces by reduction of diazonium salts. *Chemical Society Reviews* **2005,** *34* (5), 429-439.

19. Qi, H.; Li, M.; Zhang, R.; Dong, M.; Ling, C., Double electrochemical covalent coupling method based on click chemistry and diazonium chemistry for the fabrication of sensitive amperometric immunosensor. *Analytica Chimica Acta* **2013,** *792*, 28-34.

20. Guerrero, S.; Agüí, L.; Yáñez-Sedeño, P.; Pingarrón, J. M., Design of electrochemical immunosensors using electro-click chemistry. Application to the detection of IL-1β cytokine in saliva. *Bioelectrochemistry* **2020,** *133*, 107484.

21. An, Y.; Jin, T.; Zhu, Y.; Zhang, F.; He, P., An ultrasensitive electrochemical aptasensor for the determination of tumor exosomes based on click chemistry. *Biosensors and Bioelectronics* **2019,** *142*, 111503.

22. Xie, D.; Li, C.; Shangguan, L.; Qi, H.; Xue, D.; Gao, Q.; Zhang, C., Click chemistry-assisted self-assembly of DNA aptamer on gold nanoparticles-modified screen-printed carbon electrodes for label-free electrochemical aptasensor. *Sensors and Actuators B: Chemical* **2014,** *192*, 558-564.

23. Mishyn, V.; Rodrigues, T.; Leroux, Y. R.; Aspermair, P.; Happy, H.; Bintinger, J.; Kleber, C.; Boukherroub, R.; Knoll, W.; Szunerits, S., Controlled covalent functionalization of a graphene-channel of a field effect transistor as an ideal platform for (bio)sensing applications. *Nanoscale Horizons* **2021,** *6* (10), 819-829.

24. Rodrigues, T.; Mishyn, V.; Leroux, Y. R.; Butruille, L.; Woitrain, E.; Barras, A.; Aspermair, P.; Happy, H.; Kleber, C.; Boukherroub, R.; Montaigne, D.; Knoll, W.; Szunerits, S., Highly performing graphene-based field effect transistor for the differentiation between mild-moderate-severe myocardial injury. *Nano Today* **2022,** *43*, 101391.

25. Sánchez-Tirado, E.; González-Cortés, A.; Yáñez-Sedeño, P.; Pingarrón, J. M., Carbon nanotubes functionalized by click chemistry as scaffolds for the preparation of electrochemical immunosensors. Application to the determination of TGF-beta 1 cytokine. *Analyst* **2016,** *141* (20), 5730-5737.

26. Flavel, B. S.; Gross, A. J.; Garrett, D. J.; Nock, V.; Downard, A. J., A Simple Approach to Patterned Protein Immobilization on Silicon via Electrografting from Diazonium Salt Solutions. *ACS Applied Materials & Interfaces* **2010,** *2* (4), 1184-1190.

27. Hapiot, P.; Lagrost, C.; Leroux, Y. R., Molecular nano-structuration of carbon surfaces through reductive diazonium salts grafting. *Current Opinion in Electrochemistry* **2018,** *7*, 103-108.

28. Wu, T.; Fitchett, C. M.; Brooksby, P. A.; Downard, A. J., Building Tailored Interfaces through Covalent Coupling Reactions at Layers Grafted from Aryldiazonium Salts. *ACS Applied Materials & Interfaces* **2021,** *13* (10), 11545-11570.

29. Berg, K. E.; Leroux, Y. R.; Hapiot, P.; Henry, C. S., Increasing Applications of Graphite Thermoplastic Electrodes with Aryl Diazonium Grafting. *ChemElectroChem* **2019,** *6* (18), 4811-4816.

30. Hayat, A.; Sassolas, A.; Marty, J.-L.; Radi, A.-E., Highly sensitive ochratoxin A impedimetric aptasensor based on the immobilization of azido-aptamer onto electrografted binary film via click chemistry. *Talanta* **2013,** *103*, 14-19.

31. Hein, C. D.; Liu, X. M.; Wang, D., Click chemistry, a powerful tool for pharmaceutical sciences. *Pharm Res* **2008,** *25* (10), 2216-30.

32. Obaje, E. A.; Cummins, G.; Schulze, H.; Mahmood, S.; Desmulliez, M. P. Y.; Bachmann, T. T., Carbon screen-printed electrodes on ceramic substrates for label-free molecular detection of antibiotic resistance. *Journal of Interdisciplinary Nanomedicine* **2016,** *1* (3), 93-109.

33. Velický, M.; Toth, P. S.; Woods, C. R.; Novoselov, K. S.; Dryfe, R. A. W., Electrochemistry of the Basal Plane versus Edge Plane of Graphite Revisited. *The Journal of Physical Chemistry C* **2019,** *123* (18), 11677-11685.

34. Ba, O. M.; Marmey, P.; Anselme, K.; Duncan, A. C.; Ponche, A., Surface composition XPS analysis of a plasma treated polystyrene: Evolution over long storage periods. *Colloids and Surfaces B: Biointerfaces* **2016,** *145*, 1-7.

35. Hontoria-Lucas, C.; López-Peinado, A. J.; López-González, J. d. D.; Rojas-Cervantes, M. L.; Martín-Aranda, R. M., Study of oxygen-containing groups in a series of graphite oxides: Physical and chemical characterization. *Carbon* **1995,** *33* (11), 1585-1592.

36. Blyth, R. I. R.; Buqa, H.; Netzer, F. P.; Ramsey, M. G.; Besenhard, J. O.; Golob, P.; Winter, M., XPS studies of graphite electrode materials for lithium ion batteries. *Applied Surface Science* **2000,** *167* (1), 99-106.

37. Browne, M. M.; Lubarsky, G. V.; Davidson, M. R.; Bradley, R. H., Protein adsorption onto polystyrene surfaces studied by XPS and AFM. *Surface Science* **2004,** *553* (1), 155-167.

38. Hamann, C. H.; Hammett, A.; Vielstich, W., *Electrochemistry*. Second ed.; Wiley-VCH: 2007.

39. Chen, P.; McCreery, R. L., Control of Electron Transfer Kinetics at Glassy Carbon Electrodes by Specific Surface Modification. *Analytical Chemistry* **1996,** *68* (22), 3958-3965.

40. Moldenhauer, J.; Meier, M.; Paul, D. W., Rapid and Direct Determination of Diffusion Coefficients Using Microelectrode Arrays. *Journal of The Electrochemical Society* **2016,** *163* (8), H672-H678.

41. Mampallil, D.; Mathwig, K.; Kang, S.; Lemay, S. G., Redox Couples with Unequal Diffusion Coefficients: Effect on Redox Cycling. *Analytical Chemistry* **2013,** *85* (12), 6053-6058.

42. McCreery, R. L.; McDermott, M. T., Comment on Electrochemical Kinetics at Ordered Graphite Electrodes. *Analytical Chemistry* **2012,** *84* (5), 2602-2605.

43. Saby, C.; Ortiz, B.; Champagne, G. Y.; Bélanger, D., Electrochemical Modification of Glassy Carbon Electrode Using Aromatic Diazonium Salts. 1. Blocking Effect of 4-Nitrophenyl and 4-Carboxyphenyl Groups. *Langmuir* **1997,** *13* (25), 6805-6813.

44. Combellas, C.; Kanoufi, F.; Pinson, J.; Podvorica, F. I., Time-of-Flight Secondary Ion Mass Spectroscopy Characterization of the Covalent Bonding between a Carbon Surface and Aryl Groups. *Langmuir* **2005,** *21* (1), 280-286.

45. Laforgue, A.; Addou, T.; Bélanger, D., Characterization of the Deposition of Organic Molecules at the Surface of Gold by the Electrochemical Reduction of Aryldiazonium Cations. *Langmuir* **2005,** *21* (15), 6855-6865.

46. Wuts, P. G. M., Protection for the Alkyne-CH. In *Greene's Protective Groups in Organic Synthesis*, 5th ed.; John Wiley & Sons Inc.: Hoboken, New Jersey, 2014.

47. Leroux, Y. R.; Hapiot, P., Nanostructured Monolayers on Carbon Substrates Prepared by Electrografting of Protected Aryldiazonium Salts. *Chemistry of Materials* **2013,** *25* (3), 489-495.

48. Evrard, D.; Lambert, F.; Policar, C.; Balland, V.; Limoges, B., Electrochemical Functionalization of Carbon Surfaces by Aromatic Azide or Alkyne Molecules: A Versatile Platform for Click Chemistry. *Chemistry – A European Journal* **2008,** *14* (30), 9286-9291.

49. Magar, H. S.; Hassan, R. Y. A.; Mulchandani, A., Electrochemical Impedance Spectroscopy (EIS): Principles, Construction, and Biosensing Applications. *Sensors (Basel)* **2021,** *21* (19).

50. Najlaoui, D.; Echabaane, M.; Ben Khélifa, A.; Rouis, A.; Ben Ouada, H., Photoelectrochemical impedance spectroscopy sensor for cloxacillin based on tetrabutylammonium octamolybdate. *Journal of Solid State Electrochemistry* **2019,** *23* (12), 3329-3341.

51. Russell, C.; Ward, A. C.; Vezza, V.; Hoskisson, P.; Alcorn, D.; Steenson, D. P.; Corrigan, D. K., Development of a needle shaped microelectrode for electrochemical detection of the sepsis biomarker interleukin-6 (IL-6) in real time. *Biosensors and Bioelectronics* **2019,** *126*, 806-814.

52. Wang, B.; Jing, R.; Qi, H.; Gao, Q.; Zhang, C., Label-free electrochemical impedance peptide-based biosensor for the detection of cardiac troponin I incorporating gold nanoparticles modified carbon electrode. *Journal of Electroanalytical Chemistry* **2016,** *781*, 212-217.

53. Kuzuya, A.; Numajiri, K.; Kimura, M.; Komiyama, M., Single-molecule accommodation of streptavidin in nanometer-scale wells formed in DNA nanostructures. *Nucleic Acids Symp Ser (Oxf)* **2008,** (52), 681-2.

54. Tan, Y. H.; Liu, M.; Nolting, B.; Go, J. G.; Gervay-Hague, J.; Liu, G. Y., A nanoengineering approach for investigation and regulation of protein immobilization. *ACS Nano* **2008,** *2* (11), 2374-84.

55. Holzer, B.; Manoli, K.; Ditaranto, N.; Macchia, E.; Tiwari, A.; Di Franco, C.; Scamarcio, G.; Palazzo, G.; Torsi, L., Characterization of Covalently Bound Anti-Human Immunoglobulins on Self-Assembled Monolayer Modified Gold Electrodes. *Advanced Biosystems* **2017,** *1* (11), 1700055.

56. Mwanza, D.; Phal, S.; Nyokong, T.; Tesfalidet, S.; Mashazi, P., Electrografting of isophthalic acid monolayer and covalent attachment of antibody onto carbon surfaces: Construction of capacitive biosensor for methotrexate detection. *Electrochimica Acta* **2021,** *398*, 139360.

57. Nimni, M. E.; Han, B.; Cordoba, F., Are we getting enough sulfur in our diet? *Nutrition & Metabolism* **2007,** *4* (1), 24.

58. Gruian, C.; Vanea, E.; Simon, S.; Simon, V., FTIR and XPS studies of protein adsorption onto functionalized bioactive glass. *Biochimica et Biophysica Acta (BBA) - Proteins and Proteomics* **2012,** *1824* (7), 873-881.

59. Watts, J. F.; Wolstenholme, J., *An Introduction to Surface Analysis by XPS and AES*. Wiley: 2019.

CHAPTER 4 - Characterization of Heterogeneous Polyethylene Glycol Monolayers with Surface-Bound Ferrocene on Thermoplastic Electrodes for Label-Free Immunosensing Applications

4.1 Overview

The work presented in this chapter is an expansion of the platform developed in Chapter 3. Enhancing signal of a label-free immunosensing platform has major implications on the sensitivity and accuracy of the electrochemical sensor. This is particularly important for the creation of immunosensors to effectively detect a target with low limits of detection. To address this need we demonstrate a signal enhancing platform on thermoplastic electrodes (TPEs) that utilizes a multifunctional monolayer with surface-bound ferrocene to aid electron transfer. The monolayer is created by using a mixture of differing polyethylene glycol (PEG) lengths with either an azide terminal group to attach the ferrocene or a biotin terminal group to allow for an antibody to be immobilized for immunosensing capabilities. Electrochemical impedance spectroscopy (EIS) and X-ray photoelectron spectroscopy (XPS) were used to characterize the monolayer formation and confirmed modifications. Proof-of-concept detection of SARS-CoV-2 nucleocapsid protein was achieved with limits of detection below 10 PFU/mL of inactivated virus in PBS.

The data collected in this work was in collaboration with Dr. Yann R. Leroux and Dr. Philipe Hapiot of the University of Rennes. XPS was done at the Colorado State University Analytical Resources Core (RRID: SCR_021758). Emie Marin assisted with data collection as well as with writing initial drafts of this work for submission for publication. The findings are in preparation, but not yet submitted for publication. Supporting information can be found in Appendix B.

4.2 Introduction

Recent years have brought a push towards more readily available point-of-care diagnostic tools for infectious diseases.[1] Electrochemical immunosensors have emerged as a promising technology in this regard, offering several advantages over other traditional diagnostic methods. Enzyme-linked immunosorbent assays (ELISAs) are widely used in clinical laboratories but can be time-consuming and may require specialized equipment and trained personnel.[2] Lateral flow assays (LFAs) are inexpensive and easy to use but suffer from low sensitivity and are limited to qualitative or semi-quantitative results.[3, 4] Shifting to electrochemical immunosensors fills the gap by remaining relatively inexpensive, sensitive, quantitative, and deployable at the point-of-care.[5]

Label-free electrochemical immunosensors are particularly attractive because they eliminate the need for labeling molecules, such as enzymes or fluorescent tags.[6, 7] This simplifies the assay, reduces costs, and minimizes the potential for interference, resulting in more straightforward and cost-effective diagnostic tools. Label-free electrochemical immunosensors are attractive due to their simplicity over labeled formats and have achieved very low limits of detection (LOD).[7-10] Various sensing mechanisms can be employed in immunosensors, but in the case of affinity-based immunosensors, it is typical for the sensor to exhibit a decrease in signal correlating to an increase of target antigen bound to the surface.[6, 11] This characteristic represents a constraint for label-free electrochemical immunosensors owing to the practical challenges associated with effectively blocking the electrode.

Enhancing the signal or the performance of the electrode within the surface modification is the approach of many researchers.[12] Gold is a common material used to

enhance the performance of carbon electrodes while providing convenient antibody immobilization sites.[13-15] A group recently published a label-free impedimetric immunosensor that achieved an LOD of 6 pg/mL for detecting SARS-CoV-2 nucleocapsid protein (N protein) in diluted saliva samples.[16] However, this sensor relied on using gold nanostructures electrodeposited onto screen printed carbon electrodes (SPCEs) followed by a number of modification steps including EDC/NHS crosslinking which can be prone to side reactions.[16, 17] A preferred approach is to use multifunctional modifications with to eliminate the total steps required and eliminate potentially poor crosslinking reactions.

One example is that of Liu and Gooding, in which their modification of molecular wires interspersed in a PEG monolayer on glassy carbon electrodes both blocked nonspecific adsorption and enhanced electron transfer between the target analytes and the electrode surface.[18] In the work described here we use click chemistry for the modification of thermoplastic electrodes (TPEs) with multifunctional monolayers composed of PEG chains terminated with either ferrocene or biotin for facile antibody immobilization, signal rectification, and blocking of nonspecific adsorption.

4.3 Materials and Methods

Electrode Fabrication and Surface Modification

Thermoplastic electrodes (TPEs) were fabricated according to previous methods using TC303 graphite (Asbury Graphite Mills Inc., NJ) and 45,000 MW polystyrene (Sigma-Aldrich, St. Louis, MO) in templates laser-cut into poly(methyl)methacrylate.[19, 20] Prior to use, each TPE was polished by wet sanding for 30 s sequentially on 150 and 600 grit silicon carbide sandpaper, then sonicated in ultrapure water for 5 min. Aryl diazonium grafting was performed as in previous work.[21] Briefly, 10 mM 4-

(trimethylsilyl)ethynylbenzene diazonium salt was produced in situ from reacting 4-(trimethylsilyl)-ethynylaniline (96%, Sigma-Aldrich, St. Louis, MO) with 2 molar equivalents of sodium nitrite (99.99% metals basis, Sigma-Aldrich, St. Louis, MO) in 0.1 M HCl (ACS certified, Fisher Scientific, Waltham, MA). The reaction solution was diluted to approximately 0.5 mM diazonium salt which was grafted to the working electrode via CV with potential swept from 0 to −0.8 V at 50 mV/s for five cycles. Electrodes were stored in a cool dry location and protected from dust before use.

The terminal alkyne was deprotected by sonicating the TPEs in 1 M NaOH (Fisher Scientific, Waltham, MA) for 20 minutes followed by rinsing in ultrapure water and air drying according to previous work.[21] The first click reaction was performed by adding 20 μL droplets of 20 mM $CuSO_4$ (pentahydrate, 99%, Sigma-Aldrich, St. Louis, MO), 5 mM ascorbic acid (Biogems International, Westlake Village, CA), and N_3-PEGn-biotin mixture. The azido-PEG mixture was composed of 10 mM of N_3-PEG11-biotin (Acrotein ChemBio, Hoover, AL), or 10 mM N_3-PEG24-biotin (Santa Cruz Biotechnology, Dallas, TX), made in 10 mM N_3-PEG3-N_3 (Toronto Research Chemicals, North York, ON, Canada). This 1:1 molar ratio of azido-PEG compounds was used unless otherwise specified. After reacting for 1 hr at room temperature, the electrodes were rinsed thoroughly with saturated EDTA (pH = 8, Sigma-Aldrich, St. Louis, MO) and ultrapure water. The second click reaction was completed next with 20 μL each of 20 mM $CuSO_4$, 5 mM ascorbic acid, and 10 mM ethynyl ferrocene (Ambeed, Arlington Heights, IL) in ethanol (reagent alcohol, Sigma-Aldrich, St. Louis, MO). Wells made of double-sided adhesive were applied to the TPEs to contain the reactants over the working electrode. The reaction was carried out at room temperature for 1 hr on a gentle shaker. Modified TPEs were thoroughly rinsed with EDTA and ultrapure water before subsequent use.

Figure 4.1 illustrates the surface modification with dual PEG spacer lengths terminated with biotin and ferrocene moieties.

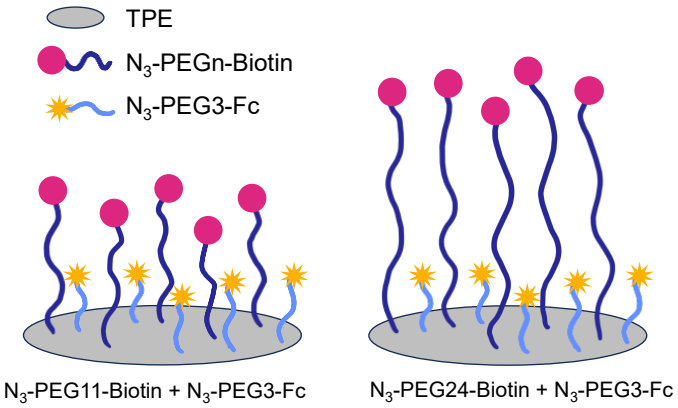

Figure 4.1. Molecular level diagram (not to scale) of the TPE surface modifications with heterogeneous monolayer formation.

Biosensor Fabrication and Testing

Streptavidin-conjugated antibody (strep-Ab) was prepared using a Lightning Link Kit (Abcam, Cambridge, UK) to link streptavidin to anti-SARS-CoV/SARS-CoV-2 nucleocapsid protein mouse monoclonal antibody (40143-MM05, Sino Biological, Wayne, PA). Stock strep-Ab was diluted 100-fold in phosphate buffered saline (PBS, pH = 7.4, Sigma-Aldrich, St. Louis, MO) to approximately 5 µg/mL and 20 µL was added to prepared TPEs for 1 hr at room temperature. After incubation, electrodes were rinsed thoroughly.

For nonspecific adsorption studies, a 20 µL of 5% of bovine serum albumin (BSA, Equitech-Bio, Kerrville, TX) in PBS was added to the modified TPE for 1 hr at room temperature. No strep-Ab was added to these electrodes. The N_3-PEG3-Fc control group was prepared similarly to the other electrodes, except there was no N_3-PEGn-biotin added

to the reaction mixture. After incubation in BSA, electrodes were rinsed thoroughly with PBS prior to electrochemical measurements.

For SARS-CoV-2 nucleocapsid protein (N protein) detection, TPEs modified through the strep-Ab step were incubated with 1% BSA to as a blocker for nonspecific adsorption. Inactivated SARS-CoV-2 virus samples were prepared according to previous methods.[22] Experiments with inactivated virus were performed following BSL2 safety protocols. Concentration of the stock solution in plaque forming units (PFU/mL) was determined by plaque assay.[23] Stock virus solution was diluted to 10 PFU/mL, 500 PFU/mL, and 2000 PFU/mL in PBS with 0.1% TWEEN20 (Sigma-Aldrich, St. Louis, MO) and 0.1% IGEPAL CA-630 (Sigma-Aldrich, St. Louis, MO). Prepared TPEs were exposed to 20 μL of virus solution for 30 min before rinsing thoroughly with PBS and measurement with SWV.

Electrochemical Measurements

All electrochemical measurements were completed using Palmsens4 potentiostat (Palmsens, Houten, Netherlands) and data was processed, fit, and plotted using PSTrace v.5. and MATLAB. Cyclic voltammetry (CV) and square wave voltammetry (SWV) were performed using 1 mM potassium ferricyanide ($Fe(CN)_6^{3-}$, Sigma-Aldrich, St. Louis, MO) in 0.1 M KCl (99.0%, Sigma-Aldrich, St. Louis, MO). The working and counter electrodes were TPEs (3 mm and 4.5 mm respectively), and the reference electrode was a saturated calomel electrode (SCE). CVs were collected by scanning from 0.65 V to -0.3 V at 20 mV/s with a 2 s equilibration time. Scan rate studies included 5, 20, 60, 100, 300, and 500 mV/s taken in random order. SWV measurements were done by scanning from 0.5 V to -0.1 V

with 0.002 V step, 0.05 V amplitude, and 10.0 Hz frequency after a 2 s equilibration time. The resulting voltammograms were baseline subtracted using moving average baseline.

Electrochemical impedance spectroscopy (EIS) was performed using a TPE pseudo-reference electrode according to previous work with some alterations.[21] The redox probe used was 1 mM ferri/ferrocyanide (0.5 mM potassium hexacyanoferrate trihydrate and 0.5 mM potassium ferricyanide) in 0.1 M KCl. Fixed scan was used with AC potential of 0.2 V, equilibration time of 3 s, and frequency range of 0.015 Hz to 10^5 Hz with 9.2 points per frequency decade.

Surface Composition Measurements

X-ray photoelectron spectroscopy (XPS) was performed on a Physical Electronics X-ray Photoelectron Spectrometer with a monochromated Al anode producing Al Kα X-rays and 2.0 × 0.8 mm aperture and 20 μA electron neutralizer. Survey spectra were collected for 10 min from 10 to 1100 eV. High-resolution spectra for C1s (not shown), O1s (not shown), N1s (not shown), and Fe2p (available in SI) were collected until a signal-to-noise ratio of 200 (for C1s) or 400 was reached or until 45 min collection time elapsed. The resulting spectra were processed and analyzed via CasaXPS software.

4.4 Results and Discussion

Initial testing was conducted to determine the electrochemical behavior of the mixed layers with and without the ferrocene functionality bound to the surface via N_3-PEG3-N_3. **Figure 4.2** shows the representative cyclic voltammograms at 20 mV/s scan rate in either 1 mM ferricyanide in 0.1 M KCl or background electrolyte (0.1 M KCl). Notably, the signal is approximately 4x and 2x higher when ethynyl ferrocene is bound to

the surface as N_3-PEG3-Fc in N_3-PEG11-biotin and N_3-PEG24-biotin mixed layers, respectively. This is comparable to more complex demonstrations of ferrocene-based signal enhancement in immunosensors.[24, 25] The peak current remains lower than the bare electrode in ferricyanide due to the presence of the modification layer. It was confirmed that the majority of the signal seen was indeed from aiding ferricyanide electron transfer rather than from the surface bound ferrocene, as very little signal on ferrocene modified TPEs in background electrolyte solution is seen. Signal rectification is also suspected due to the non-reversibility of the iron compounds after electrode modification.[26] Further, the length PEG spacer does not appear to impact the average peak current as they are not statistically unique (p-value = 0.942). At approximately 0.3 nm per monomer, N3-PEG3-N3 is approximately 0.9 nm, ignoring the additional length of the terminal azides.[27, 28] The lengths of N3-PEG11-biotin and N3-PEG24-biotin are approximately 3.3 nm and 7.2 nm, respectively, again, ignoring the terminal groups of azide and biotin.

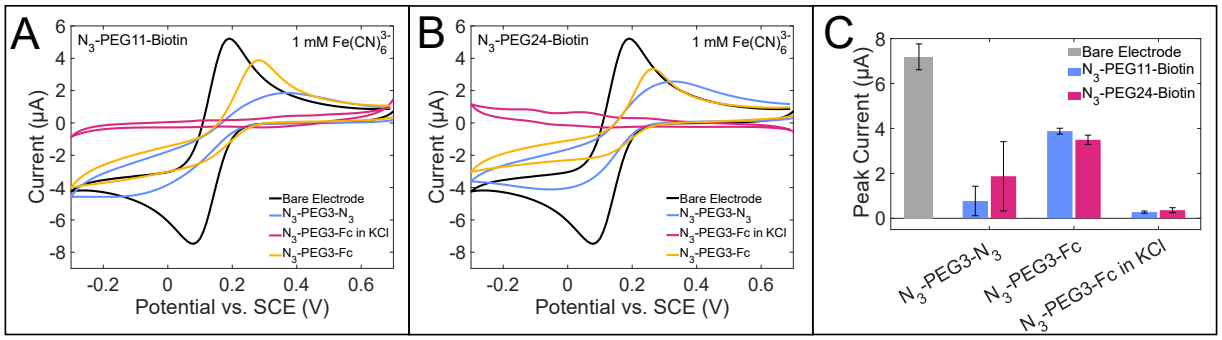

Figure 4.2. Representative CVs (versus SCE) in 1 mM $Fe(CN)_6^{3-}$ in 0.1 M KCl with and without ferrocene bound to the surface with a **(A)** N_3-PEG11-biotin or **(B)** N_3-PEG24-biotin mixed layer. **(C)** Average peak currents (n=3) show a clear increase in signal and consistency when ferrocene is surface bound within the modification layer.

Surface composition was verified with XPS to confirm the presence of ferrocene and compare relative amounts of ferrocene between monolayers with both lengths of N_3-PEGn-biotin. The survey spectra (Appendix B, **Figure B.1** and **B.2**) were used to calculate the relative abundance of iron with respect to carbon (I_{Fe}/I_C) shown in **Figure 4.3**. Fe2p high resolution XPS spectra are also available in Appendix B, **Figure B.3**. Overall, there is a clear increase in I_{Fe}/I_C on electrodes that were functionalized with surface bound ferrocene. The comparison of the bare TPE to any of the ferrocene-bound TPEs is similar to previously reported spectra for homogeneous N_3-PEG3-Fc monolayers.[21] TPEs modified with ferrocene had a percent abundance of 5-10% of iron while those without ferrocene were less than 3% in all ratios. Any nonzero measures of iron in the negative controls can be attributed to possible contaminants in the graphite used to fabricate the TPEs.[29] The relative abundance of iron remained fairly constant across low (1:10), equivalent (1:1), and high (10:1) molar ratios of N_3-PEG3-N_3 to N_3-PEGn-biotin. Thus, it is hypothesized that the resulting TPE surface modifications are relatively consistent regardless of the concentration of click reagents used.

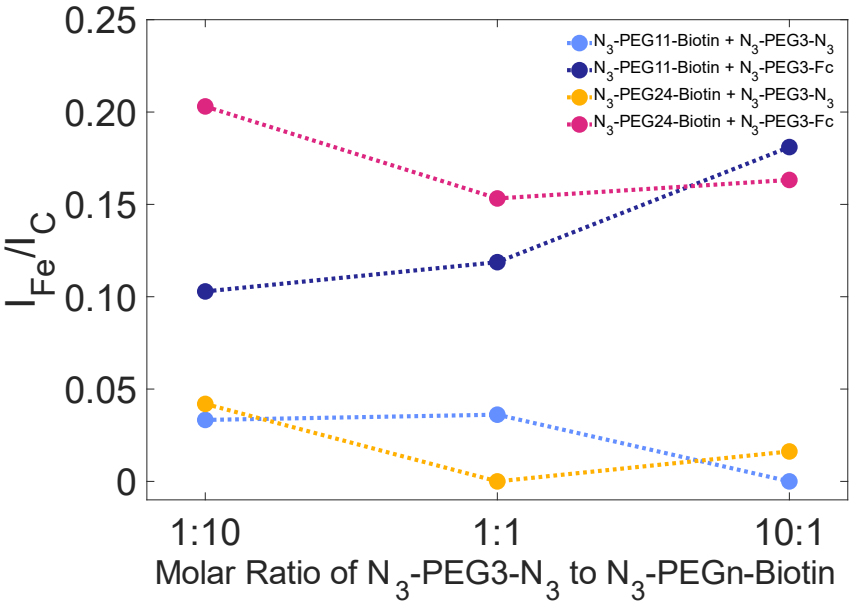

Figure 4.3. Relative abundance of iron to carbon ratio (Ife/IC) for low, equivalent, and high molar ratios of N_3-PEG3-N_3 to N_3-PEGn-biotin with and without surface bound ferrocene as determined via XPS.

Electron transfer kinetics were explored by varying the scan rate of CV. **Figure 4.4** shows representative CVs at scan rates from 5 mV/s to 500 mV/s in 1 mM ferricyanide. In the modified TPEs without ferrocene, the peak currents are lower than that of the modified TPEs with ferrocene. There does not appear to be a significant difference in the electrode performance as a function of the N_3-PEGn-biotin length used, thus, roughly doubling the spacer length from 3.3 nm to 7.2 nm is not a significant hindrance to electron transfer when ferrocene is surface bound.[27, 28] The average peak currents for ferrocene modified TPEs were not linear with respect to the scan rate or the square root of the scan rate indicating that the electron transfer is a combination of surface bound and diffuse redox probes. Equations and corresponding R^2 values are provided in **Table B.1** with poor linear fits for modified electrodes, likely due to the dual contributions to electron transfer of the surface bound ferrocene and ferricyanide in

solution. It is known that relatively short ferrocene terminated PEG (MW = 250 Da) exhibits surface confined behavior.[30] Thus, it is not surprising that the same is evident here with the non-linearity with the square root of the scan rate. On the other hand, it is clear that ferricyanide electron transfer is diffusion dependent. Again, signal rectification is clear with the lack of reduction on the modified TPEs.

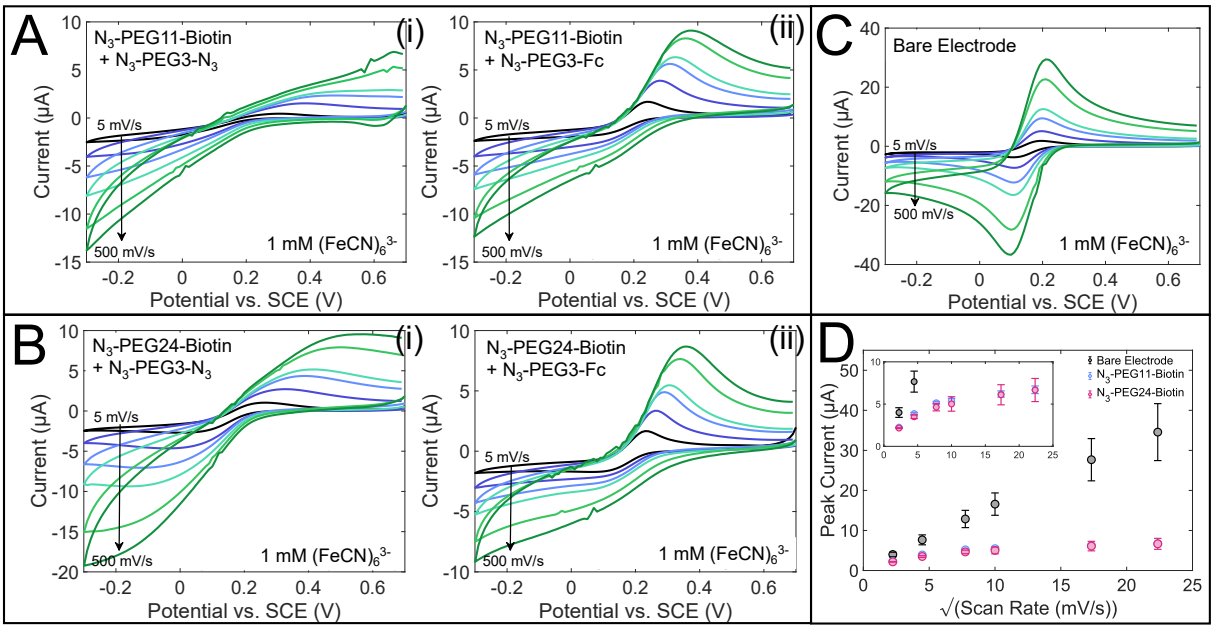

Figure 4.4. Representative CVs at varying scan rate from 5 mV/s to 500 mV/s in 1 mM $Fe(CN)_6^{3-}$ in 0.1 M KCl on **(A)** N_3-PEG11-biotin and **(B)** N_3-PEG24-biotin mixed monolayers **(i)** with and **(ii)** without surface bound ferrocene. **(C)** Bare electrode CVs have significantly higher current and reversibility. **(D)** Randles-Sevcik plots (peak current vs. square root of scan rate) for bare electrode and surface bound ferrocene with N_3-PEG11-biotin and N_3-PEG24-biotin mixed monolayers.

The organization of the monolayer was further examined by electrochemical impedance spectroscopy (EIS). Again, there is not a clear difference between N_3-PEG11-biotin and N_3-PEG24-biotin layers (**Figure 4.5**). However, it is clear that in the absence of surface bound ferrocene, the Nyquist plot shows a complex layer of two thicknesses. One thickness is the height of the N_3-PEG3-N_3 groups while the second thickness is that

of N_3-PEG11-biotin or N_3-PEG24-biotin. On the other hand, in the presence of surface bound ferrocene, the Nyquist plot shows a lower resistance to charge transfer (R_{ct}). The corresponding equivalent circuits are shown in **Figure 4.5B** with the average R_{ct} values (n = 6) from R2 in each circuit type. Examples of the fit to the equivalent circuits are shown in Appendix B, **Figure B.4**. It is true the circuits are a simplification of complex surfaces, but they are reasonable based on the fit, as well as a strong literature precedent.[21, 31, 32] Remarkably, the resistance to charge transfer is reduced by over 200-fold when ferrocene is bound to the TPE surface. The stark difference in R_{ct} is further support of the role of surface bound ferrocene to aid electron transport within the TPE modification layer.

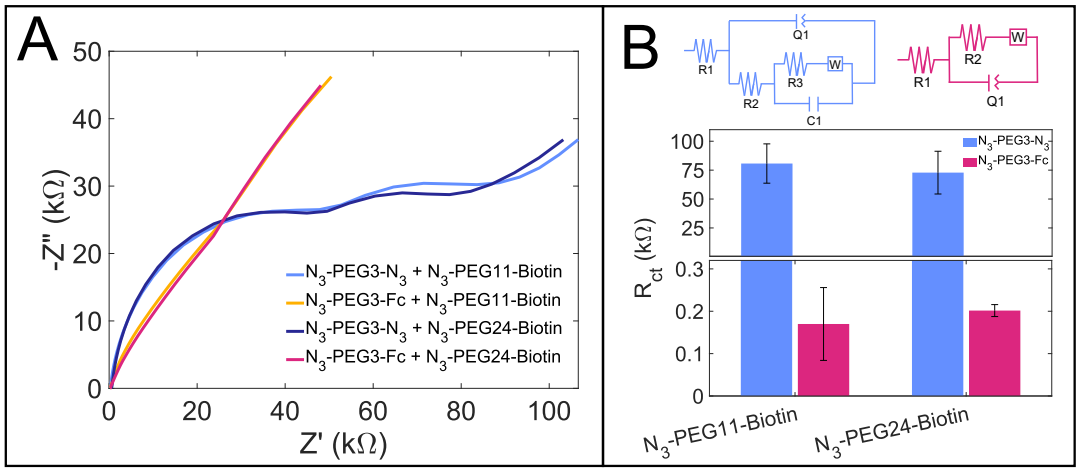

Figure 4.5. (A) Representative Nyquist plots taken in 1 mM $Fe(CN)_6^{3-/4-}$ in 0.1 M KCl with a TPE pseudo-reference. **(B)** Equivalent circuits for with and without ferrocene and R_{ct} (R2) values (n = 6). Break in the y-axis is for clarity.

The motive for these TPE modifications is to develop a label-free immunosensor. Thus, the peak current was measured after incubation of modified electrodes in either phosphate-buffered saline (PBS) or 5 µg/mL of streptavidinated IgG antibody (strep-Ab) in PBS. The electrodes with strep-Ab showed a clear decrease in peak current (**Figure**

4.6) measured by cyclic voltammetry for both N_3-PEG11-biotin and N_3-PEG24-biotin electrodes as expected.[33, 34] Again, there is not an appreciable difference between the PEG11 and PEG24 spacer lengths indicating that the antibody surface density is likely not dependent on the spacer length here. The use of PEG spacers also provides an exciting potential for dual functionality as PEG has been used as a blocker to prevent nonspecific adsorption.[35-38] It is hypothesized that the PEG spacers in this TPE modification protocol will provide the added blocking benefit for immunosensing applications.

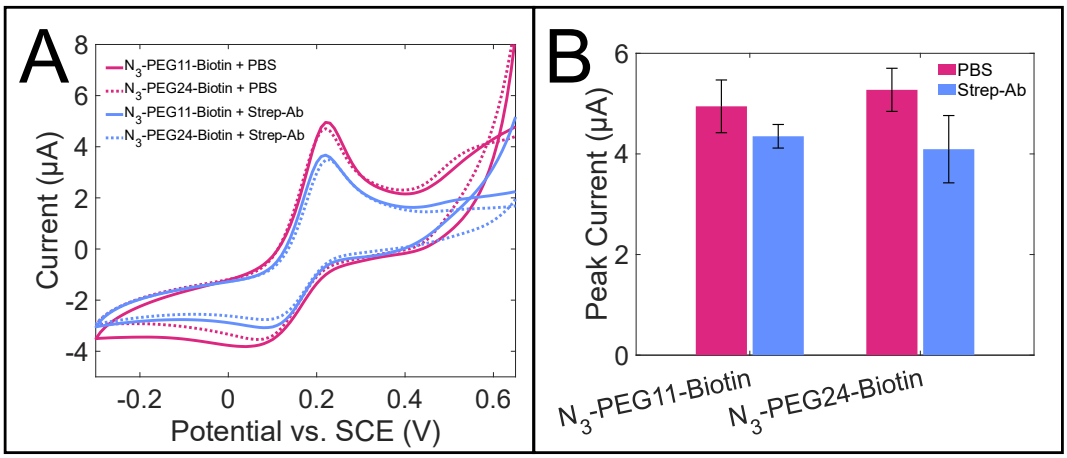

Figure 4.6. (A) Representative CVs in 1 mM $Fe(CN)_6^{3-}$ in 0.1 M KCl at 20 mV/s for PEG11 and PEG24 spacers with and without streptavidin-conjugated antibody. **(B)** Average peak currents (n = 3) showing decrease when strep-Ab is immobilized on the TPE.

As a proof-of-concept, modified electrodes were exposed to 5% bovine serum albumin (BSA) in PBS for 1 hr. The peak currents before and after BSA adsorption are shown in **Figure 4.7** and representative CVs are available in **Figure B.5**. The N_3-PEG11-biotin containing monolayer is the most resistant to signal change from BSA adsorption to the electrode with a 45% decrease in signal. The N_3-PEG3-Fc control and the N_3-PEG24-biotin heterogeneous monolayer electrodes seen decreases in peak current by

82% and 67%, respectively. These results are encouraging as 5% BSA solution is an extreme sample matrix model for nonspecific adsorption. Ignoring cellular debris and other sources of nonspecific adsorption, typical samples for point-of-care diagnostics (blood, urine, and saliva) each have less than 0.02% protein content.[39] Of course, more detailed investigation is needed to understand the efficacy of the blocking ability of the PEG spacers. Little blocking with PEG3 as the only spacer length, thus the length of the spacer should also be further optimized. Previously, it was shown that the length of the PEG chain is less impactful than the surface density of the PEG spacers.[40, 41] A balance should be met between the PEG spacer length and the surface density to provide the optimal immunosensor parameters.

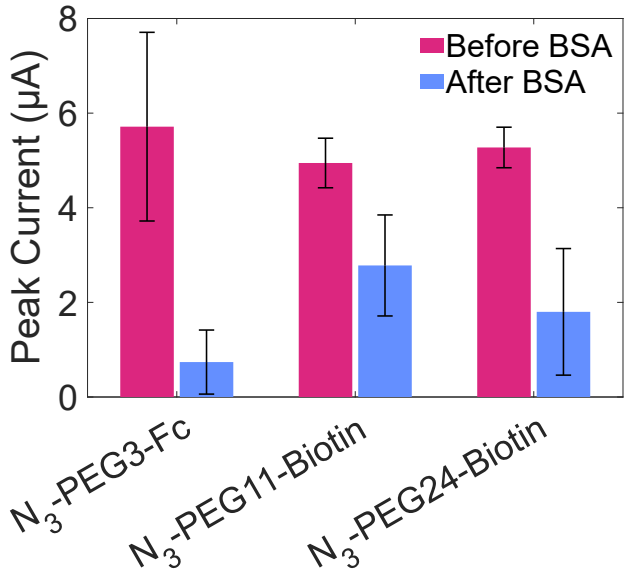

Figure 4.7. Average peak currents (n = 3) before and after exposure to 5% BSA solution for TPEs modified with N_3-PEG3-Fc only and heterogenous monolayers with either N_3-PEG11-biotin or N_3-PEG24-biotin.

A fully assembled immunosensor with anti-N protein IgG antibodies was then tested with inactivated SARS-CoV-2 virus in buffer as a proof-of-concept. **Figure 4.8**

shows the resulting square wave voltammograms and calibration curve for the peak current as a function of concentration of inactivated virus. There is a clear correlation between the concentration of inactivated virus and the peak current in 1 mM ferricyanide (in 0.1 M KCl). For this initial testing, 1% BSA was applied as the blocker to prevent nonspecific adsorption of components in the sample matrix. The limit of detection (LOD) can be estimated by 3x the standard deviation of the intercept of the line of best fit.[42] The LOD is slightly better for the N_3-PEG24-biotin TPEs at 6.0 PFU/mL, compared to 8.4 PFU/mL for N_3-PEG11-biotin TPEs. Both of these values are comparable to or lower than many existing electrochemical sensors for SARS-CoV-2.[34, 43, 44] Additionally, many commercially available diagnostic tests for SARS-CoV-2 have an LOD of approximately 250 PFU/mL.[45] The results here are certainly encouraging, however, more testing is needed to more fully optimized sensor performance and determine the full linear range. For example, it appears that there is not a significant difference between the LOD and sensitivity for N_3-PEG11-biotin versus N_3-PEG24-biotin based TPEs, however shorter or longer PEG spacers may perform better. The blocker for preventing nonspecific adsorption and anti-N protein IgG antibody concentrations and incubation times should also be optimized.

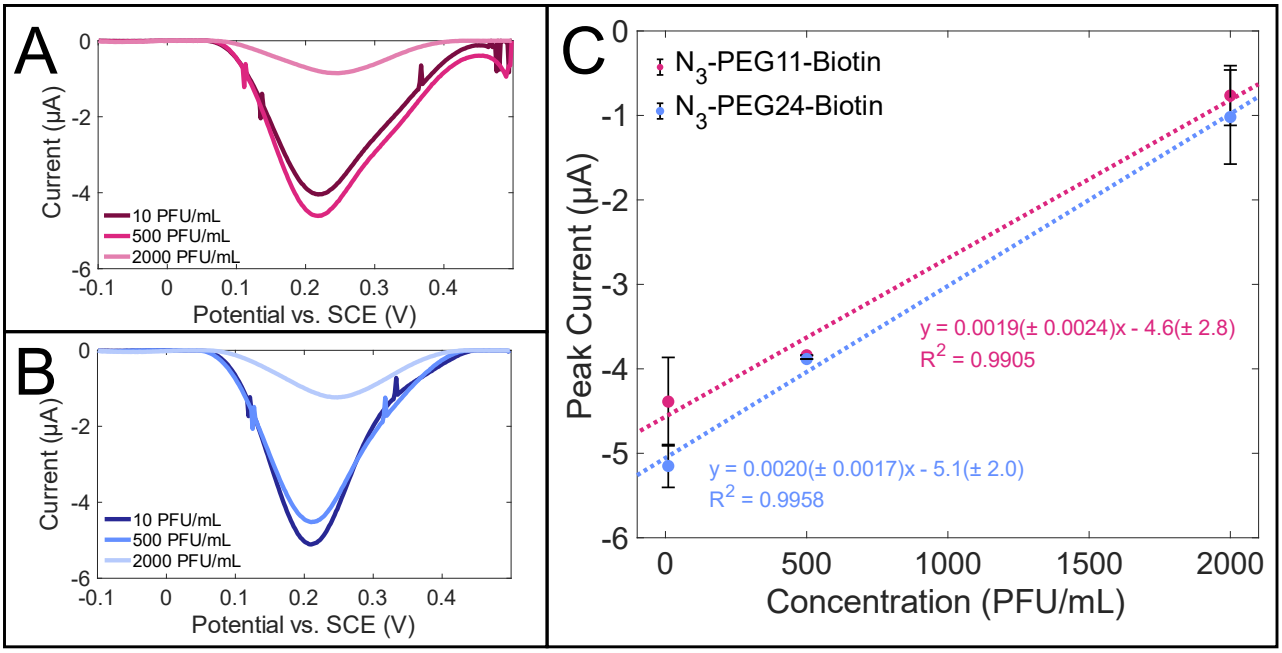

Figure 4.8. Representative square wave voltammograms for **(A)** N_3-PEG11-biotin and **(B)** N_3-PEG24-biotin TPE immunosensors for the SARS-CoV-2 nucleocapsid protein tested in varying concentrations of inactivated virus in buffer. **(C)** The resulting calibration curves show good linearity and similar performance between both PEG spacer lengths.

4.5 Conclusion

Here we present the characterization of a heterogeneous monolayer modification on TPEs for immunosensing applications. The monolayer is the result of using click chemistry to add mixture of N_3-PEG3-N_3 and N_3-PEGn-biotin, which is subsequently modified with ethynyl ferrocene to aid in electron transfer through the modification layer, to a diazonium grafter TPE. We show the increase in electron transfer of ferricyanide with the electrode surface in the presence of surface bound ferrocene and confirm the surface composition with XPS. There was no appreciable difference between the two N_3-PEGn-biotin lengths tested (n=11 and n=24) except when blocking against nonspecific adsorption was tested. Layers with N_3-PEG11-biotin showed more resistance to nonspecific adsorption which is hypothesized to be the result of higher surface density of

the PEG spacer. Both N_3-PEG11-biotin and N_3-PEG24-biotin successfully detected less SARS-CoV-2 N protein with LODs below 10 PFU/mL. Further studies and optimization is needed following this proof-of-concept work.

References

1. Parihar, A.; Ranjan, P.; Sanghi, S. K.; Srivastava, A. K.; Khan, R., Point-of-Care Biosensor-Based Diagnosis of COVID-19 Holds Promise to Combat Current and Future Pandemics. *ACS Applied Bio Materials* **2020,** *3* (11), 7326-7343.

2. Clark, M. F.; Lister, R. M.; Bar-Joseph, M., ELISA techniques. In *Methods in Enzymology*, Academic Press: 1986; Vol. 118, pp 742-766.

3. Bahadır, E. B.; Sezgintürk, M. K., Lateral flow assays: Principles, designs and labels. *TrAC Trends in Analytical Chemistry* **2016,** *82*, 286-306.

4. Ng, A. H. C.; Uddayasankar, U.; Wheeler, A. R., Immunoassays in microfluidic systems. *Analytical and Bioanalytical Chemistry* **2010,** *397* (3), 991-1007.

5. Mollarasouli, F.; Kurbanoglu, S.; Ozkan, S. A., The Role of Electrochemical Immunosensors in Clinical Analysis. *Biosensors (Basel)* **2019,** *9* (3).

6. Sanko, V.; Kuralay, F. Label-Free Electrochemical Biosensor Platforms for Cancer Diagnosis: Recent Achievements and Challenges *Biosensors* [Online], 2023.

7. Vestergaard, M.; delanji; Kerman, K.; Tamiya, E. An Overview of Label-free Electrochemical Protein Sensors *Sensors* [Online], 2007, p. 3442-3458.

8. Cotchim, S.; Thavarungkul, P.; Kanatharana, P.; Limbut, W., Multiplexed label-free electrochemical immunosensor for breast cancer precision medicine. *Analytica Chimica Acta* **2020,** *1130*, 60-71.

9. Galán, T.; Prieto-Simón, B.; Alvira, M.; Eritja, R.; Götz, G.; Bäuerle, P.; Samitier, J., Label-free electrochemical DNA sensor using “click”-functionalized PEDOT electrodes. *Biosensors and Bioelectronics* **2015,** *74*, 751-756.

10. Mao, K.; Wu, D.; Li, Y.; Ma, H.; Ni, Z.; Yu, H.; Luo, C.; Wei, Q.; Du, B., Label-free electrochemical immunosensor based on graphene/methylene blue nanocomposite. *Analytical Biochemistry* **2012,** *422* (1), 22-27.

11. Campuzano, S.; Pingarrón, J. M., Electrochemical Affinity Biosensors: Pervasive Devices with Exciting Alliances and Horizons Ahead. *ACS Sensors* **2023,** *8* (9), 3276-3293.

12. Patel, M.; Agrawal, M.; Srivastava, A., Signal amplification strategies in electrochemical biosensors via antibody immobilization and nanomaterial-based transducers. *Materials Advances* **2022,** *3* (24), 8864-8885.

13. Martins, T. S.; Bott-Neto, J. L.; Machado, S. A. S.; Oliveira, O. N., Jr., Label-Free Electrochemical Immunosensor Made with Tree-like Gold Dendrites for Monitoring 25-Hydroxyvitamin D3 Metabolite. *ACS Applied Materials & Interfaces* **2022,** *14* (27), 31455-31462.

14. Sangili, A.; Kalyani, T.; Chen, S.-M.; Nanda, A.; Jana, S. K., Label-Free Electrochemical Immunosensor Based on One-Step Electrochemical Deposition of AuNP-RGO Nanocomposites for Detection of Endometriosis Marker CA 125. *ACS Applied Bio Materials* **2020,** *3* (11), 7620-7630.

15. de Castro, A. C. H.; Alves, L. M.; Siquieroli, A. C. S.; Madurro, J. M.; Brito-Madurro, A. G., Label-free electrochemical immunosensor for detection of oncomarker CA125 in serum. *Microchemical Journal* **2020,** *155*, 104746.

16. Wu, C.-C.; Chiang, Y.-H.; Chiang, H.-Y. A Label-Free Electrochemical Impedimetric Immunosensor with Biotinylated-Antibody for SARS-CoV-2 Nucleoprotein Detection in Saliva *Biosensors* [Online], 2022.

17. Vashist, S. K., Comparison of 1-Ethyl-3-(3-Dimethylaminopropyl) Carbodiimide Based Strategies to Crosslink Antibodies on Amine-Functionalized Platforms for Immunodiagnostic Applications. *Diagnostics (Basel)* **2012,** *2* (3), 23-33.

18. Liu; Gooding, J. J., An Interface Comprising Molecular Wires and Poly(ethylene glycol) Spacer Units Self-Assembled on Carbon Electrodes for Studies of Protein Electrochemistry. *Langmuir* **2006,** *22* (17), 7421-7430.

19. Klunder, K. J.; Nilsson, Z.; Sambur, J. B.; Henry, C. S., Patternable Solvent-Processed Thermoplastic Graphite Electrodes. *Journal of the American Chemical Society* **2017,** *139* (36), 12623-12631.

20. McCord, C. P.; Summers, B.; Henry, C. S., Simultaneous Analysis of Ascorbic Acid, Uric Acid, and Dopamine at Bare Polystyrene Thermoplastic Electrodes. *ChemElectroChem* **2022,** *9* (11), e202101600.

21. Martinez, B.; Leroux, Y. R.; Hapiot, P.; Henry, C. S., Surface Modification of Thermoplastic Electrodes for Biosensing Applications via Copper-Catalyzed Click Chemistry. *ACS Applied Materials & Interfaces* **2023**.

22. Samper, I. C.; McMahon, C. J.; Schenkel, M. S.; Clark, K. M.; Khamcharoen, W.; Anderson, L. B. R.; Terry, J. S.; Gallichotte, E. N.; Ebel, G. D.; Geiss, B. J.; Dandy, D. S.; Henry, C. S., Electrochemical Immunoassay for the Detection of SARS-CoV-2 Nucleocapsid Protein in Nasopharyngeal Samples. *Analytical Chemistry* **2022,** *94* (11), 4712-4719.

23. Case, J. B.; Bailey, A. L.; Kim, A. S.; Chen, R. E.; Diamond, M. S., Growth, detection, quantification, and inactivation of SARS-CoV-2. *Virology* **2020,** *548*, 39-48.

24. Song, Y.; Li, W.; Ma, C.; Qiao, J.; Li, H.; Hong, C., The Synergistic Effect of Ferrocene and Cu2O to Construct a Sandwich-Type Multi-Signal Amplification Ultra-

Sensitive Immunosensor for Carcinoembryonic Antigen Detection. *Journal of The Electrochemical Society* **2020,** *167* (2), 027538.

25. Ning, S.; Zhou, M.; Liu, C.; Waterhouse, G. I. N.; Dong, J.; Ai, S., Ultrasensitive electrochemical immunosensor for avian leukosis virus detection based on a β-cyclodextrin-nanogold-ferrocene host-guest label for signal amplification. *Analytica Chimica Acta* **2019,** *1062*, 87-93.

26. Alleman, K. S.; Weber, K.; Creager, S. E., Electrochemical Rectification at a Monolayer-Modified Electrode. *The Journal of Physical Chemistry* **1996,** *100* (42), 17050-17058.

27. Oesterhelt, F.; Rief, M.; Gaub, H. E., Single molecule force spectroscopy by AFM indicates helical structure of poly(ethylene-glycol) in water. *New Journal of Physics* **1999,** *1* (1), 6.

28. Cruje, C.; Chithrani, D. B., Polyethylene Glycol Density and Length Affects Nanoparticle Uptake by Cancer Cells *Journal of Nanomedicine Research* **2014,** *1* (1).

29. Koshino, Y.; Narukawa, A., Determination of trace metal impurities in graphite powders by acid pressure decomposition and inductively coupled plasma atomic emission spectrometry. *Analyst* **1993,** *118* (7), 827-830.

30. Steentjes, T.; Jonkheijm, P.; Huskens, J., Electron Transfer Processes in Ferrocene-Modified Poly(ethylene glycol) Monolayers on Electrodes. *Langmuir* **2017,** *33* (43), 11878-11883.

31. Saxena, R.; Srivastava, S., An insight into impedimetric immunosensor and its electrical equivalent circuit. *Sensors and Actuators B: Chemical* **2019,** *297*, 126780.

32. Wang, B.; Jing, R.; Qi, H.; Gao, Q.; Zhang, C., Label-free electrochemical impedance peptide-based biosensor for the detection of cardiac troponin I incorporating

gold nanoparticles modified carbon electrode. *Journal of Electroanalytical Chemistry* **2016,** *781*, 212-217.

33. Sajadpour, M.; Abbasian, S.; Siampour, H.; Bagheri, H.; Moshaii, A., Label-free PSA electrochemical determination by seed-mediated electrochemically-deposited gold nanoparticles on an FTO electrode. *Journal of Solid State Electrochemistry* **2022,** *26* (1), 149-161.

34. Mojsoska, B.; Larsen, S.; Olsen, D. A.; Madsen, J. S.; Brandslund, I.; Alatraktchi, F. A. Rapid SARS-CoV-2 Detection Using Electrochemical Immunosensor *Sensors* [Online], 2021.

35. Horiguchi, Y.; Nakayama, N.; Kanayama, N.; Nagasaki, Y., Sulfobetaine-terminated PEG improves the qualities of an immunosensing surface. *Biomaterials Science* **2014,** *2* (6), 819-826.

36. Figueroa-Miranda, G.; Wu, C.; Zhang, Y.; Nörbel, L.; Lo, Y.; Tanner, J. A.; Elling, L.; Offenhäusser, A.; Mayer, D., Polyethylene glycol-mediated blocking and monolayer morphology of an electrochemical aptasensor for malaria biomarker detection in human serum. *Bioelectrochemistry* **2020,** *136*, 107589.

37. Kingshott, P.; Thissen, H.; Griesser, H. J., Effects of cloud-point grafting, chain length, and density of PEG layers on competitive adsorption of ocular proteins. *Biomaterials* **2002,** *23* (9), 2043-2056.

38. Liu, B.; Huang, P.-J. J.; Zhang, X.; Wang, F.; Pautler, R.; Ip, A. C. F.; Liu, J., Parts-per-Million of Polyethylene Glycol as a Non-Interfering Blocking Agent for Homogeneous Biosensor Development. *Analytical Chemistry* **2013,** *85* (21), 10045-10050.

39. Crosley, L. K.; Duthie, S. J.; Polley, A. C.; Bouwman, F. G.; Heim, C.; Mulholland, F.; Horgan, G.; Johnson, I. T.; Mariman, E. C.; Elliott, R. M.; Daniel, H.; de Roos, B., Variation in protein levels obtained from human blood cells and biofluids for platelet, peripheral blood mononuclear cell, plasma, urine and saliva proteomics. *Genes Nutr* **2009,** *4* (2), 95-102.

40. Reimhult, E.; Höök, F. Design of Surface Modifications for Nanoscale Sensor Applications *Sensors* [Online], 2015, p. 1635-1675.

41. Gillich, T.; Benetti, E. M.; Rakhmatullina, E.; Konradi, R.; Li, W.; Zhang, A.; Schlüter, A. D.; Textor, M., Self-Assembly of Focal Point Oligo-catechol Ethylene Glycol Dendrons on Titanium Oxide Surfaces: Adsorption Kinetics, Surface Characterization, and Nonfouling Properties. *Journal of the American Chemical Society* **2011,** *133* (28), 10940-10950.

42. Miller, J. N., Basic statistical methods for Analytical Chemistry. Part 2. Calibration and regression methods. A review. *Analyst* **1991,** *116* (1), 3-14.

43. Torres, M. D. T.; de Araujo, W. R.; de Lima, L. F.; Ferreira, A. L.; de la Fuente-Nunez, C., Low-cost biosensor for rapid detection of SARS-CoV-2 at the point of care. *Matter* **2021,** *4* (7), 2403-2416.

44. Xu, L.; Li, D.; Ramadan, S.; Li, Y.; Klein, N., Facile biosensors for rapid detection of COVID-19. *Biosensors and Bioelectronics* **2020,** *170*, 112673.

45. Stanley, S.; Hamel, D. J.; Wolf, I. D.; Riedel, S.; Dutta, S.; Contreras, E.; Callahan, C. J.; Cheng, A.; Arnaout, R.; Kirby, J. E.; Kanki, P. J., Limit of Detection for Rapid Antigen Testing of the SARS-CoV-2 Omicron and Delta Variants of Concern Using Live-Virus Culture. *J Clin Microbiol* **2022,** *60* (5), e0014022.

CHAPTER 5 – Conclusions and Future Directions

5.1 Conclusions

Improvements to current label-free electrochemical immunosensors are needed to reduce costs and increase stability, while expanding the dynamic ranges and limits of detection. The work in this dissertation seeks to fill this gap by developing a label-free immunosensor platform using thermoplastic electrodes (TPEs) modified with aryl diazonium grafting followed by click chemistry. The initial attempts to immobilize antibodies on TPEs was examined, only to find that traditional techniques such as EDC/NHS crosslinking are unsuitable. This revealed the need to apply a new modification technique for antibody immobilization on TPEs.

The remainder of the dissertation presented an alternative technique for antibody immobilization involving a three step modification including: aryl diazonium grafting, click chemistry, and biotin-streptavidin conjugation.[1] The utility of the new approach is in its wide versatility with the ability to easily change antibodies, PEG spacer lengths or other components. This was demonstrated with the modification of TPEs with heterogeneous monolayers of mixtures of N_3-PEG3-N_3 with N_3-PEGn-biotin which allowed a second click reaction to bind ethynyl ferrocene to the surface. This allowed for an increase in electron transfer with ferricyanide, limited blocking of nonspecific adsorption, while providing stable and consistent antibody immobilization for detection of SARS-CoV-2 nucleocapsid protein (N protein). The ability to produce multifunctional modifications on the electrodes with few steps is a significant advantage over alternatives where each function (blocking, signal enhancement, and antibody attachment) requires individual modification steps. Overall, the potential applications of TPEs in biosensing

has been greatly expanded by this work providing an option for a durable, yet inexpensive, carbon electrode immunosensor.

As for broader impacts, the research in this dissertation provides the basis for a new label-free immunosensor technologies that can provide better options for point-of-care (POC) and point-of-need (PON) diagnostics. As previously mentioned, most commercial SARS-CoV-2 sensors achieve limits of detection (LODs) of approximately 250 PFU/mL.[2] While this is a good screening tool and accepted by the World Health Organization standards, more sensitive detection is needed to confirm infection.[3] Instead of waiting hours or even days for RT-PCR confirmation of COVID-19 infection, patients could get sensitive and accurate results within minutes, reducing the burden on the healthcare system while getting high risk patients the treatment they need sooner.

Detecting SARS-CoV-2 N protein is just the beginning for potential analytes compatible with the techniques developed in this work given the ability to swap antibodies easily. Additionally, the work focuses on TPEs due to their advantages over other types of carbon electrodes, however the mild conditions of the surface functionalizations in this work are hypothesized to be applicable to any desired carbon electrode, given compatibility in water and ethanol solutions. The impact of the methods and results presented in this dissertation is expected to be broad due to the versatility and adaptability of the approach.

5.2 Future Directions

The potential for expanding this body of work is immense. The natural course is to first continue optimization of the SARS-CoV-2 N protein detection presented in Chapter 4. The optimization of the N protein sensor would serve as a model for subsequent

immunosensors targeting other analytes given the versatility of the antibody attachment technique. As mentioned, antibody and blocker type, concentration and incubation times should be optimized to determine the best performance. Nonspecific binding is one of the largest impacts on label-free sensor performance, as such, determining the best blocker conditions should be a priority.[4] Ideally, the blocking can be done with the PEG spacers built into the TPE modifications. Different surface concentrations and lengths of N_3-PEGn-biotin should be tested to determine the most beneficial for blocking nonspecific adsorption while maintaining high sensitivity. However, in the event that an extra blocking component is still required, potential alternatives to bovine serum albumin (BSA) are aged casein and superblock, both of which have shown success in electrochemical immunosensors.[4, 5] Once the performance of the sensor, in terms of sensitivity, dynamic range, and LOD, is optimized, testing should include multiple variants and clinical samples to further support the success of the sensor.

Ideally, the sensor platform developed here will be implemented into a system that can be used at the point-of-need or point-of-care to be of most use to the public. The optimized N protein sensor on TPEs could be integrated with microfluidic devices to aid in sample delivery to the electrode. The Henry group has recently published sandwich-type electrochemical immunosensor for the detection of N protein with an LOD of 45 PFU/mL.[6] The existing system uses screen printed carbon electrodes (SPCEs) and the swap to TPEs with the antibody immobilization and surface modifications in this work can improve the sensitivity and LOD while also increasing the durability.

Exciting options for further expansion of the click chemistry modifications brings about the potential to multiplex detection and detect different target antigens. The methods in this dissertation rely on streptavidin conjugated to the antibody of choice

meaning that swapping the antibody for a different antigen should not impact the function of the sensor other than the specific target. **Figure 5.1** illustrates a potential device where there are three working electrodes, each modified with a different antibody, for the detection of three different antigens. For example, influenza, SARS-CoV-2, and respiratory syncytial virus (RSV) are all respiratory viruses with similar symptoms that tend to circulate the population at the same time of year.[7] It can be helpful to healthcare professionals and patients to be able to diagnose the illness early to provide the patient with the proper treatment immediately. In the proposed device, the user would provide a nasal swab sample and swirl in a lysing buffer to deactivate the viruses present and expose the antigens for capture on the electrodes. Further, recent advances in potentiostat technology has provided much easier means of obtaining electrochemical measurements using a smart phone to give a readout of test results.[8-10]

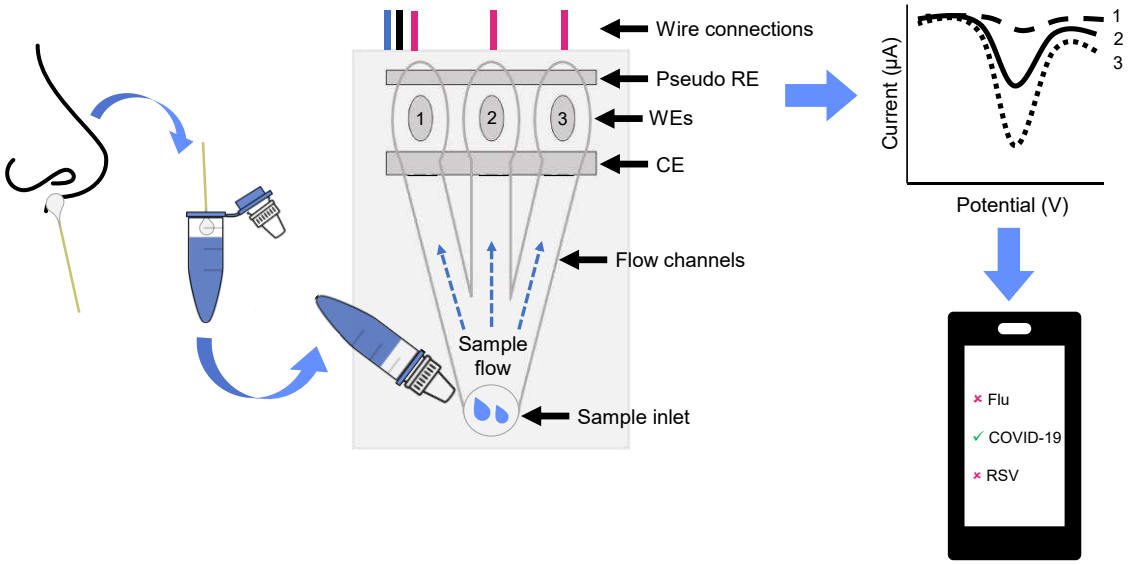

Figure 5.1. Illustration of potential applications of TPE immunosensors in a multiplexed device for simultaneous detection of three respiratory viruses in a user friendly format. (RE = reference electrode, WE = working electrode, CE = counter electrode).

While TPEs are more durable and have higher electrochemical performance than stencil- and screen-printed carbon electrodes (SPCEs), SPCEs remain easier to manufacture and are commercially available.[11, 12] This trade-off provides an exciting option for developing improved SPCE-based immunosensors that are more easily integrated with microfluidics to get devices in the hands of healthcare professionals and patients more quickly. Diazonium grafting and click chemistry have been shown to be successful on SPCEs, though they have not been used sequentially to created heterogeneous, multifunctional, monolayers as done in this work.[13-16]

Another avenue of expansion on this work is in the biorecognition element used. Antibodies are convenient due to their wide availability and high specificity, however, nanobodies and aptamers are two alternatives that have shown great advantages.[17] Nanobodies are small fragments of antibodies that have higher stability and increased affinity over traditional antibodies.[18] Nanobodies are a relatively new area, yet a few examples of electrochemical sensors have been developed using nanobodies as the biorecognition element successfully.[19, 20] Aptamers, nucleotide strands that selectively bind target molecules, have seen an increase in popularity over the last decade due to their high stability and ease of synthesizing.[21, 22] Many researchers have turned to aptamers for electrochemical sensors, including using click chemistry to attach the aptamers to the electrode surface due to the ease of synthesizing azide-terminated aptamers.[14, 23-25] Both nanobodies and aptamers are exciting options for expanding the immunosensor fabrication methods developed in this dissertation.

In conclusion, the outlined research lays a strong foundation for potential breakthroughs in the field of electrochemical immunosensors. First, optimization of the N protein sensor paves the way for an immunosensor fabrication process with broad

analyte applications. Second, the prospect of integrating the sensor into a user-friendly POC device, with the possibility of multiplexed detection for various respiratory viruses, holds significant promise for advancing public health initiatives. Finally, the exploration of alternative carbon electrodes (i.e. SPCEs) and biorecognition elements (i.e. nanobodies and aptamers) presents exciting avenues for future research and development.

References

1. Martinez, B.; Leroux, Y. R.; Hapiot, P.; Henry, C. S., Surface Modification of Thermoplastic Electrodes for Biosensing Applications via Copper-Catalyzed Click Chemistry. *ACS Applied Materials & Interfaces* **2023**.

2. Stanley, S.; Hamel, D. J.; Wolf, I. D.; Riedel, S.; Dutta, S.; Contreras, E.; Callahan, C. J.; Cheng, A.; Arnaout, R.; Kirby, J. E.; Kanki, P. J., Limit of Detection for Rapid Antigen Testing of the SARS-CoV-2 Omicron and Delta Variants of Concern Using Live-Virus Culture. *J Clin Microbiol* **2022,** *60* (5), e0014022.

3. WHO; Print, R. D. B.; C-Tap COVID-19 Target product profiles for priority diagnostics to support response to the COVID-19 pandemic v.1.0. https://www.who.int/publications/m/item/covid-19-target-product-profiles-for-priority-diagnostics-to-support-response-to-the-covid-19-pandemic-v.0.1.

4. Contreras-Naranjo, J. E.; Aguilar, O. Suppressing Non-Specific Binding of Proteins onto Electrode Surfaces in the Development of Electrochemical Immunosensors *Biosensors* [Online], 2019.

5. Balcer, H. I.; Spiker, J. O.; Kang, K. A., Effects of Blocking Buffers and Plasma Proteins on the Protein C Biosensor Performance. In *Oxygen Transport to Tissue XXIV*, Dunn, J. F.; Swartz, H. M., Eds. Springer US: Boston, MA, 2003; pp 133-141.

6. Samper, I. C.; McMahon, C. J.; Schenkel, M. S.; Clark, K. M.; Khamcharoen, W.; Anderson, L. B. R.; Terry, J. S.; Gallichotte, E. N.; Ebel, G. D.; Geiss, B. J.; Dandy, D. S.; Henry, C. S., Electrochemical Immunoassay for the Detection of SARS-CoV-2 Nucleocapsid Protein in Nasopharyngeal Samples. *Analytical Chemistry* **2022,** *94* (11), 4712-4719.

7. Prevention, C. f. D. C. a. Protect yourself from COVID-19, Flu, and RSV. https://www.cdc.gov/respiratory-viruses/index.html (accessed Oct 31).

8. Beck, J. J.; Alenicheva, V.; Rahn, K. L.; Russo, M. J.; Baldo, T. A.; Henry, C. S., Evaluating the performance of an inexpensive, commercially available, NFC-powered and smartphone controlled potentiostat for electrochemical sensing. *Electroanalysis* **2023,** *n/a* (n/a), e202200552.

9. Colozza, N.; Chebil, A.; Arduini, F., Chapter Four - Smartphone-integrated electrochemical (bio)sensors as smart and reliable analytical tools. In *Comprehensive Analytical Chemistry*, Nelis, J. L. D.; Tsagkaris, A. S., Eds. Elsevier: 2023; Vol. 101, pp 73-108.

10. Keçili, R.; Ghorbani-Bidkorbeh, F.; Dolak, İ.; Canpolat, G.; Hussain, C. M., 2 - Smartphone-based optical and electrochemical sensing. In *Smartphone-Based Detection Devices*, Hussain, C., Ed. Elsevier: 2021; pp 19-36.

11. Klunder, K. J.; Nilsson, Z.; Sambur, J. B.; Henry, C. S., Patternable Solvent-Processed Thermoplastic Graphite Electrodes. *Journal of the American Chemical Society* **2017,** *139* (36), 12623-12631.

12. Adkins, J.; Boehle, K.; Henry, C., Electrochemical paper-based microfluidic devices. *ELECTROPHORESIS* **2015,** *36* (16), 1811-1824.

13. Jasmin, J.-P.; Cannizzo, C.; Dumas, E.; Chaussé, A., Fabrication and characterization of all-covalent nanocomposite functionalized screen-printed voltammetric sensors. *Electrochimica Acta* **2014,** *133*, 467-474.

14. Xie, D.; Li, C.; Shangguan, L.; Qi, H.; Xue, D.; Gao, Q.; Zhang, C., Click chemistry-assisted self-assembly of DNA aptamer on gold nanoparticles-modified

screen-printed carbon electrodes for label-free electrochemical aptasensor. *Sensors and Actuators B: Chemical* **2014,** *192*, 558-564.

15. Hetemi, D.; Noël, V.; Pinson, J., Grafting of Diazonium Salts on Surfaces: Application to Biosensors. *Biosensors (Basel)* **2020,** *10* (1).

16. Edward Sekhosana, K.; Majeed, S. A.; Feleni, U., Click chemistry in the electrochemical systems: Toward the architecture of electrochemical (bio)sensors. *Coordination Chemistry Reviews* **2023,** *491*, 215232.

17. Dhar, P.; Samarasinghe, R. M.; Shigdar, S. Antibodies, Nanobodies, or Aptamers—Which Is Best for Deciphering the Proteomes of Non-Model Species? *Int J Mol Sci* [Online], 2020.

18. Jin, B. K.; Odongo, S.; Radwanska, M.; Magez, S., Nanobodies: A Review of Generation, Diagnostics and Therapeutics. *Int J Mol Sci* **2023,** *24* (6).

19. Campuzano, S.; Salema, V.; Moreno-Guzmán, M.; Gamella, M.; Yáñez-Sedeño, P.; Fernández, L. A.; Pingarrón, J. M., Disposable amperometric magnetoimmunosensors using nanobodies as biorecognition element. Determination of fibrinogen in plasma. *Biosensors and Bioelectronics* **2014,** *52*, 255-260.

20. Trashin, S.; Morales-Yánez, F.; Thiruvottriyur Shanmugam, S.; Paredis, L.; Carrión, E. N.; Sariego, I.; Muyldermans, S.; Polman, K.; Gorun, S. M.; De Wael, K., Nanobody-Based Immunosensor Detection Enhanced by Photocatalytic-Electrochemical Redox Cycling. *Analytical Chemistry* **2021,** *93* (40), 13606-13614.

21. Lakhin, A. V.; Tarantul, V. Z.; Gening, L. V., Aptamers: problems, solutions and prospects. *Acta Naturae* **2013,** *5* (4), 34-43.

22. Thiviyanathan, V.; Gorenstein, D. G., Aptamers and the next generation of diagnostic reagents. *Proteomics Clin Appl* **2012,** *6* (11-12), 563-73.

23. Flauzino, J. M. R.; Nalepa, M.-A.; Chronopoulos, D. D.; Šedajová, V.; Panáček, D.; Jakubec, P.; Kührová, P.; Pykal, M.; Banáš, P.; Panáček, A.; Bakandritsos, A.; Otyepka, M., Click and Detect: Versatile Ampicillin Aptasensor Enabled by Click Chemistry on a Graphene–Alkyne Derivative. *Small* **2023,** *n/a* (n/a), 2207216.

24. An, Y.; Jin, T.; Zhu, Y.; Zhang, F.; He, P., An ultrasensitive electrochemical aptasensor for the determination of tumor exosomes based on click chemistry. *Biosensors and Bioelectronics* **2019,** *142*, 111503.

25. Hayat, A.; Sassolas, A.; Marty, J.-L.; Radi, A.-E., Highly sensitive ochratoxin A impedimetric aptasensor based on the immobilization of azido-aptamer onto electrografted binary film via click chemistry. *Talanta* **2013,** *103*, 14-19.

APPENDIX A – Supporting Information for Chapter 3: Surface Modification of Thermoplastic Electrodes for Biosensing Applications via Copper-Catalyzed Click Chemistry

Table of Contents

Figure A.6. Representative CVs in 1 mM $Fc(MeOH)_2$ or 1 mM $Fe(CN)_6^{3-/4-}$ with varying concentration of diazonium solution (4-TMS-ethynylaniline with excess $NaNO_2$ in 0.1 M HCl). Potential is versus carbon pseudo reference.

Figure A.7. Representative CVs for diazonium grafted electrodes in **(A)** 1 mM $Fe(CN)_6^{3-/4-}$ or **(B)** 1 mM $Fc(MeOH)_2$ in 0.1 M KCl electrolyte solution as a function of scan rate. Randles-Sevcik plots of anodic and cathodic peak currents in **(C)** $Fc(MeOH)_2$ with linear fits. Error bars represent the standard deviation in n=3 electrodes. Potential is versus carbon pseudo reference.

Figure A.8. Representative CVs in **(A)** 1 mM $Fc(MeOH)_2$ or **(B)** 1 mM $Fe(CN)_6^{3-/4-}$ to monitor the effectiveness of deprotection protocol for removal of the TMS protecting group prior to click chemistry reaction. Potential is versus carbon pseudo-reference.

Figure A.9. Representative CVs in 10 mM $Fe(CN)_6^{3-/4-}$ with a scan rate of 80 mV/s of biotin, biotin-streptavidin, and biotin-streptavidinated antibody modified electrodes compared to previous modification steps and bare electrode.

Figure A.10. Representative CVs of biotin clicked electrodes in **(A)** 1 mM $Fe(CN)_6^{3-/4-}$ or **(B)** 1 mM $Fc(MeOH)_2$ in 0.1 M KCl electrolyte solution as a function of scan rate. Randles-Sevcik plots of anodic and cathodic peak currents in **(C)** $Fc(MeOH)_2$ with linear fits. Error bars represent the standard deviation in n=3 electrodes. Potential is versus carbon pseudo reference.

Table A.1. Percent error values for the R_{ct} calculated from equivalent circuit fitting.

References

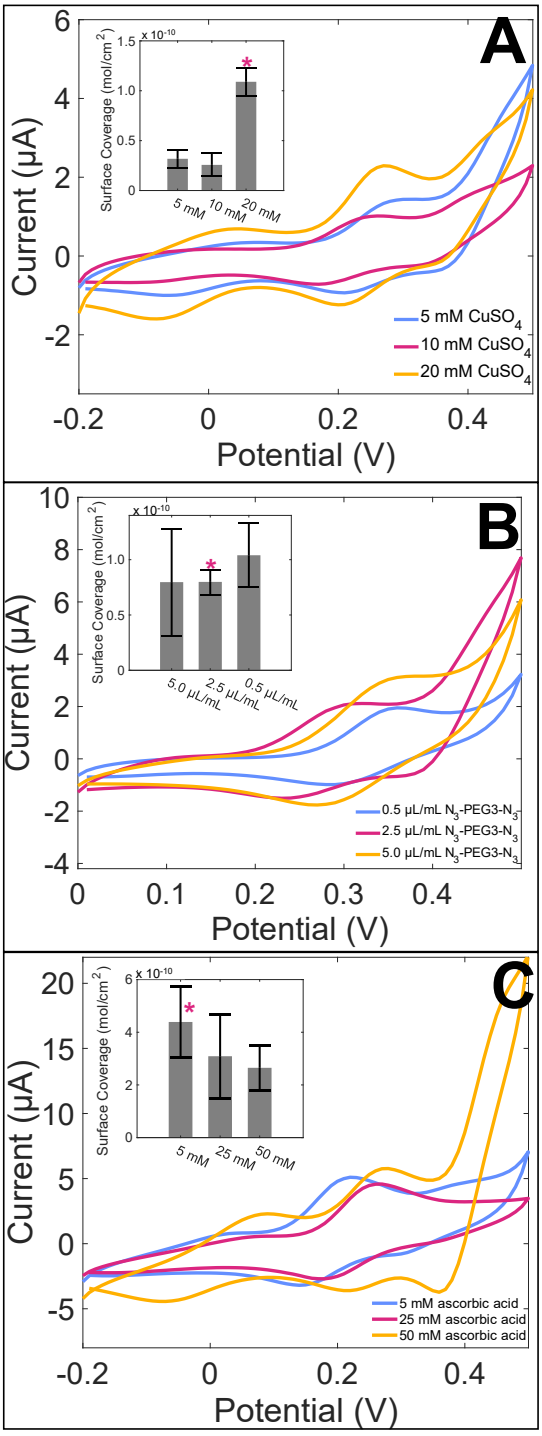

Figure A.1. Representative CVs in 0.1 M KCl from the optimization of $CuSO_4$ (**A**), N_3-PEG3-N_3 (**B**), and ascorbic acid (**C**) using the ethynyl ferrocene clicked to the surface as the redox probe. Surface coverage was calculated by taking the area under the oxidation peak as the current density. * Indicates the condition that was used for the remainder of the work. Potential is versus carbon pseudo reference.

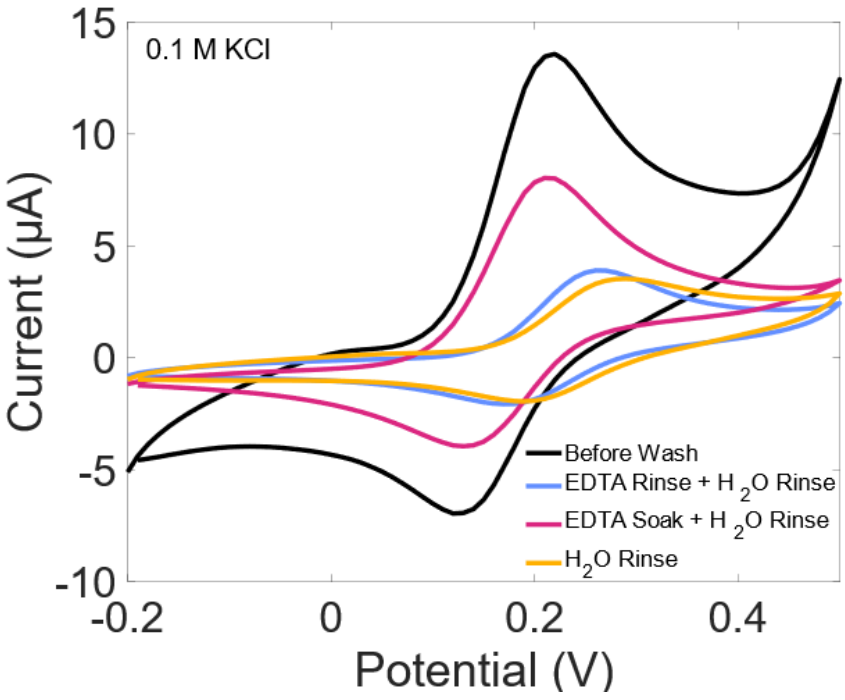

Figure A.2. Representative CVs in 0.1 M KCl for the optimization of the wash step following click chemistry reaction on TPE. Potential is versus carbon pseudo reference.

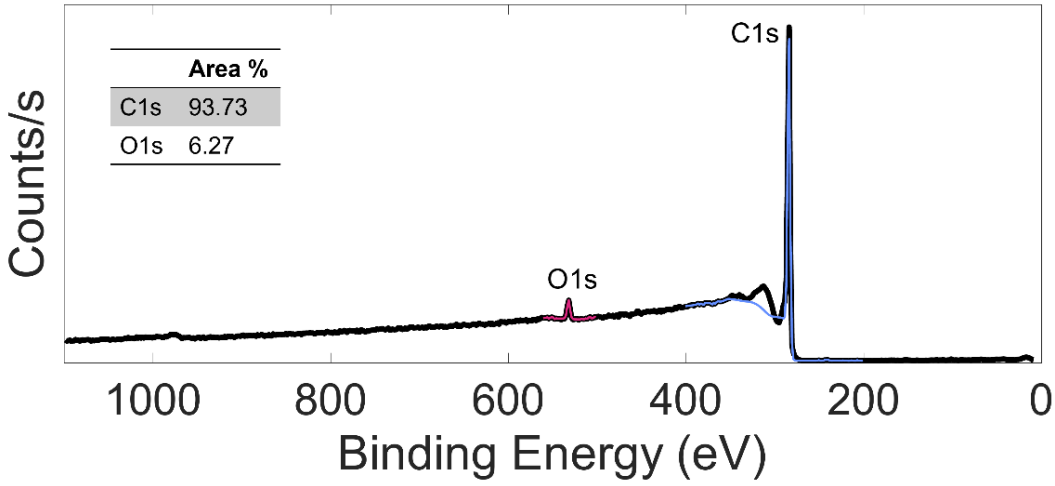

Figure A.3. Full survey spectrum using XPS to examine surface composition of the bare electrode. Peak fits are shown for C1s (blue) and O1s (pink) peaks. The oxygen to carbon content (I_O/I_C) was determined to be 0.067.

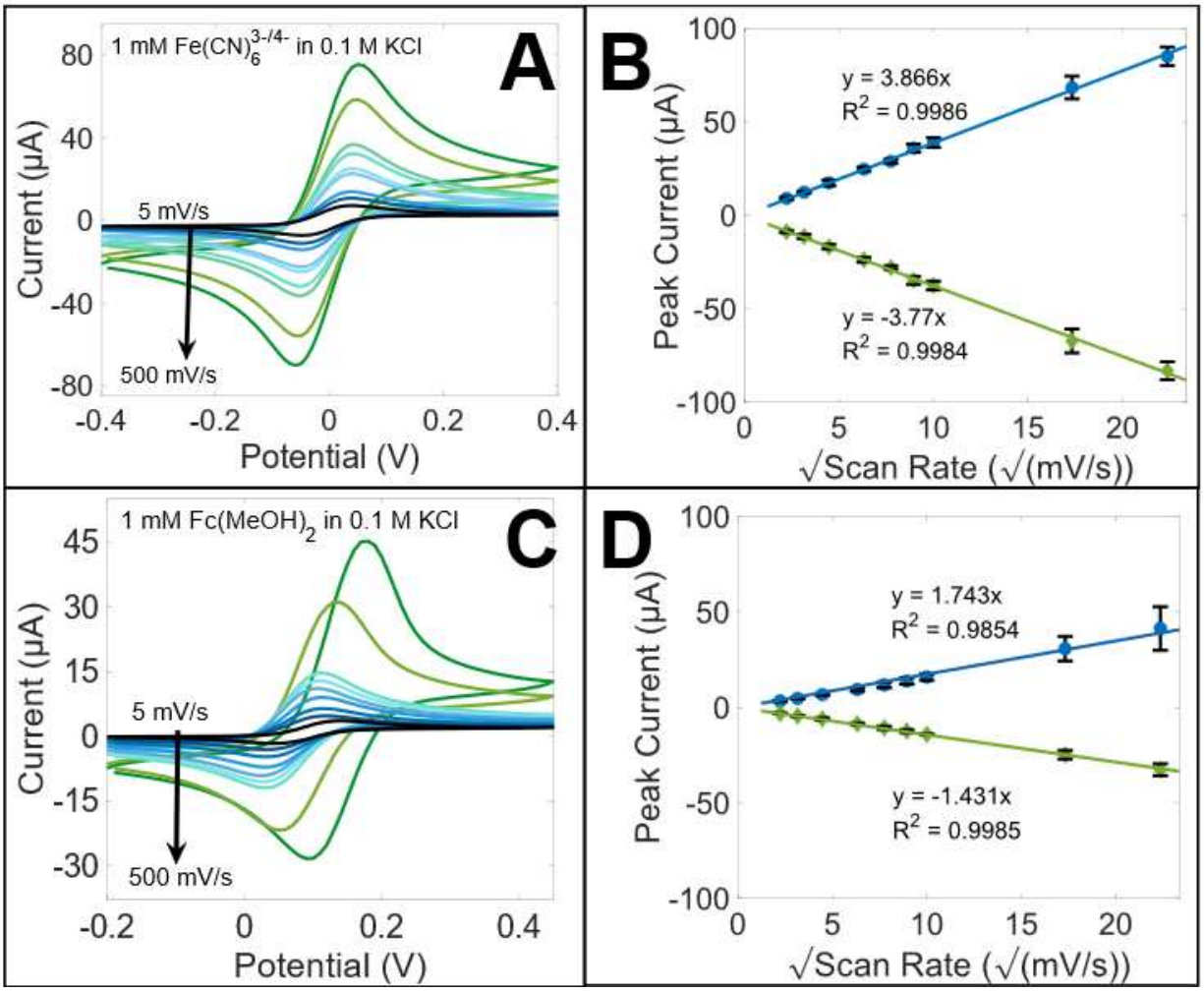

Figure A.4. Representative CVs in **(A)** 1 mM $Fe(CN)_6^{3-/4-}$ or **(C)** 1 mM $Fc(MeOH)_2$ in 0.1 M KCl electrolyte solution as a function of scan rate. Potential is with respect to a TPE pseudo-reference. Randles-Sevcik plots of anodic and cathodic peak currents in **(B)** $Fe(CN)_6^{3-/4-}$ and **(D)** $Fc(MeOH)_2$ with linear fits. Error bars represent the standard deviation in n=3 electrodes.

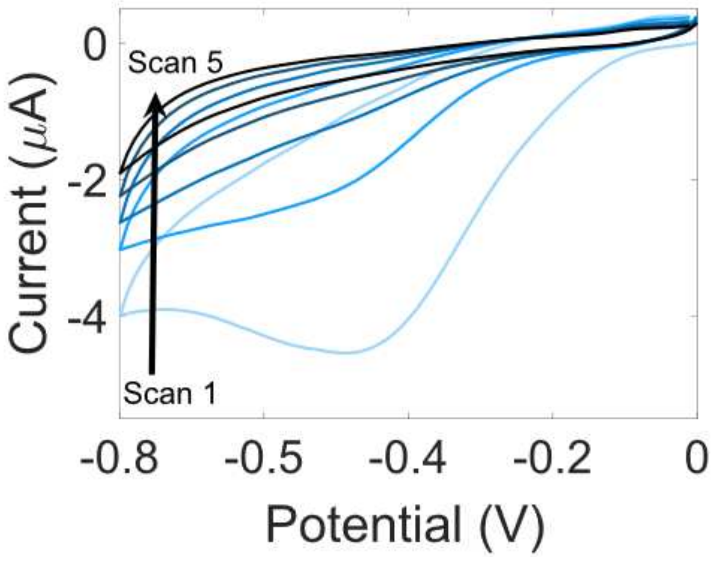

Figure A.5. Representative CVs from the electrografting of 0.5 mM of 4-ethynylbenzenediamine (produced *in situ*) onto the surface of the thermoplastic electrodes (TPEs). These curves are comparable to those previously reported in the literature.[1-3] Potential is versus carbon pseudo reference.

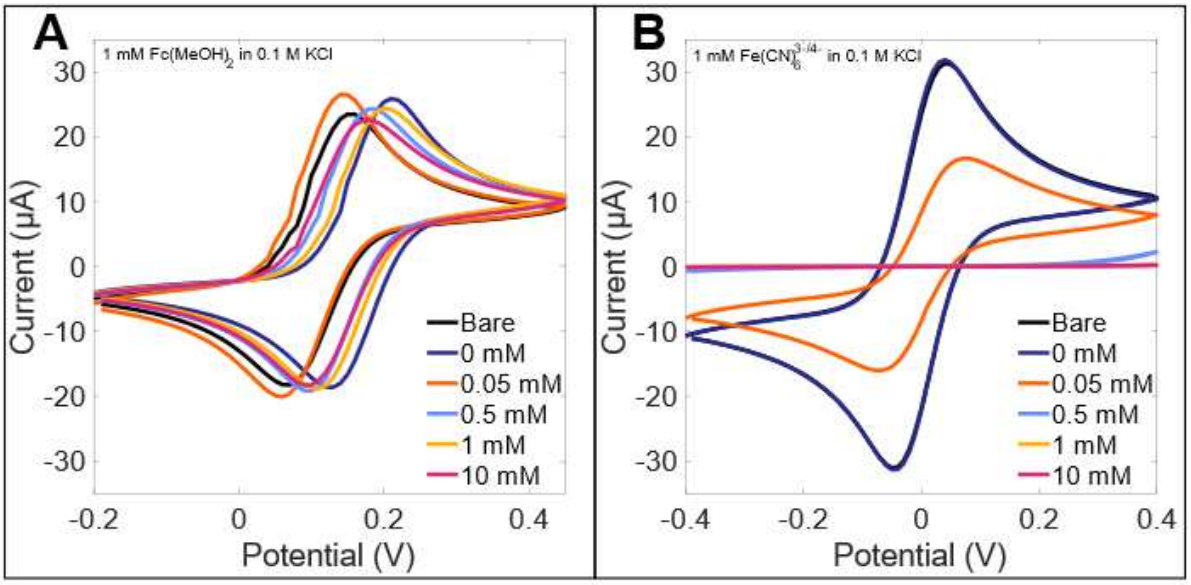

Figure A.6. Representative CVs in 1 mM $Fc(MeOH)_2$ or 1 mM $Fe(CN)_6^{3-/4-}$ with varying concentration of diazonium solution (4-TMS-ethynylaniline with excess $NaNO_2$ in 0.1 M HCl). Potential is versus carbon pseudo reference.

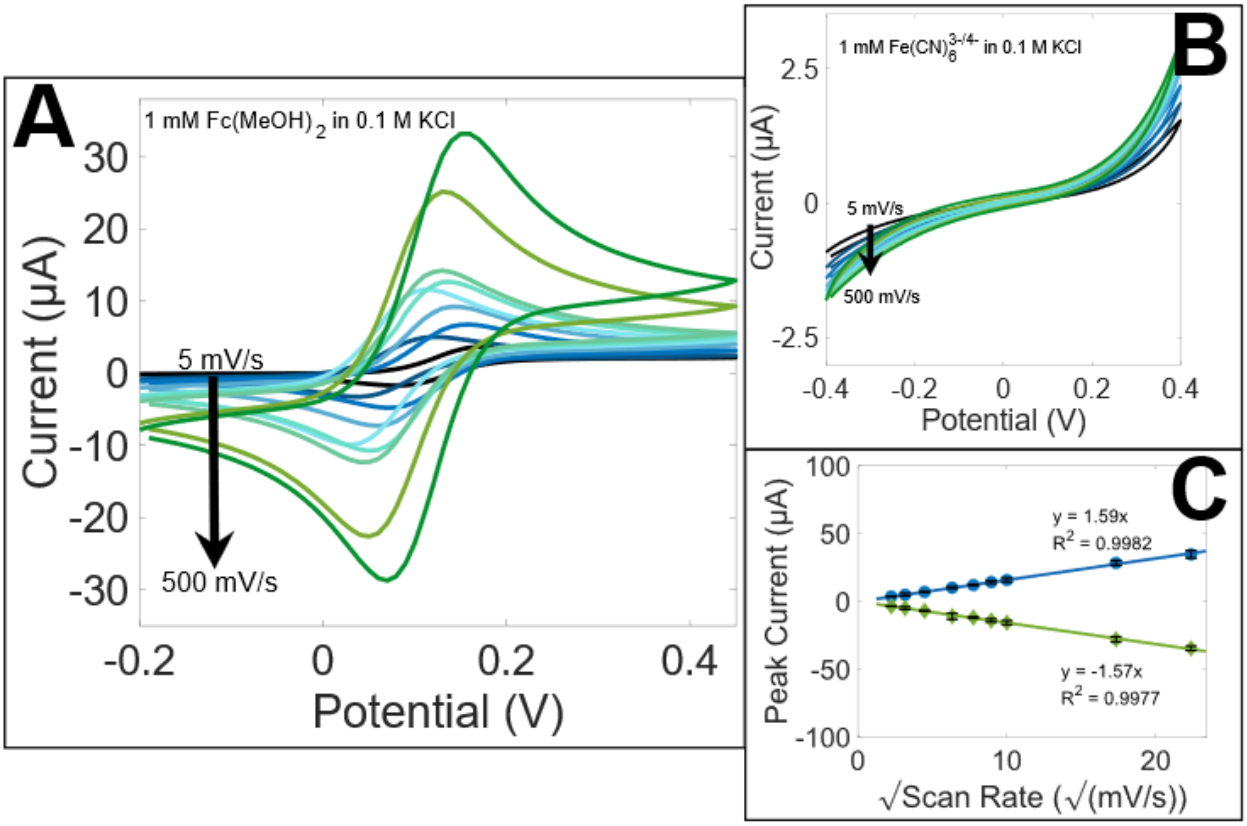

Figure A.7. Representative CVs for diazonium grafted electrodes in **(A)** 1 mM $Fe(CN)_6^{3-/4-}$ or **(B)** 1 mM $Fc(MeOH)_2$ in 0.1 M KCl electrolyte solution as a function of scan rate. Randles-Sevcik plots of anodic and cathodic peak currents in **(C)** $Fc(MeOH)_2$ with linear fits. Error bars represent the standard deviation in n=3 electrodes. Potential is versus carbon pseudo reference.

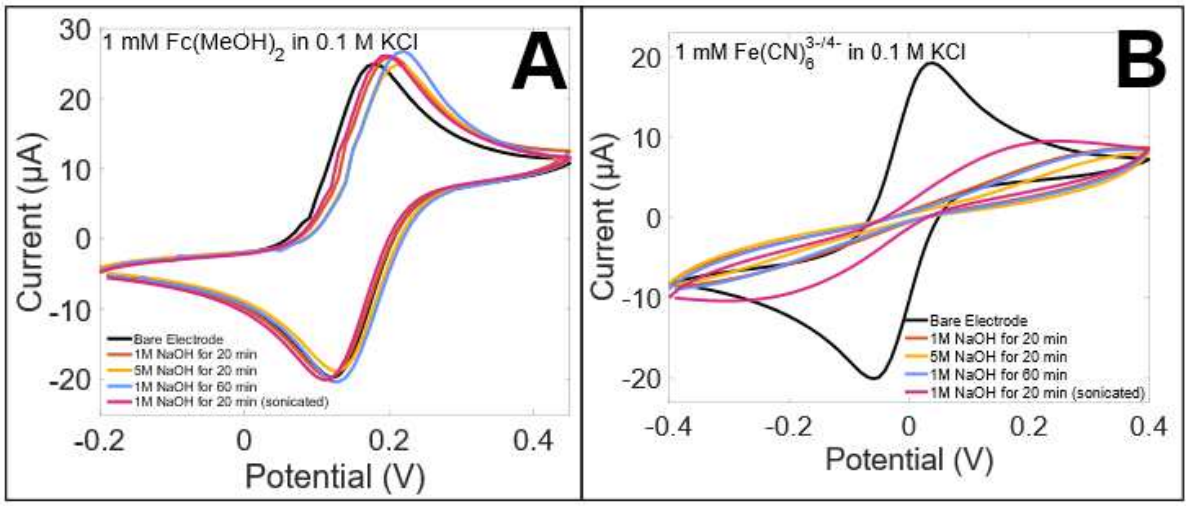

Figure A.8. Representative CVs in **(A)** 1 mM $Fc(MeOH)_2$ or **(B)** 1 mM $Fe(CN)_6^{3-/4-}$ to monitor the effectiveness of deprotection protocol for removal of the TMS protecting group prior to click chemistry reaction. Potential is versus carbon pseudo-reference.

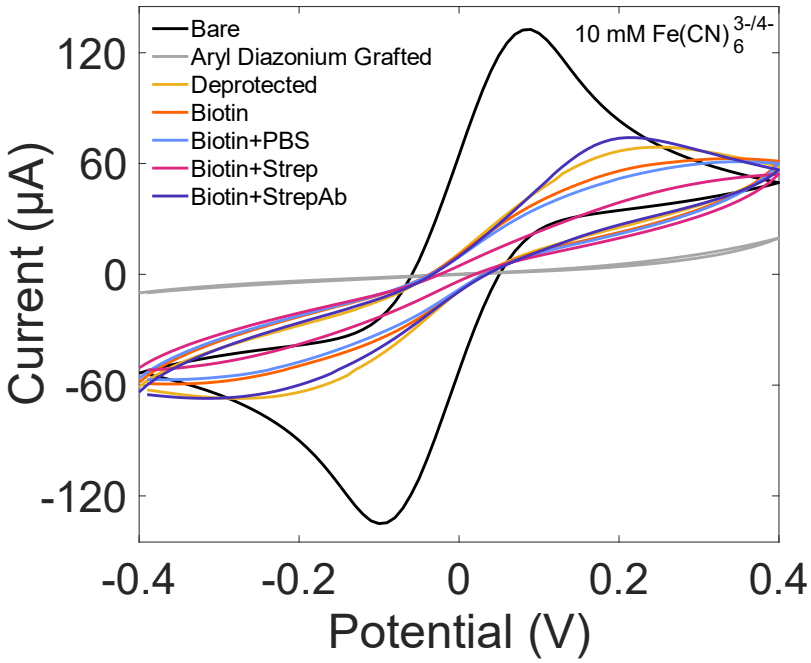

Figure A.9. Representative CVs in 10 mM $Fe(CN)_6^{3-/4-}$ in 0.1 M KCl with a scan rate of 80 mV/s of biotin, biotin-streptavidin, and biotin-streptavidinated antibody modified electrodes compared to previous modification steps and bare electrode.

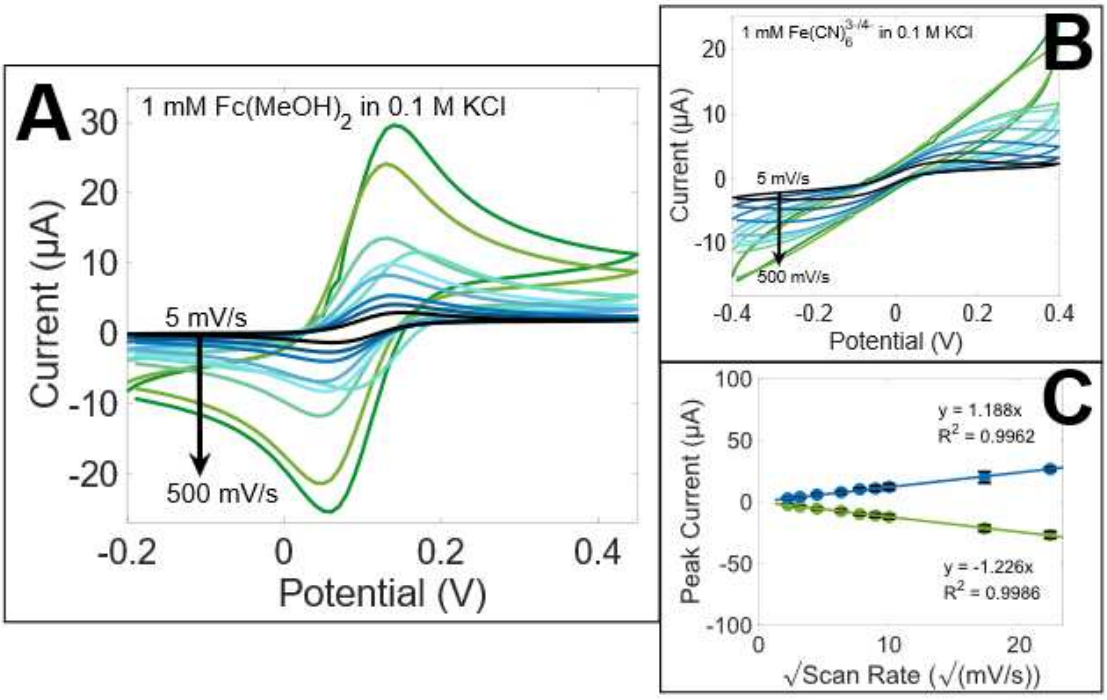

Figure A.10. Representative CVs of biotin clicked electrodes in **(A)** 1 mM $Fe(CN)_6^{3-/4-}$ or **(B)** 1 mM $Fc(MeOH)_2$ in 0.1 M KCl electrolyte solution as a function of scan rate. Randles-Sevcik plots of anodic and cathodic peak currents in **(C)** $Fc(MeOH)_2$ with linear fits. Error bars represent the standard deviation in n=3 electrodes. Potential is versus carbon pseudo reference.

Table A.1. Percent error values for the R_{ct} calculated from equivalent circuit fitting.

	Average % Error of Fit (n=3)
Biotin	2.8 ± 1.0%
Biotin+PBS	3.2 ± 0.1%
Biotin+Strep	2.2 ± 0.4%
Biotin+StrepAb	2.7 ± 0.6%

References

1. Pinson, J.; Podvorica, F., Attachment of organic layers to conductive or semiconductive surfaces by reduction of diazonium salts. *Chemical Society Reviews* **2005,** *34* (5), 429-439.

2. Berg, K. E.; Leroux, Y. R.; Hapiot, P.; Henry, C. S., Increasing Applications of Graphite Thermoplastic Electrodes with Aryl Diazonium Grafting. *ChemElectroChem* **2019,** *6* (18), 4811-4816.

3. Leroux, Y. R.; Hui, F.; Noël, J.-M.; Roux, C.; Downard, A. J.; Hapiot, P., Design of Robust Binary Film onto Carbon Surface Using Diazonium Electrochemistry. *Langmuir* **2011,** *27* (17), 11222-11228.

APPENDIX B - Supporting Information for Chapter 4: Characterization of Heterogeneous Polyethylene Glycol Monolayers with Surface-Bound Ferrocene on Thermoplastic Electrodes for Label-Free Immunosensing Applications

Table of Contents

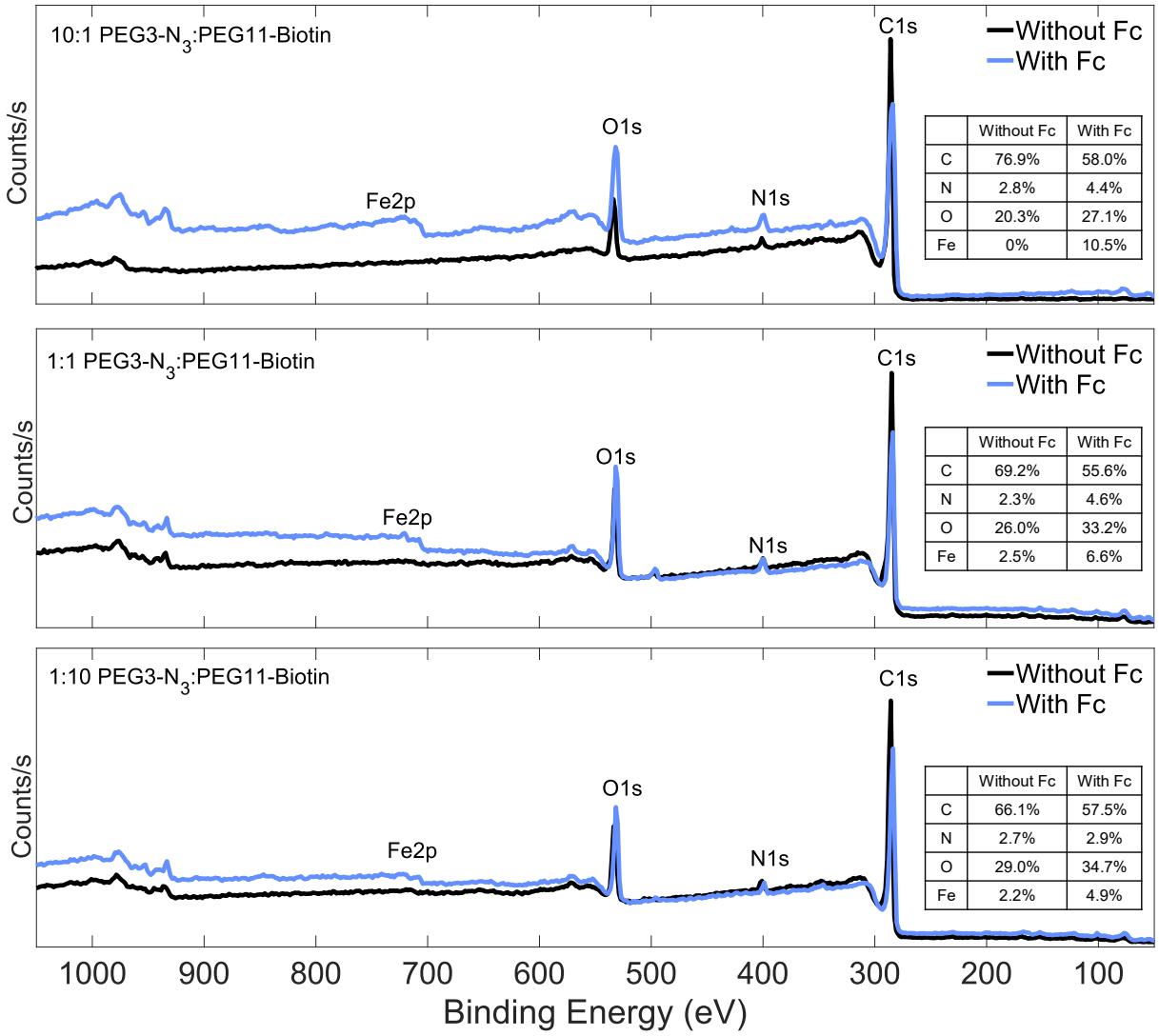

Figure B.1. XPS survey spectra for high (top), equivalent (middle) and low (bottom) molar ratios of N_3-PEG3-N_3 to N_3-PEG11-biotin with (blue) and without (black) surface bound ferrocene. Relative percent abundances are shown in the inset tables.

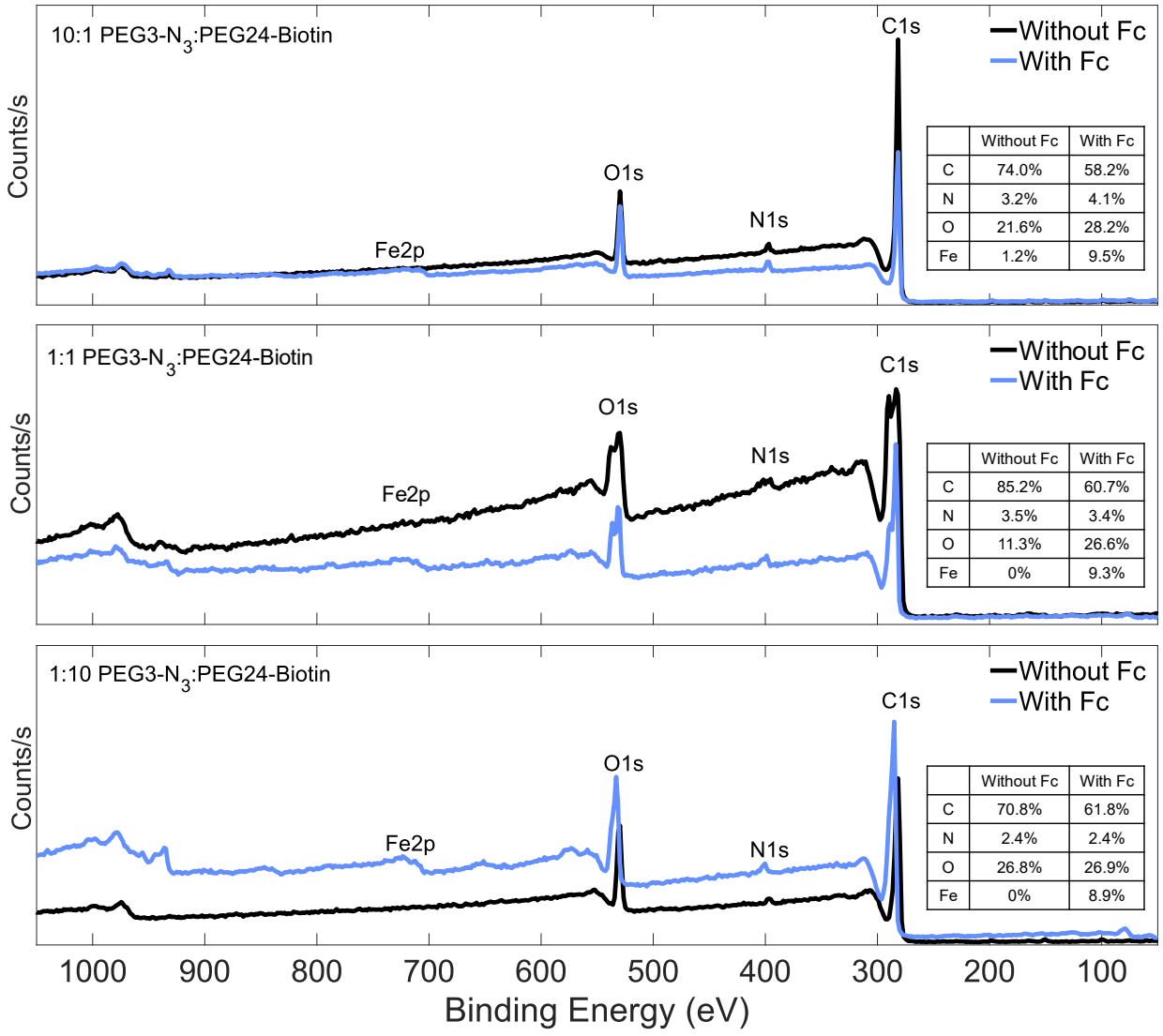

Figure B.2. XPS survey spectra for high (top), equivalent (middle) and low (bottom) molar ratios of N_3-PEG3-N_3 to N_3-PEG24-biotin with (blue) and without (black) surface bound ferrocene. Relative percent abundances are shown in the inset tables.

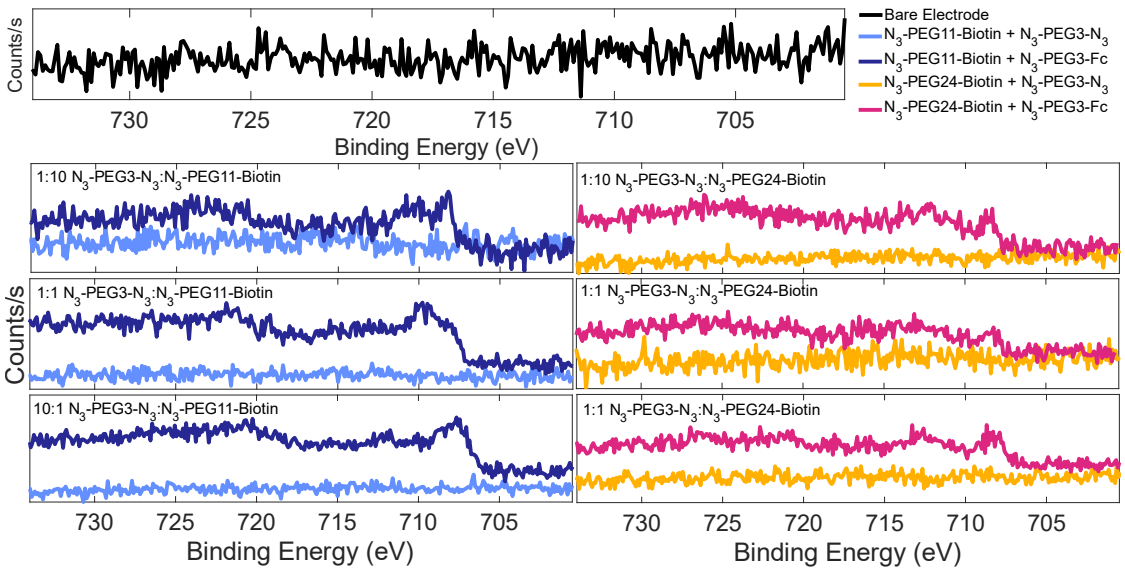

Figure B.3. Fe2p high resolution XPS spectra for low, equivalent, and high molar ratios of N_3-PEG3-N_3 to N_3-PEGn-biotin with and without surface bound ferrocene. Bare TPE Fe2p high resolution spectrum is shown at the top for comparison to modified TPEs.

Table B.1. Curve fitting for peak currents as a function of scan rate and square root of scan rate.

Electrode Modification Type	Peak Current (μA) vs. Scan Rate (mV/s)	Peak Current (μA) vs. √Scan Rate (√(mV/s))
Bare TPE	$y = 0.080(\pm 0.029)x$ $R^2 = 0.667$	$y = 1.58(\pm 0.05)x$ $R^2 = 0.997$
N3-PEG11-Biotin	$y = 0.018 (\pm 0.014)x$ $R^2 = -3.00$	$y = 0.38(\pm 0.15)x$ $R^2 = -0.346$
N3-PEG24-Biotin	$y = 0.017(\pm 0.013)x$ $R^2 = -2.09$	$y = 0.37(\pm 0.13)x$ $R^2 = 0.0796$

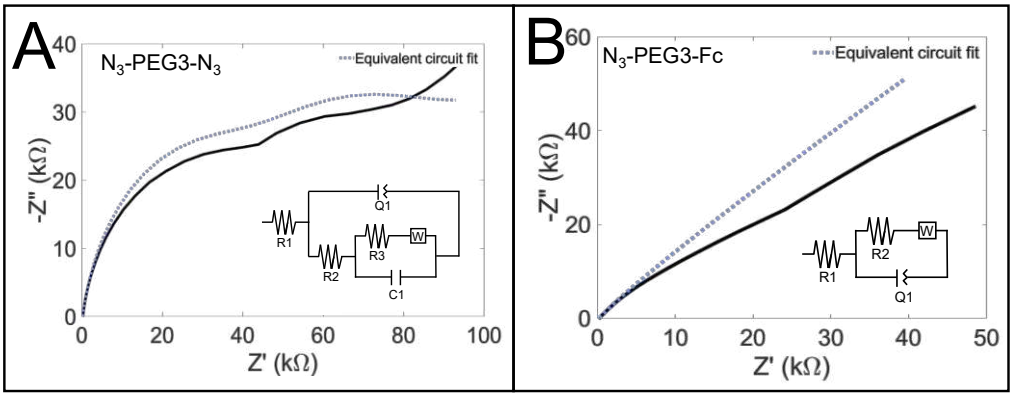

Figure B.4. Equivalent circuits and fits for representative Nyquist plots for **(A)** without ferrocene and **(B)** with ferrocene bound to the TPE surface.

APPENDIX C – ^{1}H-NMR Profiling of Short-Chain Fatty Acid Content from a Physiologically Accurate Gut-on-a-Chip Device

C.1 Overview

The following work was published in *Analytical Chemistry* during the first two years of my PhD work and was my preliminary exam area of focus.[1] It is on an unrelated project to the rest of the dissertation and was completed in collaboration with Dr. Luke A. Schwerdtfeger and Dr. Stuart A. Tobet for tissue maintenance and manipulation and Alec Richardson, who designed the microfluidic device and helped with sample collection. I completed all ^{1}H-NMR experiments and data analysis after initial training by Dr. Chris Rithner and Dr. Claudia Boot of the Materials and Molecular Analysis Center at the CSU Analytical Resources Core.

It has been shown that short-chain fatty acids (SCFAs) produced by the gut microbiome are of importance to host tissue health; however, measuring such compounds in biological samples is often limited to using hours to days old fecal and blood plasma samples. Organ-on-a-chip models have been created to simplify the complexity but struggle to reproduce the full biology of the gut specifically. We recently reported a tissue-in-a-chip gut model that incorporates gut explanted tissue into a microfluidic device. The system maintains a biologically relevant oxygen gradient and tissue ex vivo for days at a time, but minimal characterization of biological activity was reported. Herein, we use ^{1}H-NMR to analyze the SCFA content of tissue media effluents from gut explants cultured in the recently developed microfluidic organotypic device (MOD). ^{1}H-NMR can identify key SCFAs in the complex samples with minimal sample preparation. Our findings show that maintaining physiologically relevant oxygen conditions, something often missing from many other culture systems, significantly impacts the SCFA profile. Additionally, we

noted the changes in SCFAs with culture time and potential variability between SCFA levels in male and female mouse tissue explants cultured in the MOD system based on ^{1}H-NMR spectral profiles.

C.2 Introduction

Short-chain fatty acids (SCFAs), defined here as carboxylic acids with 1-6 aliphatic carbons, are by-products of anaerobic metabolism by the gut microbiome. Collectively, they have become increasingly correlated with various human health conditions.1 Among the wide ranging impacts are correlations to depression, colon cancer, and type 2 diabetes.[2-5] The three most prevalent SCFAs, acetate, butyrate, and propionate, constitute upwards of 90% of the total SCFA content in the human body which is in the range of 100 – 200 mM.[5-8] Abnormally high levels of propionate in fecal samples are linked to higher risk of type 2 diabetes while increased fecal butyrate levels were shown to aid insulin production, thus reducing risk of type 2 diabetes.[4] Both propionate and butyrate have been correlated to a number of other conditions including ulcerative colitis,[9] and decreased butyrate producing gut microbes have been noted in Parkinson's disease[10] and in multiple sclerosis patients.[11]

Much of what we know about SCFAs correlation to human diseases comes from studies of fecal samples and mechanistic studies are difficult to perform. Alternative approaches for generating biologically analyzable samples include human gut via in vitro cultures or animal studies, principally murine in vitro culture techniques, which can allow for measurement of the total SCFA content across the gut wall and feces rather than just the approximately 5% in fecal samples.[4] One in vitro device focused on the impact of oxygen conditions on the microbiome with engineered tissue (using Caco-2 cells co-

cultured with selected gastrointestinal bacteria) used GC-MS to compare the subsequent impact of oxygen culture condition on metabolites.[12] The device was also used to show impacts of pre- and probiotic supplementation on gut microbial metabolism including SCFAs.[13] However, in vitro studies of the gut have pitfalls centered around the inability to recapitulate the broad cellular diversity and complex 3D tissue structure of the in vivo gut wall.[14]

Addressing this issue brought about the development of gut-on-a-chip devices which aim to recreate in vivo conditions in a controlled environment.[15, 16] One such device uses cultured human Caco-2 intestinal epithelial cells in a PDMS chip that can mimic the peristaltic movement of the gut.[17] Other work aims to replicate the natural microbiome, cellular diversity with cultured tissues, and the natural oxygen gradient across the tissue.[18-21] A notable advancement in the development of gut-on-a-chip devices is the use of ex vivo culture of intestinal tissue which are attractive due to the total preservation of cellular diversity and structure, with an intact microbiome.[16, 22] The work presented here is based on the recently developed ex vivo system, the Microfluidic Organotypic Device (MOD).[23]

Current methods for SCFA analysis primarily involve collecting fecal or blood samples either from humans or model organisms which are then filtered and the SCFAs derivatized before analysis via gas chromatography.[24, 25] Liquid chromatography-mass spectrometry has been used for analyzing metabolite profiles from human colon tissue culture supernatants[26] and fecal samples[27] ^{1}H-NMR. Metabolite profiles produced from ^{1}H-NMR of fecal and blood samples have also been used to analyze SCFA levels.[25, 28, 29] Each of these techniques of analysis has benefits, however ^{1}H-NMR is particularly attractive due to no need for extensive sample prep, a shortened instrumentation time,

and highly reproducible results over GC-MS.[30] Mass spectrometry based methods may also be limited in their universality. Each SCFA may not react with the derivatizing agent required for GC-MS or LC-MS in the same manner and different SCFA derivatives may have varying degrees of chromatographic resolution or fragmentation.[31, 32] Each of these factors impact the degree to which each respective SCFA can be quantified. Despite decreased sensitivity compared to GC-MS or LC-MS methods, ^{1}H-NMR is highly quantitative and is sufficient for many biological samples, including SCFA analysis and has been used in metabolomics for over thirty years.[30, 33, 34] Particularly attractive are the many options for biological samples using ^{1}H-NMR. High-resolution magic-angle-spinning ^{1}H-NMR spectroscopy (HR-MAS NMR) is great for whole intact tissue analysis, for example.[35]

Here ^{1}H-NMR is used to investigate SCFA production in MOD cultured ex vivo samples as a function of oxygen concentrations as a further demonstration of the value of the platform for studying gut tissue under physiologically relevant conditions. The use of ^{1}H-NMR over gas or liquid chromatography allows for more rapid screening with minimal sample preparation. ^{1}H-NMR has been used previously for fecal samples and other biological fluids to provide profiles for SCFA analysis.[36-38] In this work, the sample profiles are the basis for proof-of-concept for the detection of SCFAs in tissue media collected from gut tissue explants cultured in the MOD. This work further supports the importance of accounting for native tissue oxygen levels when generating tissue cultures while outlining the feasibility of using the MOD culture system for determination of SCFA levels in the gut with spatial and temporal resolution.

C.3 Materials and Methods

Tissue and MOD set-up.

Mouse colon explants were collected from 8-12 week old C57BL/6 mice and maintained in MODs as previously described.[23] Explants were maintained in media composed of CTS Neurobasal-A Medium (Thermo Fisher Scientific, Waltham, MA, USA) with 2% (v/v) B-27 Supplement (Thermo Fisher Scientific, Waltham, MA, USA), 5% (v/v) HEPES buffer (Sigma Aldrich, St. Louis, MO) supplemented with 10 μM of the L-type calcium ion channel blocker nicardipine (Sigma Aldrich, St. Louis, MO). Fractions of media from both serosal and mucosal channels of the tissue were collected in ten-hour increments from t = 0 to t = 50 hours and stored at -80°C until use. Ambient samples were cultured in media at atmospheric O_2 levels (~ 100 mmHg) in both channels, while gradient samples had ambient O_2 in the serosal channel and 3.0 ± 0.38 mmHg O_2 in the mucosal channel, lowered by the addition of 0.5 M sodium sulfite (Sigma Aldrich, St. Louis, MO).

^{1}H-NMR analysis of tissue media fractions.

Samples were thawed at room temperature and then diluted with D_2O (Cambridge Isotope Laboratories, Andover, MA, USA) by adding 100 μL of D_2O to 900 μL of sample. These were then kept on ice to reduce degradation of SCFAs prior to analysis. Instruments used were the Bruker NEO400 with Prodigy ™ Broad Band Fluorine Observation (BBFO) Probe and Bruker US400 with BBFO SMART Probe ™ (Bruker Scientific LLC, Billerica, MA, USA) located in the Analytical Resources Core, Center for Materials and Molecular Analysis at Colorado State University (Fort Collins, CO, USA). The Bruker NEO400 was operating at 400.07 MHz and the Bruker Ascend 400 MHz was operating at 400.13 MHz.

At 298.0 K probe temperature, the Carr-Purcell-Meiboom-Gill method[39] with presaturation was applied (cpmgpr1d, Bruker pulse program). The parameters of the pulse sequence were 1.0 sec relaxation delay, 0.2 msec fixed echo delay, 90° pulse for 11.0 μsec followed by 180° pulse for 22.0 μsec, 128 scans, 4 dummy scans, 32K points, 15.6 ppm spectral sweep width, with acquisition time of 2.54 sec. There were L4 = 100 echos and presaturation power was 7.2×10^{-5} W (B1 field amplitude was not changed from the autoinput from the cpmgpr1d pulse program). For qualitative identification of SCFA signals, samples of effluent from the device were spiked with 0.5 M of lactic acid (85%+ ACS Reagent, Sigma Aldrich, Saint Louis, MO, USA), acetic acid (glacial, Avantor Performance Materials, Radnor, PA, USA), butyric acid (99%+, Fisher Scientific, Pittsburgh, PA, USA), and propionic acid (99%+, Fisher Scientific, Pittsburgh, PA, USA) to yield a final concentration of 0.167 M of each acid per sample. These samples were then diluted in D_2O so that each SCFA was at 0.150 M just prior to analysis.

Data analysis.

MetaboAnalyst,[40] Mestrenova, and MATLAB were used for data processing and analysis. First, raw spectra were processed by Bruker Topspin using exponential window multiplication of the FID with Lorentzian broadening factor of 0.30 Hz.. Mestrenova was then used to perform a full auto polynomial (n=3) fit for baseline correction. Apodization was 0.30 Hz, exponential with the first point set to 0.5. Linear prediction was done backwards to 3 via Toeplitz algorithm and the group delay was set to linear phase shift. Spectra were binned at 0.02 ppm intervals. Interquartile range data filtering was applied to reduce the number of features for the MetaboAnalyst tool. Normalization of data was performed via log transformation and Pareto scaling.

C.4 Results and Discussion

Identification of chemical shifts of SCFAs in media

We first sought to determine if SCFAs could be resolved from components of the cell culture media. The acidic protons of the carboxylic functional group were omitted from analysis because they would be largely in the deprotonated state at physiological pH in murine colon, thus not present in the ^{1}H-NMR spectra. The chemical shifts and full sample spectrum are available in Appendix D (**Figure D.1** and **Table D.1**). Each spiked sample was spiked with the acid form of each SCFA, which is expected to have an impact on the observed chemical shift for SCFAs in sample solution. Slight variations in pH should be minimal due to buffer present in the effluent samples, however it could alter the chemical environment each proton is experiencing, in terms of electron densities. SCFAs in real samples are expected to be shielded slightly more, thus lower chemical shift than the acid spiked samples. Such shifts, however, are expected to be minimal in their impact.

Further, comparing the expected chemical shifts to the actual sample shows the real sample contains overlap of natural contaminants in the expected region for SCFAs, demonstrating the complexity of the sample matrix. The primary suspects for the signals in the region from 0 to 4 ppm are components of the media used for maintaining tissue explants including amino acids, biotin, corticosterone, and linoleic acid to name a few.[41, 42] For the work herein, SCFAs were the primary interest, and as such, the identities of interfering compounds were not investigated.

Impact of O_2 on SCFA spectral profile. Anaerobic metabolism of carbohydrates by the gut microbiome is the primary source of SCFAs.[13, 43, 44] Based on the findings from an in vitro study,[12] it is expected that the SCFA output will vary based on the differential

populations of bacteria, particularly anaerobic species, without an O_2 gradient applied across the tissue (both mucosal and serosal sides at atmospheric O_2). For example, the main producers of butyrate, the Firmicutes phylum, are expected to thrive in anaerobic conditions over aerobic, resulting in differential butyrate production.[45] The oxygen levels in the MOD-housed tissue were controlled in such a way that the luminal (mucosal) side of the gut tissue approached anaerobic while the serosal side of the tissue was kept at ambient O_2 levels resulting in a physiologically relevant O_2 gradient across the tissue. **Figure C.1** shows representative mucosal tissue effluent spectral differences in the region of interest, 0.50 to 2.50 ppm, as identified from the spiked neurobasal media. Within this range, the SCFA signals are quite different based on the oxygen conditions applied to the tissue, pointing towards an influence of oxygen culture condition on SCFA levels. Based on the signals from butyrate and acetate, there are more of these compounds being produced by the gut microbiome of the tissue maintained under an O_2 gradient. The reverse trend is seen for propionate and lactate. The difference is indicative of different bacteria thriving under the different condition.[46]

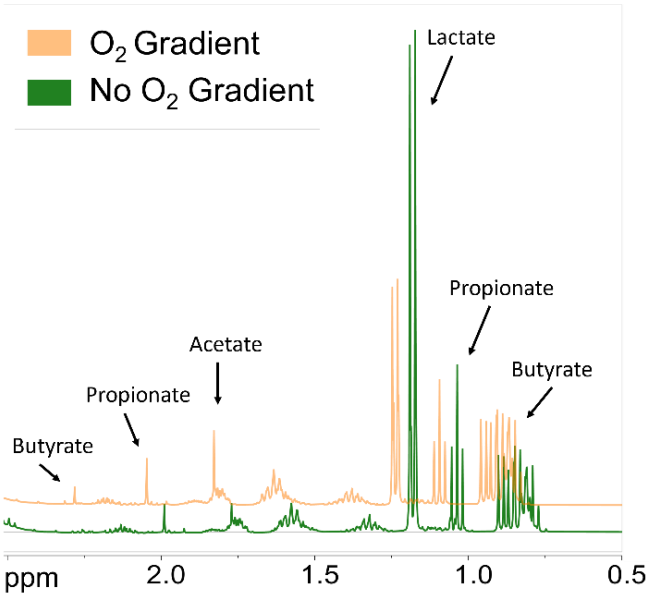

Figure C.1. ^{1}H-NMR (400 MHz, D2O + H2O) spectra show changes in relative abundance of SCFAs present in mucosal tissue effluent with different oxygen conditions. Spectra are offset by 0.05 ppm for clarity. Butyrate is particularly overlapped with signals from components present in neurobasal medium with B-27 supplement.

The importance of oxygen in gut-on-a-chip models is further elucidated by cluster analysis based on the full ^{1}H-NMR spectrum from each sample. Principle components 1 and 2 yielded from principle component analysis (PCA) make up a total of 32.8% of the explained variance in the full spectra for both sides of the tissue under either no gradient O_2 conditions or gradient O_2 (**Figure C.2**). Consideration of the 95% confidence region further demonstrates the clear differences in the full ^{1}H-NMR spectra, with some expected overlap. A closer look at the clusters shows it is clear that the MOD successfully maintained the gut tissue barrier, preventing mixing of serosal and mucosal effluents based on the clear variance between the tissue sides regardless of O_2 condition. This is not surprising based on our observations during sample collection, but it is a good verification that we do not have leakage across the barrier. Second, the O2 gradient has a significant impact on the mucosal effluent composition, as expected, with a slight impact on the

serosal side of the tissue. The serosal sides of both oxygen conditions are assumed to be exposed to the same, ambient, oxygen concentration, additionally, the serosal side is expected to lack the large microbiome present on the mucosal side. The significant variation in mucosal tissue effluent sample spectra supports the importance of considering physiologically accurate oxygen conditions in gut-on-a-chip models. PCA is an unsupervised method and can be less informative than a supervised method such as partial least squares discriminant analysis (PLS-DA) when intragroup variability is high.[47, 48] PLS-DA of the same sample spectra in **Figure C.2** is seen to demonstrate even stronger classification of samples based on the tissue side and oxygen conditions (Appendix D, **Figure D.2**). Due to the concern of overfitting when using PLS-DA, k-fold cross validation was done (Appendix D, **Figure D.3**) where the samples were split into k training and test sets to verify the accuracy of the analysis.[48-50] Here, k-fold (k = 10) cross validation shows $Q^2 > 0.29$ and $R^2 > 0.65$ where R^2 is the correlation coefficient and Q^2 is the correlation coefficient when the PLS-DA model is applied to the test set. These values support the validity of the PLS-DA results by supporting the ability of the model to predict the correct class for a sample with low impact of overfitting.[48, 51]

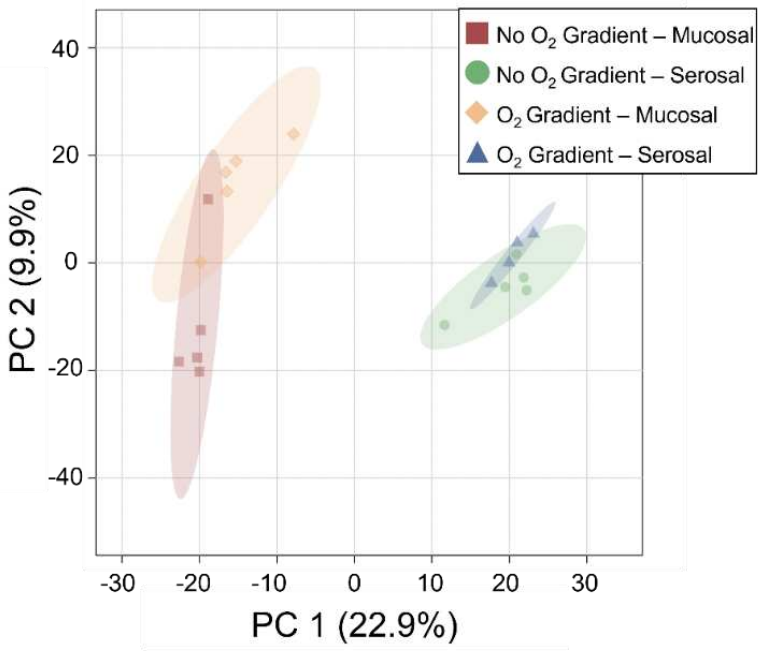

Figure C.2. Principle component analysis (PCA) for the full ^{1}H-NMR spectra (n=5 for all except O_2 gradient – serosal, where n = 4) from mouse colon explant media effluents demonstrates clear separation between the serosal and mucosal effluents as expected. There is less overlap, thus larger variance, between no O_2 gradient and O_2 gradient when considering the mucosal samples.

When considering just the region of interest of 0.50 – 2.50 ppm the clear classification is not seen as easily by discriminant analysis, however unique groups are visible in **Figure C.3**. The heat map shows the 20 most significant features within the region of interest as determined by ANOVA for the average of each group. The average values for mucosal samples for the O_2 gradient are largely opposite of the average spectral profile for the samples from the mucosal side under no O_2 gradient. Features that are high for the O_2 gradient spectra are low for the sample spectra under no O_2 gradient and vice versa. This is suspected to be correlated to different bacteria, thus different SCFA producers, surviving differentially under each condition.[52] This behavior is first noted in **Figure C.1**. Characterization of the bacterial species present would be needed to verify this.

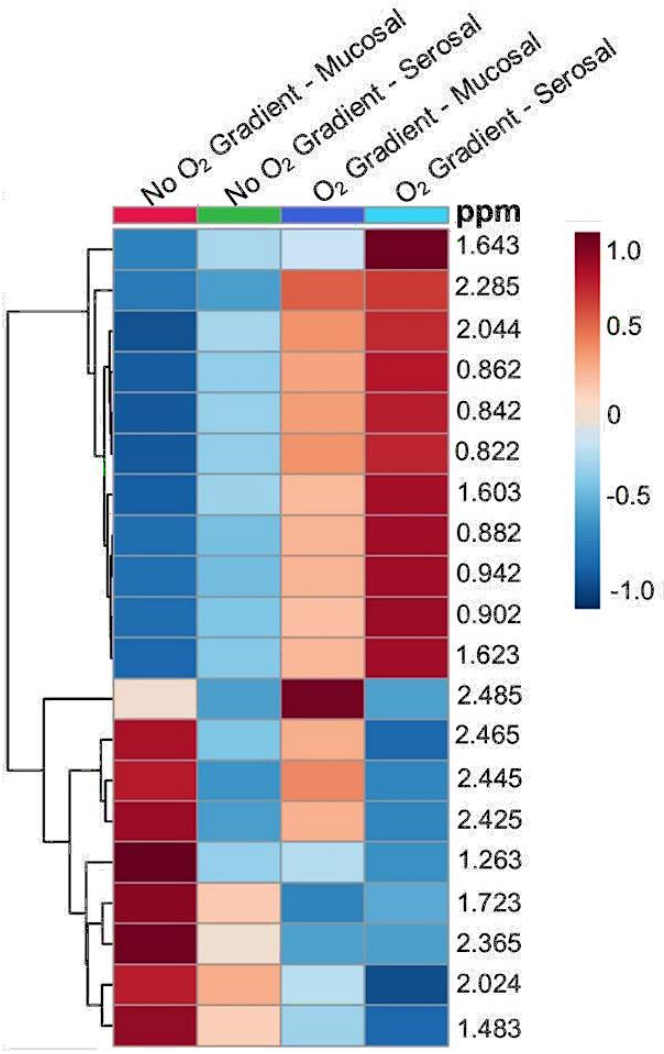

Figure C.3. Heat map using Euclidian distance and Ward clustering algorithm showing clear spectral differences among the 20 most significant features (by ANOVA) in the spectral region of interest of the average of each sample group, n = 5.

Effluent fractions from the MOD. Fractions collected manually at ten-hour increments showed the fluctuation in SCFA levels over time. **Figure C.4** shows representative variation in peak area for two peaks over time. The signal at δ 2.05 corresponds to the singlet for acetate, the signal at δ 1.09 corresponds to the triplet for propionate, and the signal at δ 0.81 is a butyrate triplet (Appendix D, **Table D.1**). For the propionate signal, the peak area trends downward for the first 20 hours and then appears

relatively constant. Acetate increases slightly with no drastic changes and butyrate drops sharply at around 20 hours and then fluctuates. It should be noted that the scale for propionate is at 107 units while acetate and butyrate are at 106. The changes in the relative amounts of each SCFA present are hypothesized to represent a decrease in bacterial metabolism for the first 20 hours that the tissue is in the MOD before a steady state is reached. Since peak area is directly proportional to the absolute concentration of each compound we can use the change in peak area (normalized to an external standard) as a measure of the change in concentration over time.[35] Future iterations of this work will seek to quantify these compounds for further elucidation of the gut tissue in the MOD.

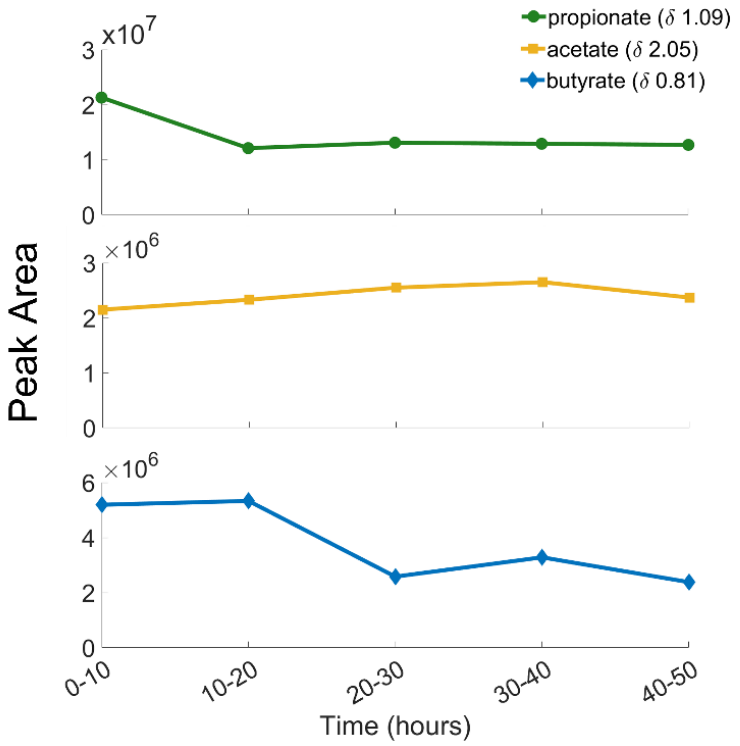

Figure C.4. Trends in SCFA levels over time in mucosal effluent from tissue under physiologically accurate O_2 gradient. Peak areas represent the propionate, acetate, and butyrate signals at δ 1.09, δ 2.05, and δ 0.81, respectively.

Sex-based variation in SCFA profiles. The tissue effluents collected from the MOD were from a population of both male (n = 3) and female (n = 3) mice. When comparing

the SCFA profile of the mucosal effluent of the two sexes, it is seen that there is a distinction between the two (average spectra shown in Appendix D, **Figure D.4**). The heat map shown in **Figure C.5** is a breakdown of those differences within the SCFA region of the ^{1}H-NMR spectra (0.5 to 2.5 ppm). Notable here is the nearly inverse nature between male and female samples, signals that are high in female murine effluent are low in male murine effluent and vice versa. Thus, the SCFA profiles of male and female mice are unique from each other, however a larger sample size is needed to further support this. It has been shown previously that sex-based differences in metabolism and microbiome are present in rats fed supplemented diets.[53] It was also verified that male and female mice exhibit sex-based differences in the gut microbiome linked to the influence of sex hormones.[54, 55] The same has been noted in humans.[56] Overall, the presence of such trend within the results here supports the use of the MOD system with 1H-NMR for the determination of SCFA profiles. It should be noted that these results represent a preliminary result that would need to be verified with a larger population to draw an accurate biological conclusion.

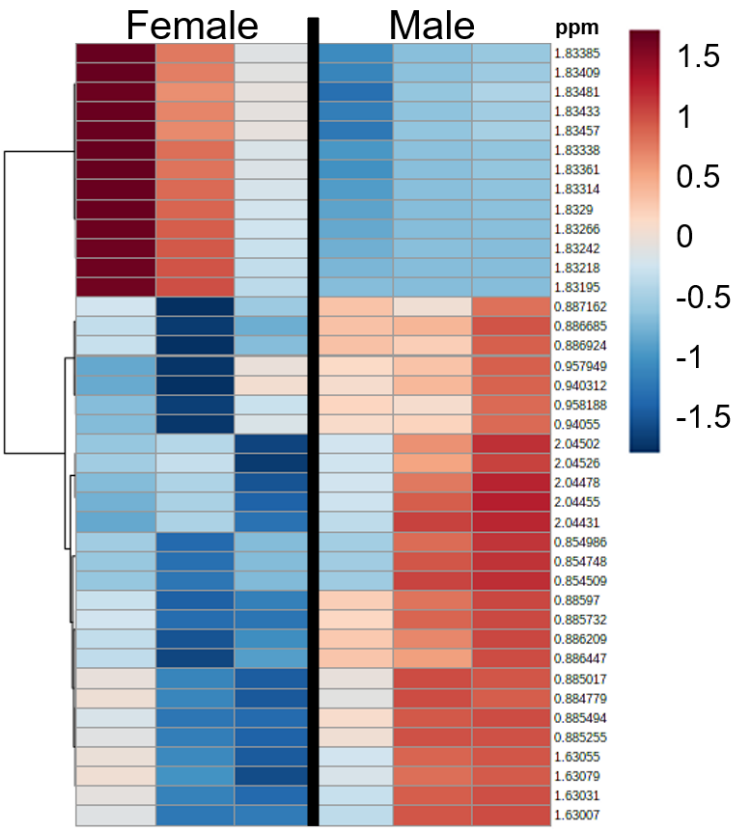

Figure C.5. Heat map showing clear differences between male (n = 3) and female (n = 3) mucosal samples spectral region of interest (0.5 to 2.5 ppm).

C.5 Conclusions

Here is reported the proof of concept for the use of the MOD tissue on a chip culture system with 1H-NMR for the analysis of SCFA profiles from gut tissue culture effluents. Spectra showed the importance of considering the presence of a physiologically relevant O2 gradient across the gut tissue. The device also allowed for the collection of samples over time which is limited in the most common SCFA analysis techniques that use fecal samples. The data also reiterated the sex-based differences in microbiome by showing the disparities in SCFA production. Information gained supports the development of a baseline for male and female mouse gut effluent so that the impact of drug dosage or tissue environment in the MOD can be monitored.

References

1. Martinez, B.; Schwerdtfeger, L. A.; Richardson, A.; Tobet, S. A.; Henry, C. S., 1H-NMR Profiling of Short-Chain Fatty Acid Content from a Physiologically Accurate Gut-on-a-Chip Device. *Analytical Chemistry* **2022,** *94* (28), 9987-9992.

2. Skonieczna-Żydecka, K.; Grochans, E.; Maciejewska, D.; Szkup, M.; Schneider-Matyka, D.; Jurczak, A.; Łoniewski, I.; Kaczmarczyk, M.; Marlicz, W.; Czerwińska-Rogowska, M.; Pełka-Wysiecka, J.; Dec, K.; Stachowska, E., Faecal Short Chain Fatty Acids Profile is Changed in Polish Depressive Women. *Nutrients* **2018,** *10* (12).

3. den Besten, G.; van Eunen, K.; Groen, A. K.; Venema, K.; Reijngoud, D.-J.; Bakker, B. M., The role of short-chain fatty acids in the interplay between diet, gut microbiota, and host energy metabolism. *Journal of Lipid Research* **2013,** *54* (9), 2325-2340.

4. Sanna, S.; van Zuydam, N. R.; Mahajan, A.; Kurilshikov, A.; Vich Vila, A.; Võsa, U.; Mujagic, Z.; Masclee, A. A. M.; Jonkers, D. M. A. E.; Oosting, M.; Joosten, L. A. B.; Netea, M. G.; Franke, L.; Zhernakova, A.; Fu, J.; Wijmenga, C.; McCarthy, M. I., Causal relationships among the gut microbiome, short-chain fatty acids and metabolic diseases. *Nature Genetics* **2019,** *51* (4), 600-605.

5. Cook; Sellin, Review article: short chain fatty acids in health and disease. *Alimentary Pharmacology & Therapeutics* **1998,** *12* (6), 499-507.

6. Ríos-Covián, D.; Ruas-Madiedo, P.; Margolles, A.; Gueimonde, M.; de los Reyes-Gavilán, C. G.; Salazar, N., Intestinal Short Chain Fatty Acids and their Link with Diet and Human Health. *Frontiers in Microbiology* **2016,** *7*, 185.

7. Dürholz, K.; Hofmann, J.; Iljazovic, A.; Häger, J.; Lucas, S.; Sarter, K.; Strowig, T.; Bang, H.; Rech, J.; Schett, G.; Zaiss, M. M., Dietary Short-Term Fiber Interventions

in Arthritis Patients Increase Systemic SCFA Levels and Regulate Inflammation. *Nutrients* **2020,** *12* (10), 3207-3207.

8. Tan, J.; McKenzie, C.; Potamitis, M.; Thorburn, A. N.; Mackay, C. R.; Macia, L., Chapter Three - The Role of Short-Chain Fatty Acids in Health and Disease. Alt, F. W. B. T. A. i. I., Ed. Academic Press: 2014; Vol. 121, pp 91-119.

9. Kathleen, M.; Marie, J.; João, S.; Vicky De, P.; Ingrid, A.; Venessa, E.; Vera, B.; Karolien, C.; Filip Van, I.; Kristin, V.; Marc, F.; Jan, V.; Paul, R.; Séverine, V., A decrease of the butyrate-producing species Roseburia hominis and Faecalibacterium prausnitzii defines dysbiosis in patients with ulcerative colitis. *Gut* **2014,** *63* (8), 1275.

10. Cox, L. M.; Abou-El-Hassan, H.; Maghzi, A. H.; Vincentini, J.; Weiner, H. L., The sex-specific interaction of the microbiome in neurodegenerative diseases. *Brain Res* **2019,** *1724*, 146385.

11. Jangi, S.; Gandhi, R.; Cox, L. M.; Li, N.; von Glehn, F.; Yan, R.; Patel, B.; Mazzola, M. A.; Liu, S.; Glanz, B. L.; Cook, S.; Tankou, S.; Stuart, F.; Melo, K.; Nejad, P.; Smith, K.; Topçuolu, B. D.; Holden, J.; Kivisäkk, P.; Chitnis, T.; De Jager, P. L.; Quintana, F. J.; Gerber, G. K.; Bry, L.; Weiner, H. L., Alterations of the human gut microbiome in multiple sclerosis. *Nat Commun* **2016,** *7*, 12015.

12. Shah, P.; Fritz, J. V.; Glaab, E.; Desai, M. S.; Greenhalgh, K.; Frachet, A.; Niegowska, M.; Estes, M.; Jäger, C.; Seguin-Devaux, C.; Zenhausern, F.; Wilmes, P., A microfluidics-based in vitro model of the gastrointestinal human-microbe interface. *Nat Commun* **2016,** *7*, 11535-11535.

13. Greenhalgh, K.; Ramiro-Garcia, J.; Heinken, A.; Ullmann, P.; Bintener, T.; Pacheco, M. P.; Baginska, J.; Shah, P.; Frachet, A.; Halder, R.; Fritz, J. V.; Sauter, T.;

Thiele, I.; Haan, S.; Letellier, E.; Wilmes, P., Integrated In Vitro and In Silico Modeling Delineates the Molecular Effects of a Synbiotic Regimen on Colorectal-Cancer-Derived Cells. *Cell Reports* **2019,** *27* (5), 1621-1632.e9.

14. McLean, I. C.; Schwerdtfeger, L. A.; Tobet, S. A.; Henry, C. S., Powering ex vivo tissue models in microfluidic systems. *Lab Chip* **2018,** *18* (10), 1399-1410.

15. Ashammakhi, N.; Nasiri, R.; Barros, N. R. d.; Tebon, P.; Thakor, J.; Goudie, M.; Shamloo, A.; Martin, M. G.; Khademhosseini, A., Gut-on-a-chip: Current progress and future opportunities. *Biomaterials* **2020,** *255*, 120196.

16. Moysidou, C.-M.; Owens, R. M., Advances in modelling the human microbiome-gut-brain axis in vitro. *Biochem Soc Trans* **2021,** *49* (1), 187-201.

17. Kim, H. J.; Huh, D.; Hamilton, G.; Ingber, D. E., Human gut-on-a-chip inhabited by microbial flora that experiences intestinal peristalsis-like motions and flow. *Lab on a Chip* **2012,** *12* (12), 2165-2174.

18. Kim, H. J.; Ingber, D. E., Gut-on-a-Chip microenvironment induces human intestinal cells to undergo villus differentiation. *Integrative Biology* **2013,** *5* (9), 1130-1140.

19. Lee, S. Y.; Sung, J. H., Gut–liver on a chip toward an in vitro model of hepatic steatosis. *Biotechnology and Bioengineering* **2018,** *115* (11), 2817-2827.

20. Jalili-Firoozinezhad, S.; Gazzaniga, F. S.; Calamari, E. L.; Camacho, D. M.; Fadel, C. W.; Bein, A.; Swenor, B.; Nestor, B.; Cronce, M. J.; Tovaglieri, A.; Levy, O.; Gregory, K. E.; Breault, D. T.; Cabral, J. M. S.; Kasper, D. L.; Novak, R.; Ingber, D. E., A complex human gut microbiome cultured in an anaerobic intestine-on-a-chip. *Nature Biomedical Engineering* **2019,** *3* (7), 520-531.

21. Kim, H. J.; Li, H.; Collins, J. J.; Ingber, D. E., Contributions of microbiome and mechanical deformation to intestinal bacterial overgrowth and inflammation in a human gut-on-a-chip. *Proceedings of the National Academy of Sciences* **2016,** *113* (1), E7.

22. Yissachar, N.; Zhou, Y.; Ung, L.; Lai, N. Y.; Mohan, J. F.; Ehrlicher, A.; Weitz, D. A.; Kasper, D. L.; Chiu, I. M.; Mathis, D.; Benoist, C., An Intestinal Organ Culture System Uncovers a Role for the Nervous System in Microbe-Immune Crosstalk. *Cell* **2017,** *168* (6), 1135-1148.e12.

23. Richardson, A.; Schwerdtfeger, L. A.; Eaton, D.; McLean, I.; Henry, C. S.; Tobet, S. A., A microfluidic organotypic device for culture of mammalian intestines ex vivo. *Analytical Methods* **2020,** *12* (3), 297-303.

24. van Eijk, H. M. H.; Bloemen, J. G.; Dejong, C. H. C., Application of liquid chromatography–mass spectrometry to measure short chain fatty acids in blood. *Journal of Chromatography B* **2009,** *877* (8), 719-724.

25. Primec, M.; Mičetić-Turk, D.; Langerholc, T., Analysis of short-chain fatty acids in human feces: A scoping review. *Analytical Biochemistry* **2017,** *526*, 9-21.

26. Schwerdtfeger, L. A.; Nealon, N. J.; Ryan, E. P.; Tobet, S. A., Human colon function ex vivo: Dependence on oxygen and sensitivity to antibiotic. *PloS one* **2019,** *14* (5), e0217170-e0217170.

27. Baxter, B. A.; Parker, K. D.; Nosler, M. J.; Rao, S.; Craig, R.; Seiler, C.; Ryan, E. P., Metabolite profile comparisons between ascending and descending colon tissue in healthy adults. *World J Gastroenterol* **2020,** *26* (3), 335-352.

28. Bertram, H. C.; Kristensen, N. B.; Malmendal, A.; Nielsen, N. C.; Bro, R.; Andersen, H. J.; Harmon, D. L., A metabolomic investigation of splanchnic metabolism

using 1H NMR spectroscopy of bovine blood plasma. *Analytica Chimica Acta* **2005,** *536* (1), 1-6.

29. Cui, M.; Trimigno, A.; Aru, V.; Khakimov, B.; Engelsen, S. B., Human Faecal 1H NMR Metabolomics: Evaluation of Solvent and Sample Processing on Coverage and Reproducibility of Signature Metabolites. *Analytical Chemistry* **2020,** *92* (14), 9546-9555.

30. Cai, J.; Zhang, J.; Tian, Y.; Zhang, L.; Hatzakis, E.; Krausz, K. W.; Smith, P. B.; Gonzalez, F. J.; Patterson, A. D., Orthogonal Comparison of GC–MS and 1H NMR Spectroscopy for Short Chain Fatty Acid Quantitation. *Analytical Chemistry* **2017,** *89* (15), 7900-7906.

31. Zeng, M.; Cao, H., Fast quantification of short chain fatty acids and ketone bodies by liquid chromatography-tandem mass spectrometry after facile derivatization coupled with liquid-liquid extraction. *Journal of Chromatography B* **2018,** *1083*, 137-145.

32. Song, W.-S.; Park, H.-G.; Kim, S.-M.; Jo, S.-H.; Kim, B.-G.; Theberge, A. B.; Kim, Y.-G., Chemical derivatization-based LC–MS/MS method for quantitation of gut microbial short-chain fatty acids. *Journal of Industrial and Engineering Chemistry* **2020,** *83*, 297-302.

33. Haddad, L.; Francis, J.; Rizk, T.; Akoka, S.; Remaud, G. S.; Bejjani, J., Cheese characterization and authentication through lipid biomarkers obtained by high-resolution 1H NMR profiling. *Food Chemistry* **2022,** *383*, 132434.

34. Nicholson, J. K.; Wilson, I. D., High resolution proton magnetic resonance spectroscopy of biological fluids. *Progress in Nuclear Magnetic Resonance Spectroscopy* **1989,** *21* (4), 449-501.

35. Vonhof, E. V.; Piotto, M.; Holmes, E.; Lindon, J. C.; Nicholson, J. K.; Li, J. V., Improved Spatial Resolution of Metabolites in Tissue Biopsies Using High-Resolution Magic-Angle-Spinning Slice Localization NMR Spectroscopy. *Analytical Chemistry* **2020,** *92* (17), 11516-11519.

36. Saric, J.; Wang, Y.; Li, J.; Coen, M.; Utzinger, J.; Marchesi, J. R.; Keiser, J.; Veselkov, K.; Lindon, J. C.; Nicholson, J. K.; Holmes, E., Species Variation in the Fecal Metabolome Gives Insight into Differential Gastrointestinal Function. *Journal of Proteome Research* **2008,** *7* (1), 352-360.

37. Ndagijimana, M.; Laghi, L.; Vitali, B.; Placucci, G.; Brigidi, P.; Guerzoni, M. E., Effect of a synbiotic food consumption on human gut metabolic profiles evaluated by 1H Nuclear Magnetic Resonance spectroscopy. *International Journal of Food Microbiology* **2009,** *134* (1), 147-153.

38. Jacobs, D. M.; Deltimple, N.; van Velzen, E.; van Dorsten, F. A.; Bingham, M.; Vaughan, E. E.; van Duynhoven, J., 1H NMR metabolite profiling of feces as a tool to assess the impact of nutrition on the human microbiome. *NMR in Biomedicine* **2008,** *21* (6), 615-626.

39. Dona, A. C., Standardized NMR Protocols for Metabonomics. In *Encyclopedia of Spectroscopy and Spectrometry (Third Edition)*, Lindon, J. C.; Tranter, G. E.; Koppenaal, D. W., Eds. Academic Press: Oxford, 2017; pp 218-223.

40. Chong, J.; Wishart, D. S.; Xia, J., Using MetaboAnalyst 4.0 for Comprehensive and Integrative Metabolomics Data Analysis. *Current Protocols in Bioinformatics* **2019,** *68* (1), e86-e86.

41. Scientific, T. B-27 Serum-Free Supplement (50X) liquid. https://www.thermofisher.com/us/en/home/technical-resources/media-formulation.250.html.

42. Brewer, G. J.; Torricelli, J. R.; Evege, E. K.; Price, P. J., Optimized survival of hippocampal neurons in B27-supplemented Neurobasal, a new serum-free medium combination. *J Neurosci Res* **1993,** *35* (5), 567-76.

43. Clarke, G.; Stilling, R. M.; Kennedy, P. J.; Stanton, C.; Cryan, J. F.; Dinan, T. G., Minireview: Gut Microbiota: The Neglected Endocrine Organ. *Molecular Endocrinology* **2014,** *28* (8), 1221-1238.

44. Cummings, J. H., Short chain fatty acids in the human colon. *Gut* **1981,** *22* (9), 763-779.

45. Macfarlane, S.; Macfarlane, G. T., Regulation of short-chain fatty acid production. *Proceedings of the Nutrition Society* **2003,** *62* (1), 67-72.

46. Parada Venegas, D.; De la Fuente, M. K.; Landskron, G.; González, M. J.; Quera, R.; Dijkstra, G.; Harmsen, H. J. M.; Faber, K. N.; Hermoso, M. A., Short Chain Fatty Acids (SCFAs)-Mediated Gut Epithelial and Immune Regulation and Its Relevance for Inflammatory Bowel Diseases. *Frontiers in Immunology* **2019,** *10*, 277.

47. Fonville, J. M.; Richards, S. E.; Barton, R. H.; Boulange, C. L.; Ebbels, T. M. D.; Nicholson, J. K.; Holmes, E.; Dumas, M.-E., The evolution of partial least squares models and related chemometric approaches in metabonomics and metabolic phenotyping. *Journal of Chemometrics* **2010,** *24* (11-12), 636-649.

48. Worley, B.; Powers, R., Multivariate Analysis in Metabolomics. *Current Metabolomics* **2013,** *1* (1), 92-107.

49. Rodríguez-Pérez, R.; Fernández, L.; Marco, S., Overoptimism in cross-validation when using partial least squares-discriminant analysis for omics data: a systematic study. *Analytical and Bioanalytical Chemistry* **2018,** *410* (23), 5981-5992.

50. Saccenti, E.; Timmerman, M. E., Approaches to Sample Size Determination for Multivariate Data: Applications to PCA and PLS-DA of Omics Data. *Journal of Proteome Research* **2016,** *15* (8), 2379-2393.

51. Henseler, J.; Ringle, C. M.; Sinkovics, R. R., The use of partial least squares path modeling in international marketing. In *New Challenges to International Marketing*, Sinkovics, R. R.; Ghauri, P. N., Eds. Emerald Group Publishing Limited: 2009; Vol. 20, pp 277-319.

52. Zeng, H.; Umar, S.; Rust, B.; Lazarova, D.; Bordonaro, M., Secondary Bile Acids and Short Chain Fatty Acids in the Colon: A Focus on Colonic Microbiome, Cell Proliferation, Inflammation, and Cancer. *Int J Mol Sci* **2019,** *20* (5), 1214.

53. Shastri, P.; McCarville, J.; Kalmokoff, M.; Brooks, S. P. J.; Green-Johnson, J. M., Sex differences in gut fermentation and immune parameters in rats fed an oligofructose-supplemented diet. *Biology of Sex Differences* **2015,** *6* (1), 13-13.

54. Markle, J. G. M.; Frank, D. N.; Mortin-Toth, S.; Robertson, C. E.; Feazel, L. M.; Rolle-Kampczyk, U.; von Bergen, M.; McCoy, K. D.; Macpherson, A. J.; Danska, J. S., Sex Differences in the Gut Microbiome Drive Hormone-Dependent Regulation of Autoimmunity. *Science* **2013,** *339* (6123), 1084 LP-1088.

55. Org, E.; Mehrabian, M.; Parks, B. W.; Shipkova, P.; Liu, X.; Drake, T. A.; Lusis, A. J., Sex differences and hormonal effects on gut microbiota composition in mice. *Gut Microbes* **2016,** *7* (4), 313-322.

56. Mueller, S.; Saunier, K.; Hanisch, C.; Norin, E.; Alm, L.; Midtvedt, T.; Cresci, A.; Silvi, S.; Orpianesi, C.; Verdenelli, M. C.; Clavel, T.; Koebnick, C.; Zunft, H.-J. F.; Doré, J.; Blaut, M., Differences in Fecal Microbiota in Different European Study Populations in Relation to Age, Gender, and Country: a Cross-Sectional Study. *Applied and Environmental Microbiology* **2006,** *72* (2), 1027 LP-1033.

APPENDIX D – Supporting Information for Appendix C: ^{1}H-NMR Profiling of Short-Chain Fatty Acid Content from a Physiologically Accurate Gut-on-a-Chip Device

Table of Contents

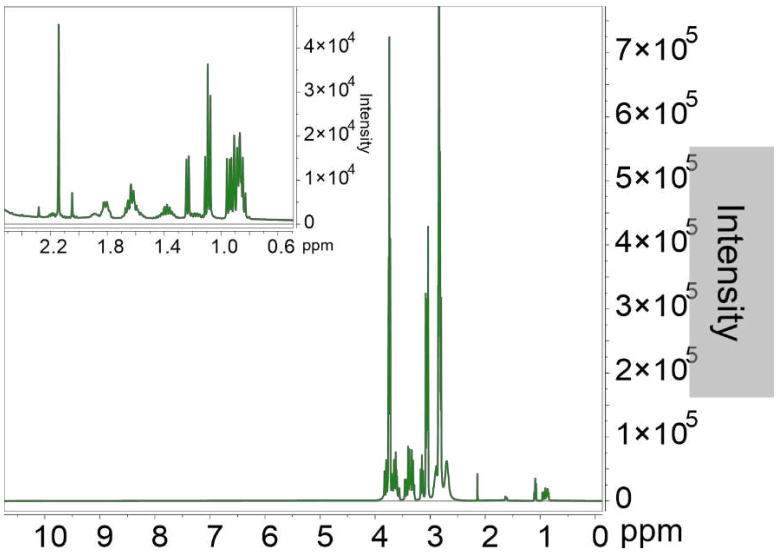

Figure D.1. Representative full ^{1}H-NMR (400 MHz, D_2O + H_2O) spectra for murine tissue effluent using CPMG pulse sequence with presaturation. Inset is the region of interest, 0.5 to 2.5 ppm.

Table D.1. ^{1}H-NMR signals for short-chain fatty acids in CTS Neurobasal-A Medium with B27 supplement and HEPES buffer.

Short-chain fatty acid	Signal (ppm)
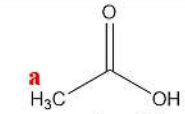 Acetic acid	a: δ1.96, singlet
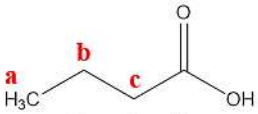 Butyric acid	a: δ0.81, triplet
	b: δ1.49, sextet
	c: δ2.22, triplet
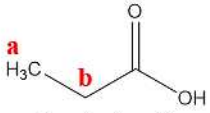 Propionic acid	a: δ0.96, triplet
	b: δ2.08, quartet
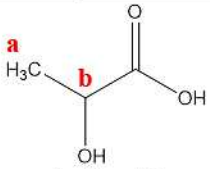 Lactic acid	a: δ1.30, doublet
	b: δ4.25, quartet

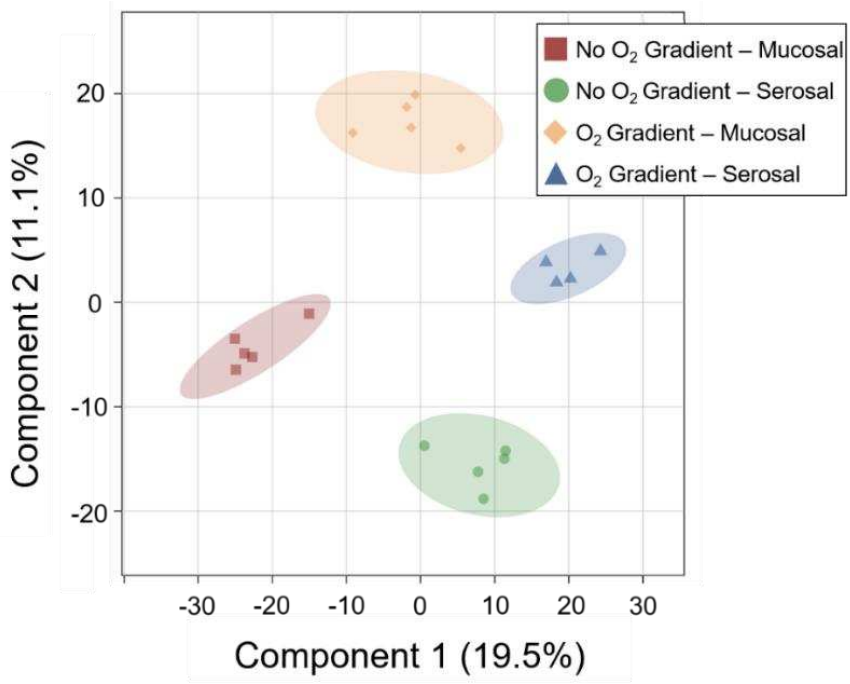

Figure D.2. Partial least squares discriminant analysis (PLS-DA) demonstrates clear separation of each tissue side as well as the gradient to no gradient O_2 conditions supporting the importance of physiologically accurate O_2 levels to the metabolite profile. (n = 5 for all except O_2 gradient – serosal where n = 4).

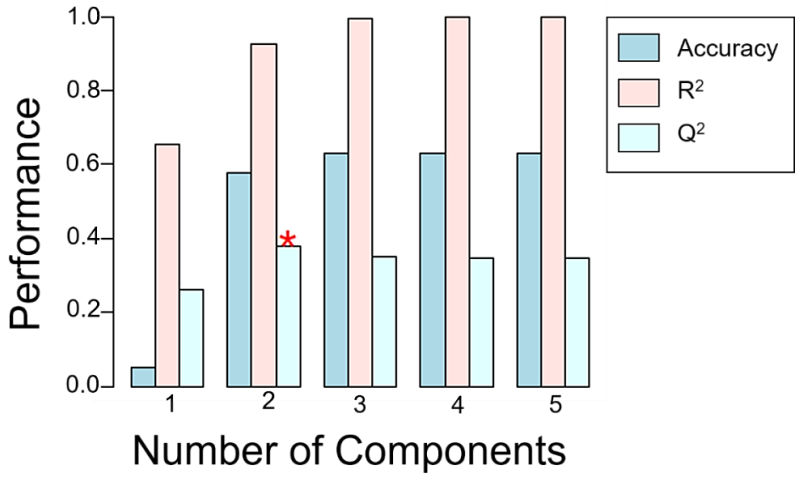

Figure D.3. Resulting 10-fold cross validation for the PLS-DA shown in **Figure D.2** of Appendix D. Star indicates the best classifier for the data.

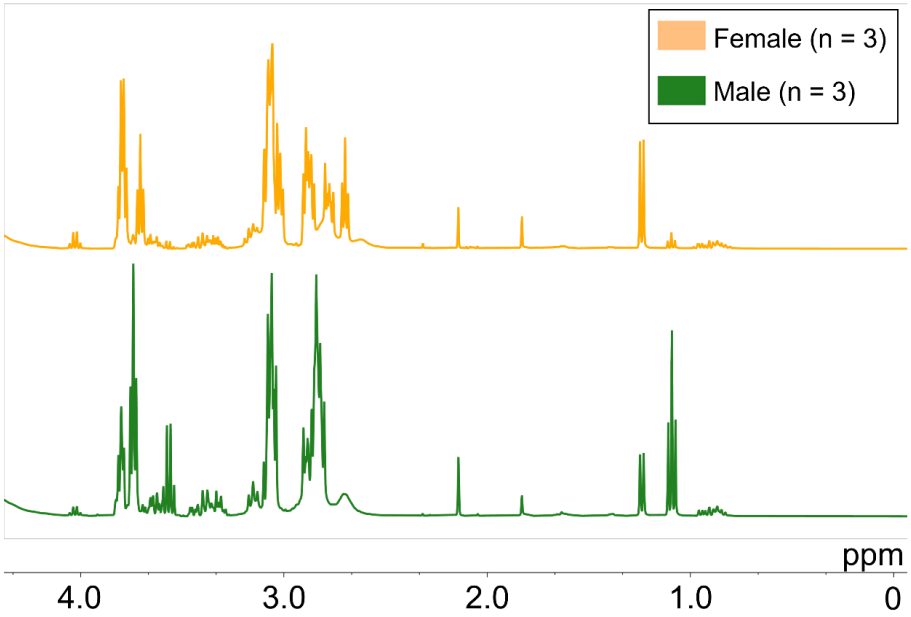

Figure D.4. ^{1}H-NMR (400 MHz, D_2O + H_2O) average (n = 3) spectra for mucosal effluent from male and female mouse colon explants in MOD under physiologically relevant O_2 gradient.